

ANALYZING THE THERMAL ANNEALING BEHAVIOR OF LASER THERMAL
PROCESSED SILICON

By

ERIK ADAM KURYLIW

A DISSERTATION PRESENTED TO THE GRADUATE SCHOOL
OF THE UNIVERSITY OF FLORIDA IN PARTIAL FULFILLMENT
OF THE REQUIREMENTS FOR THE DEGREE OF
DOCTOR OF PHILOSOPHY

UNIVERSITY OF FLORIDA

2003

Copyright 2003

by

Erik Kuryliw

ACKNOWLEDGMENTS

I would like to thank my advisors, Profs. Kevin Jones and Mark Law, for their guidance, support, and patience throughout the many years it took to complete this work. I am also grateful for the wonderful work environment and the quality of students they have brought together to create the SWAMP Center. I would also like to thank Profs. David Norton, Susan Sinnott, and Michael Kaufman for their participation on my supervisory committee.

Sematech and the Semiconductor Research Council (SRC) provided financial support for this research. Without those funds this work and many others within the SWAMP Center could not have been pursued. Additionally, I am personally indebted to the SRC for the Graduate Fellowship Award that allowed me to pay the rent, find two separate internships at Intel Corp., as well as create a network of contacts that will be invaluable to the future of my career. I am especially grateful for the processed silicon wafers that were provided by Michael Rendon and David Sing of Motorola, and to Somit Talwar for allowing access to the laser annealing tools at Verdant Technologies. I would also like to thank Prof. Mike Thompson and Shenzhi Yang of Cornell University for their assistance with initial laser experiments and helpful discussions. Finally, this work would have never progressed past its infancy had it not been for the hard work of fellow graduate student Kevin Gable. His last minute trip out to California saved this project and for that I will be forever grateful. I would also like to thank Kevin and a long list of other graduate students, both past and present, for providing many both useful and

useless discussions. I would especially like to thank Lance Robertson who encouraged me to “just give grad school a shot.”

Of course I never would have gone to college had it not been for the love, support, support and education of my parents, Denny and Monique, as well as my desire to be an excellent role model and older brother to my siblings, Derek and Kevin. They and the rest of my family provided me the perfect environment to grow up in and become the person I am today. I must also acknowledge the many friends and roommates I have had during my many years here in Gainesville, including Mike, Ken, Durden and Rhodes. Finally, I will forever be indebted to my current roommate and best friend, Misty. Without her assistance and encouragement, I might never have seen this work to its completion.

TABLE OF CONTENTS

	<u>Page</u>
ACKNOWLEDGMENTS	iii
LIST OF TABLES	viii
LIST OF FIGURES	ix
ABSTRACT	xiii
CHAPTER	
1 MOTIVATION	1
Brief History of Semiconductors	1
Shallow Junction Scaling Challenges	2
Conventional Processing	3
Laser Thermal Processing	4
Scope and Organization	4
2 BACKGROUND	9
Ion Implantation	9
Point Defects	10
Amorphization	12
Thermal Annealing	13
Diffusion	13
Macroscopic diffusion	13
Point defect mediated diffusion	14
Activation	16
Solubility limited activation	17
Point defect limited activation	18
Microstructure Evolution	18
Amorphous layer regrowth	18
Extended defect evolution	19
Challenges	20
Laser Annealing	23
Melting of Amorphous Silicon	24
Measuring liquid-solid interfaces	24
Altering the solid-liquid interface velocity	25

Non-equilibrium Solute Trapping	27
Laser Thermal Processing	29
Shrinking of the process window	30
Post LTP thermal cycling	30
3 MICROSTRUCTURAL STUDIES.....	45
Characterization.....	45
Transmission Electron Microscopy (TEM).....	45
Variable Angle Spectroscopic Ellipsometry (VASE)	46
Experimental Outline.....	47
As-LTP Defect Density	49
Comparing Conventional and LTP	52
Defect Analysis	52
Evolution of EOR Dislocation Loops.....	53
Evolution of Epitaxial Defects	53
Effect of Laser Power on Loop Evolution.....	54
Summary.....	56
4 DIFFUSION AND ACTIVATION STUDIES.....	72
Characterization.....	72
Secondary Ion Mass Spectrometry (SIMS).....	72
Spreading Resistance Profiling (SRP).....	73
Four Point Probe (4PP).....	74
Hall Effect Measurement.....	74
Experimental Outline.....	74
Diffusion Studies of LTP Silicon	76
Retained Dose Calibration.....	77
Defining the Process Window	78
Diffusion of Boron	79
Diffusion of Antimony	81
Activation Studies of LTP Silicon.....	81
Four Point Probe.....	82
Spreading Resistance Profiling.....	84
Hall Effect Measurement.....	85
Summary.....	87
5 DISCUSSIONS AND CONCLUSIONS.....	107
Initial Theories and Discussion of Results	107
Theories for Reduced Interstitial Population in Loops.....	108
Reduction of available interstitials.....	109
Altered nucleation process	110

Proposed Theory.....	111
Very Low Temperature Annealing.....	112
Loop Evolution.....	113
Boron Diffusion.....	113
Deactivation.....	114
Beyond the Process Window.....	114
Crystal Melt Conditions.....	116
As-implanted.....	116
Annealed.....	117
Summary.....	118
6 SUMMARY AND FUTURE RECOMMENDATIONS.....	132
Synopsis of Results.....	132
Conclusion.....	134
Areas of Further Study.....	134
APPENDIX	
A EFFECT OF PARAMETER VARIATIONS.....	136
B STEREOLOGY OF DEFECTS.....	138
LIST OF REFERENCES.....	140
BIOGRAPHICAL SKETCH.....	146

LIST OF TABLES

<u>Table</u>	<u>page</u>
2-1 Diffusion parameters D_0 and E_A for dopants boron and antimony in silicon.	44
2-2 Equilibrium segregation coefficient, k_0 , and non-equilibrium coefficient, k' , values for dopants.....	44
2-3 Maximum equilibrium solid solubility, C_s^0 , of dopants	44

LIST OF FIGURES

<u>Figure</u>	<u>page</u>
1-1 Diagram of conventional MOSFET	6
1-2 Moore's Law.....	6
1-3 Technology nodes for the ITRS 2000.....	7
1-4 Revised ITRS for 2002.....	8
2-2 Implant profile showing the difference between a channeled implant into crystalline silicon and one implanted into an amorphous layer	33
2-3 Equilibrium concentrations of interstitials and vacancies as a function of inverse temperature.....	34
2-4 Damage cascades created by different ion masses	34
2-5 Representation of how different concentrations of damage can result in a) crystalline, b) buried amorphous, and c) continuous amorphous layers.....	35
2-6 Effect of active doping concentration on the mobility of carriers	35
2-7 Solubility of various dopants in silicon as a function of temperature.	36
2-8 Phase diagram of boron and silicon.....	37
2-9 Diagram showing a typical interstitial profile following the solid phase epitaxy of an ion implantation induced amorphous layer	38
2-10 Gibbs free energy differences for Si crystal.....	39
2-11 Solid phase epitaxy growth rate of undoped amorphous silicon in the <100> direction as a function of inverse temperature	40
2-12 Recrystallization velocity of silicon from both amorphous layers (solid line) and metallic melt (hashed area)	41
2-13 An example of transient conductance and reflectance measurement	42
2-14 Diagram of different undercooling regimes	43

3-1 Cross section image of material implanted with 15keV Si ⁺	57
3-2 Cross section image of material laser annealed at 770 mJ/cm ²	58
3-3 Cross section image of material laser annealed at 825 mJ/cm ²	58
3-4 Plan view image of material laser annealed at a) 730, b) 750, c) 770, d) 800, e) 825, and f) 850 mJ/cm ²	59
3-5 Diffraction pattern of 730 mJ/cm ² material showing a poly-crystalline ring pattern..	60
3-6 Diffraction pattern of 770 mJ/cm ² material observed down the a) {100} and b) {111} zone axis	60
3-7 Diffraction pattern of 825 mJ/cm ² material observed down the {100} zone axis.....	61
3-8 Epitaxial defect density as a function the laser energy density	61
3-9 Images comparing defect evolution in plan view and in cross section	62
3-10 Series of plan view images showing the evolution of defects in material laser annealed at 770 mJ/cm ² and then subsequently thermally annealed at 750 °C.....	63
3-11 Series of plan view images showing the evolution of defects in material laser annealed at 770 mJ/cm ² and then subsequently thermally annealed at 750 °C.....	64
3-12 The evolution of the regrowth related defect density as a function of laser energy density at 750 °C	65
3-13 Series of plan view images showing the evolution of defects in material laser annealed at 770 mJ/cm ² and then subsequently thermally annealed at 900 °C.....	66
3-14 Images comparing the annealing behavior for samples.....	67
3-15 Images showing material laser annealed at 750 mJ/cm ² and then subsequently thermally annealed at 750 °C for a) 4 and b) 8 hours.....	68
3-16 Trapped interstitials in dislocation loops as a function of laser energy density at an anneal temperature of 750 °C	69
3-17 Plots showing both the a) average loop size and b) number density of loops as a function of time for each material	70
3-18 Plot showing the trapped interstitial density in dislocation loops as a function of the epitaxial defect density	71
4-1 SIMS of boron doped laser processed material. Laser energy densities from 730 up to 900 mJ/cm ² are shown	89

4-2 SIMS of boron comparing diffusion in conventionally processed material and that having first received a laser anneal at an energy density of 800 mJ/cm ²	90
4-3 SIMS of boron doped laser processed material having received a 750 °C 2 h.....	91
4-4 SIMS of boron doped laser processed material subsequently thermally annealed at 900 °C for 100m	92
4-5 PTEM of material laser annealed at 770 mJ/cm ² and then thermally annealed at 750 °C for 2h and 900 °C for 100m.....	92
4-6 SIMS of boron doped laser processed material (770 mJ/cm ²) subsequently thermally annealed at 900 °C for 5 m	93
4-7 PTEM of material laser annealed at 770 mJ/cm ² and then thermally annealed at 750 °C for 2h and 900 °C for 5 m.....	93
4-8 SIMS boron profile showing the difference in time to saturation for enhanced diffusion for material laser annealed at 770 compared to 800 mJ/cm ²	94
4-9 SIMS of antimony doped laser processed material (770 and 800 mJ/cm ²).....	95
4-10 Sheet resistance for boron doped laser processed material as a function of the laser energy density	96
4-11 Sheet resistance for antimony doped laser processed material as a function of the laser energy density.....	97
4-12 Sheet resistance for boron doped laser processed material as a function of the laser energy density. The material was then subjected to a 750 °C anneal for times between 20 s and 4 hours	98
4-13 Sheet resistance of boron doped LTP material as a function of time at 750 °C for process window material laser annealed at 750, 770, and 800 mJ/cm ²	99
4-14 Sheet resistance for antimony doped laser processed material as a function of the laser energy density. The material was then subjected to a 750 °C anneal for times between 20 s and 2 hours	100
4-15 SRP of 800 mJ/cm ² with no anneal and 750 2h	101
4-16 Hall effect of as-LTP material at room temperature.....	102
4-17 Hall effect measurement of active boron dose as a function of laser energy density, at temperatures below 250 K.....	103
4-18 Hall effect measurement of active boron dose as a function of laser energy density used during laser annealing	104

4-19 Hall effect measurement of active antimony dose as a function of energy density used during laser annealing	105
4-20 Hall active boron dose measurement as a function of energy density used during laser annealing.....	106
5-1 Boron junction depth and trapped interstitial concentration as a function of anneal time at 750 °C.....	120
5-2 XTEM showing the amorphous layer depth after a 450 °C 30 min VLTA. No amorphous layer regrowth was observed	121
5-3 PTEM showing as-LTP defect densities for material having first received a) no anneal followed by 750 mJ/cm ² , b) no anneal followed by 800 mJ/cm ² , and c) a 450 °C 30 minute anneal followed by 750 mJ/cm ²	122
5-4 PTEM showing LTP material having first received a) no anneal followed by 750 mJ/cm ² , b) no anneal followed by 800 mJ/cm ² , and c) a 450 °C 30 minute anneal followed by 750 mJ/cm ²	123
5-5 SIMS boron profiles analyzing the effect of a VLTA (450 °C 30 minutes) prior to laser annealing.....	124
5-6 Hall effect active boron dose measurements showing the effect of VLTA on deactivation at 750 °C for 5 minutes and 2 hours	125
5-7 Plots showing all three interstitial based phenomenon as a function of the epitaxial defect density.....	126
5-8 SRIM simulation of 15 keV Si ⁺ 1x10 ¹⁵ /cm ² implant	127
5-9 Hall effect active boron dose measurements showing data for material beyond the process window	128
5-10 SIMS boron profiles for material laser annealed beyond the process window and then thermally annealed	129
5-11 SIMS profile showing transient enhanced diffusion of boron in laser melted material following thermal annealing at 750 °C for 2 hours	130
5-12 SIMS profile showing transient enhanced diffusion of boron in laser melted material following thermal annealing at 750 °C for 2 hours	131
A-1 PTEM images showing how variations in measured laser energy density affect the epitaxial defect density.....	137

Abstract of Dissertation Presented to the Graduate School
of the University of Florida in Partial Fulfillment of the
Requirements for the Degree of Doctor of Philosophy

ANALYZING THE THERMAL ANNEALING BEHAVIOR OF LASER THERMAL
PROCESSED SILICON

By

Erik Adam Kuryliw

August 2003

Chair: Kevin S. Jones

Major Department: Materials Science and Engineering

Laser thermal processing (LTP) is one of several novel processes being studied as a replacement to conventional thermal annealing for silicon processing. It involves laser melting of an ion implantation induced pre-amorphized layer to form highly doped ultra shallow junctions. In theory, a supersaturation of interstitials created by the implantation step remains just below the laser-formed junction. Additionally, the possibility exists of quenching in point defects during the rapid liquid phase epitaxial regrowth of the melt region. Since post processing anneals are inevitable, it is necessary to understand both the behavior of these interstitials and the nature of point defects in the recrystallized-melt region since they can directly affect deactivation and enhanced diffusion of dopant in the junction. It is also desirable to understand what role variations in the laser energy density play during post-LTP thermal annealing.

In this study (100) oriented silicon received a 15 keV $1 \times 10^{15}/\text{cm}^2$ Si^+ implant to create a 31 nm continuous amorphous layer. This was followed by a 1 keV $1 \times 10^{14}/\text{cm}^2$

B⁺ or Sb⁺ implant. Some material then received a very low temperature anneal (VLTA) between 400 and 450 °C for up to 2 hours. The surface was then laser melted at energy densities between 730 and 900 mJ/cm² using a 308 nm excimer-laser. It was found that laser energy densities above 800 mJ/cm² melted past the amorphous-crystalline interface and that energy densities less than 750 mJ/cm² were not sufficient to completely melt the amorphous layer resulting in a polycrystalline regrowth. For energy densities within this “process window,” it was observed that there were a continuously decreasing number of epitaxial defects as the energy density increased. This varying epitaxial defect density was observed to be constant for samples that received VLTAs. Post-laser furnace anneals were performed at 750 and 900 °C for up to 8 hours.

It was observed that increasing the laser energy density between 750 and 800 mJ/cm² led to increased dislocation loop formation, diffusion, and dopant clustering after the furnace anneal. It was found that material that received a VLTA prior to laser annealing showed a behavior similar to that of material that received higher energy density laser anneals but without a VLTA, suggesting a correlation between the interstitial related phenomenon and the epitaxial defects. It was also found that the laser melting and recrystallization process itself can serve as a source for interstitials.

CHAPTER 1 MOTIVATION

This work will examine the thermal stability of ultra shallow junctions formed using a novel process called laser thermal processing (LTP). More importantly it will attempt to understand the effects of variations of the laser energy density used during processing. This chapter will discuss the motivation for such a study as well as cover the organization and scope of the work.

Brief History of Semiconductors

Since the invention of the transistor by Bardeen, Brattain and Shockley in 1947 at Bell Labs, the semiconductor industry has seen a whirlwind of advances in the world of computing. Previously computing was limited to the use of vacuum tubes that limited the size and the speed at which they could operate. In 1958, Kilby and Noyce separately invented the integrated circuit (IC) at Texas Instruments and Fairchild Semiconductor Corp., respectively. This allowed the number of transistors within a product to be increased without increasing the number of components on the circuit board by putting all the transistors in one component. Finally in 1971, Intel engineers Faggin, Hoff, and Mazor developed the first microprocessor. Similar to how the IC incorporated more than one transistor into one component, the microprocessor incorporated several processing components, such as the central processing unit, memory, input and output controls, onto one chip [Bel03].

The basic unit used in silicon microprocessors is the metal-oxide semiconductor field effect transistor or MOSFET [May90]. In essence the MOSFET is a current path

that is separated by a capacitor that functions as a switch to turn the current path on or off. The number of parts that make up a MOSFET have increased over the years, and is shown in Figure 1-1, but at its core, the MOSFET is still the same as it was at its inception. The key to increasing the performance and computing power of microprocessors rests in the miniaturization of the MOSFET. The smaller each device is, the more devices that can be put onto one chip, sometimes referred to as a die, and thus the more functions that can be performed at one time. In 1965 Gordon Moore, who later founded Intel with Noyce and Grove, predicted that the number of transistors per chip would double every two years. This prediction became known as Moore's Law [Moo75]. The semiconductor industry has been able to hold to Moore's Law for nearly three decades while in the process overcoming many challenges that were thought to be "brick walls" to the advancement of semiconductor technology. Figure 1-2 shows the trend of Moore's Law.

Shallow Junction Scaling Challenges

In 1977 it became clear that in order to compete with the Japanese semiconductor markets, U.S. manufacturers would have to work together and the Semiconductor Industry Association (SIA) was created. The SIA would later go on to create the Semiconductor Research Corporation (SRC) and Sematech. In addition, in 1992, the SIA introduced its first 15-year National Technology Roadmap for Semiconductors. The purpose of the roadmap was to outline semiconductor research needs so that future challenges could be overcome. The roadmap has been revised several times and in 2000 became the International Technology Roadmap for Semiconductors (ITRS) [Bel03].

One of the challenges outlined by the ITRS is the need to effectively scale the source-drain regions of the MOSFET in a similar fashion to which the gate length is

scaled. Failure to reduce both the depth of the junction and the lateral abruptness introduces high lateral electrical fields beneath the gate region and increases the leakage current in the device off-state. In addition to scaling the physical dimensions of the junction, it is also necessary to adjust the resistance of the source-drain regions so that the drive current of the device can remain high. A typical method of displaying the effectiveness of a shallow junction process technology is to plot sheet resistance (R_s) as a function of junction depth (X_j). Lines on these plots represent the electrical dopant concentration in the crystal. Figure 1-3 and 1-4 show the various technology nodes for junction depth and sheet resistance as defined by the 2000 and the 2002 ITRS, respectively [SIA00, SIA02]. The primary difference between the two is a decrease in the sheet resistances requirements for each technology node for the later roadmap.

Conventional Processing

Conventional junction processing uses ion implantation to introduce dopants into the silicon lattice. For n-type junctions the standard dopants are arsenic and phosphorus. For p-type dopants the primary dopant is boron, but in some applications indium is used as well. The ion implantation process has proven to be extremely reliable due to its control over both the depth of the implant as well as the precise control over the amount of dopant introduced into the lattice. However, this process also creates damage in the form of lattice interstitials and vacancies. In addition, the implanted dopant resides randomly throughout the lattice. A high temperature thermal cycle is necessary to remove the damage and allow dopant atoms enough energy to move to a site where they can be electrically active. It is during this thermal anneal cycle that many of the challenges facing shallow junction technology are revealed. Excessive diffusion of the dopant leading to an increase in the junction depth and a spreading of the lateral

abruptness is often observed as well as a deactivation of dopant leading to higher sheet resistances. These phenomena will be discussed in more detail in Chapter 2 and will represent a bulk of the phenomena that are studied in Chapter 4. Another important phenomenon that occurs during the thermal cycle is the formation of extended defects such as $\{311\}$'s and dislocation loops. These defects, when present at the electrical junction, have been shown to be able to getter metal impurities, which gives rise to electrical trap sites, increase scattering, resulting in a reduction of carrier mobility, and increase leakage currents, leading to a degradation of device performance. These defects will be the focus of Chapter 3.

Laser Thermal Processing

Laser thermal processing allows many of these challenges to be circumvented. By using non-uniform thermal gradients to perform the thermal anneal step, it has been found not only that enhanced diffusion can be avoided, but also that high metastable activation concentrations can be achieved. However, LTP faces many process integration challenges as well as a lack of understanding of how these LTP formed junctions will behave when exposed to additional thermal cycles. At the onset of this work in 2000, there were few known junction process technologies capable of reaching the technology requirements for 2007 node defined by the ITRS. Thus LTP was seen as a critical technology to develop. With the relaxed sheet resistance requirements of the recent ITRS, LTP is no longer as critical a technology for the near future but remains viable as a candidate for far future junctions.

Scope and Organization

This research investigates the effects of thermal annealing on LTP formed junctions. In addition it will look at how variations in the LTP parameters, such as laser

energy density and pre-laser thermal annealing, can affect the behavior of the material during post-LTP thermal cycles. Chapter 2 will introduce the fundamentals and challenges of conventional processing and LTP, including ion implantation and thermal annealing, as well as previous laser based processing research. Chapter 3 will investigate the microstructure behavior of LTP material both prior to and after conventional thermal processing. Chapter 4 will examine the effects of post-LTP thermal annealing on both the diffusion and the activation of dopant. Chapter 5 will discuss the significant observations of Chapters 3 and 4, develop a general theory to explain the behavior of point defects, test this theory, and examine the possibility of trapping point defects during the solidification from melt. Finally Chapter 6 will summarize the findings of this work and suggest future directions of study for laser thermal processing.

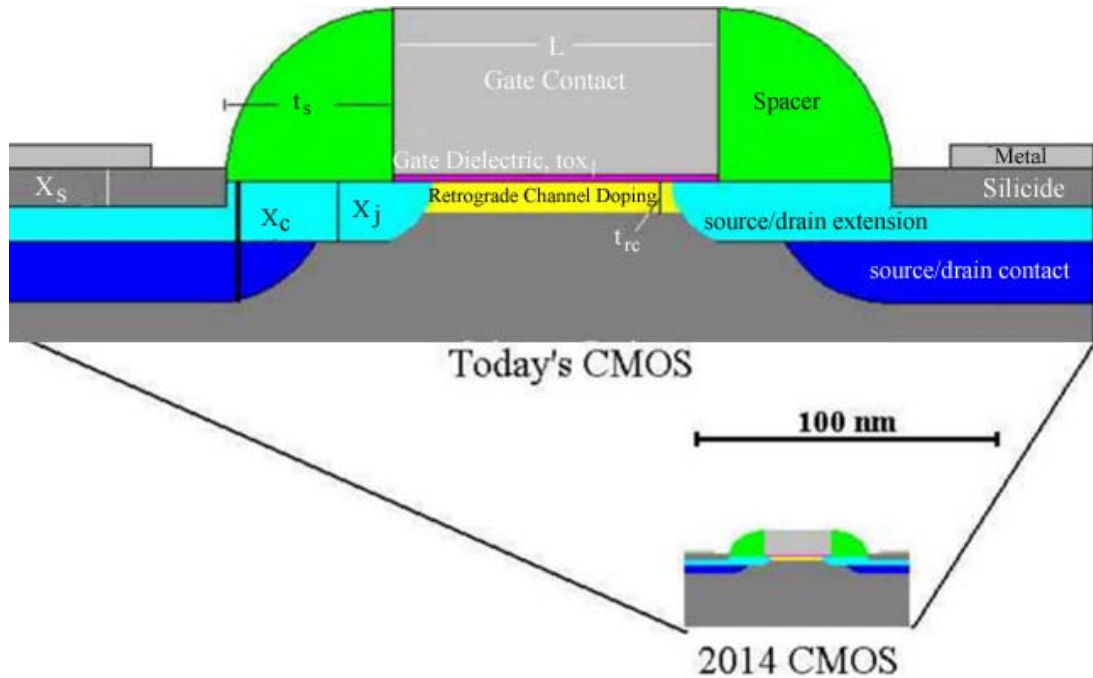


Figure 1-1 Diagram of conventional MOSFET as well as a scaled device that shows the expected dimensions expected for a device in 2014. This work will focus on a technology intended primarily for the source/drain extension area (in light blue) [NIS03].

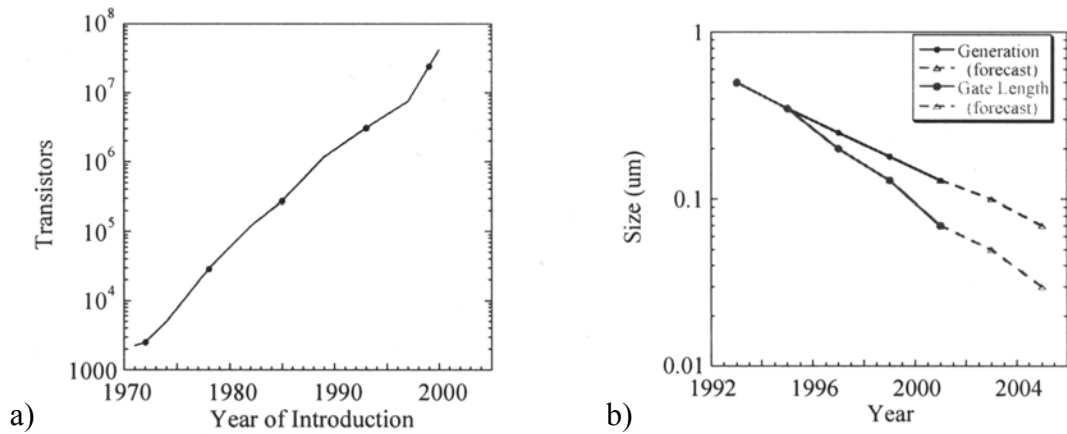


Figure 1-2 Moore's Law describes the expected a) number of transistor per chip and b) size of those transistors as a function of time [Key01].

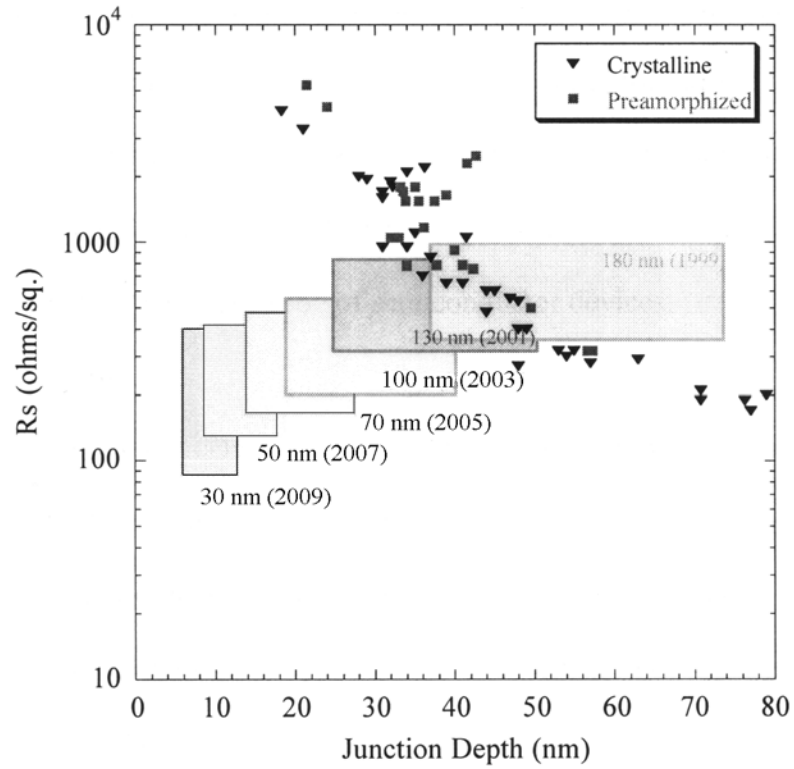


Figure 1-3 Technology nodes for the ITRS 2000 showing required sheet resistances (PMOS) and junction depths. Also included are data points showing the limits of conventional processing for both crystalline and amorphous silicon. Plot created using data from ISA00.

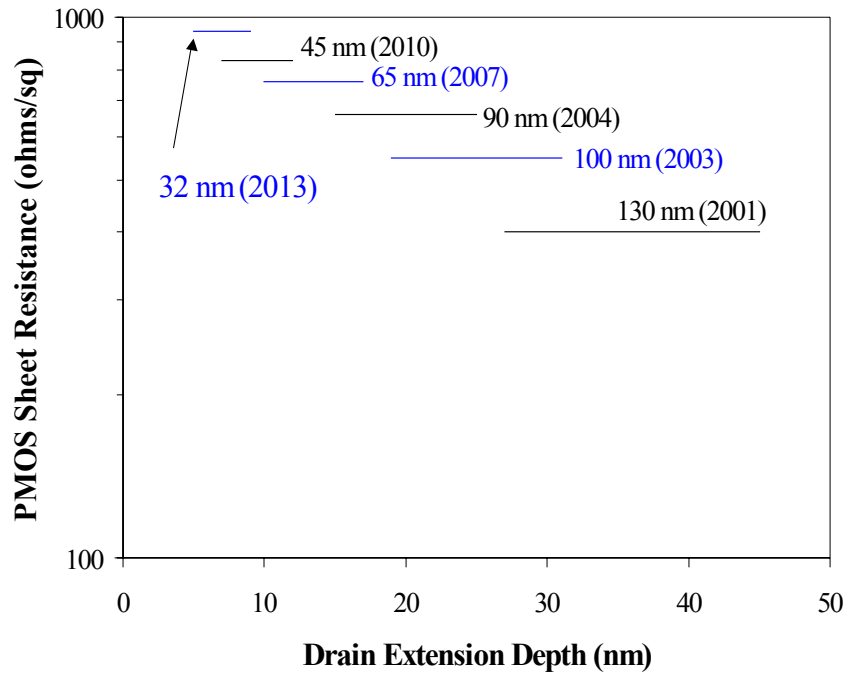


Figure 1-4 Revised ITRS for 2002. Unlike previous ITRS, the 2002 edition merely quoted one sheet resistance per technology node as opposed to a range. The 2002 edition also marked a change in the progressive reduction of required sheet resistances to a gradual increase. Plot created using data from ISA02.

CHAPTER 2 BACKGROUND

This chapter is intended to provide the reader with basic understanding of ion implantation, thermal annealing, and laser annealing as they pertain to the research of this work. In addition, this chapter will review the findings of past research and discuss how these findings were used to develop the experimental approach used in later chapters.

Ion Implantation

The modification of materials using ion beams allows for a number of techniques in semiconductor fabrication processes, including epitaxy, implantation, and etching. The most common method used in industry for introducing dopant into silicon is by ion implantation. Shockley first patented this process for the purposes of creating semiconductor devices in 1954 [Sho54]. Since then implantation has been used for a number of doping steps including poly gate, deep source-drain, shallow source-drain, HALO, threshold adjust, and retrograde wells. Figure 2-1 shows the basic schematic for an ion implanter. The implant tool works by introducing a gas species that contains the desired dopant into the source chamber. The gas is then ionized and extracted, using a voltage potential, from the chamber toward a mass spectrometer. The mass spectrometer isolates the desired ion species by mass-to-charge ratio. The ions that pass through the mass spectrometer are then accelerated toward the target, the silicon wafer in this case. The target is connected to an ion current integrator so that the total ion dose striking the target can be calculated. The topic of material bombardment by energetic particles and the reactions that can occur has been the subject of many theories and experiments for

nearly a century [Cur04, Rut06, Tas89]. One reaction that can occur is disassociation, for the case of multi-atom ions such as BF_2^+ . Recoiling, in which the incoming ion is scattered away, can also occur, as well as sputtering, in which the ion-target collision event causes some of the target atoms to be ejected from the target. Finally, the ion can penetrate the surface and come to rest inside the host. The slow down or stopping of an ion in a host can be broken up into electronic and nuclear stopping and is typically on the order of 100 eV per nanometer [May90]. During electronic stopping, the traveling ion excites or ejects target atom electrons. This form of stopping prevails for lighter ion species and during the initial stages of stopping. Nuclear stopping involves the collision and physical displacement of host atoms. It is this form of stopping that will give rise to the point defect perturbations discussed in the next section. The final concentration distribution of the implanted species is typically modeled as a Gaussian profile, where the peak of the profile is the projected range, R_p , and the spread of the profile is defined by ΔR_p . In reality, implant profiles into single crystalline silicon are rarely Gaussian in nature due to ion channeling. Examples from this work are shown in Figure 2-2. Ion channeling occurs when the ion trajectory is aligned along atomic rows where it experiences a slower rate of energy loss. The result is a profile that is Gaussian towards the surface but is supplemented by a tail that can extend deep into the bulk. Ion channeling can be eliminated by implanting into amorphous layers rather than crystalline, since it effectively eliminates the channels.

Point Defects

In crystalline solids there exist three forms of point defects: vacancies, interstitials, and impurities [Cal97]. As an energetic ion comes to rest within a solid, the number of nuclear collisions increases [May70]. If the energy of these collisions is greater than 15

eV, the binding energy of a silicon atom to its lattice site, displacement of the substitutional atom can occur. This is typically likened to an elastic “billiard ball” reaction. With the imparted momentum from this primary collision, these displaced atoms can in turn displace other atoms in secondary collisions resulting in a collision cascade. For crystalline targets this displacement results in the formation of a vacancy and an interstitial, also known as a Frenkel pair. A vacancy can be defined as the absence of a point from a periodic matrix. An interstitial is the addition of a point to a periodic matrix that rests in a position not normally occupied. The third type of point defect is an impurity, which is an atom of different atomic number than the host lattice. Impurities can sit on either substitutional sites or in an interstitial site and can either be intentionally incorporated (dopant) or unintentionally (contaminant). The maximum equilibrium concentration of impurities that can sit on a substitutional site is defined by the solid solubility. This in turn is typically dependent on the temperature of the system and is described by a phase diagram. Both vacancies and interstitials exist naturally in crystalline solids as defined by

$$N_p = Ne^{\left(\frac{-Q_p}{kT}\right)} \quad (2.1)$$

where N_p is the concentration of point defects (defects/cm³), N is the concentration of lattice sites (atoms/cm³), Q_p is the formation energy of the point defect (eV), k is Boltzmann’s constant (8.617×10^{-5} eV/K) and T is the temperature of the system (K) [Cal97]. The formation energies for vacancies and interstitials have been reported as 4.4 eV and 2 eV, respectively. The corresponding values extracted out to the melting temperature of silicon are $3.5 \times 10^{17}/\text{cm}^3$ and $2.1 \times 10^{17}/\text{cm}^3$, respectively [Tan 85]. The equilibrium values as a function of inverse temperature is shown in Figure 2-3, and are

typically written as C_i^* and C_v^* , the equilibrium concentrations of interstitials and vacancies, respectively. Other observations, however, have shown discrepancies in the true values of these equilibrium concentrations [Sto86, Bra95]. This phenomenon will be particularly important during discussions of transient enhanced diffusion and will form the basis for the theory for quenched in point defects in Chapter 5.

Because of the momentum transfer reaction that occurs during implantation, primary and secondary damage is directly influenced by the mass of the implanted ion. For a given implanted dose, a lighter ion such as boron may leave the implanted host in a highly damaged yet crystalline state, in which a higher mass ion such as phosphorus or arsenic may lead to amorphization. Figure 2-4 shows how different mass ions can create different damage cascades.

Amorphization

As the number of displaced host atoms within an implanted region increases, the long-range order of the crystal matrix is interrupted and the film becomes amorphous. The generally accepted displaced atom concentration needed to amorphize silicon is 10%, or a damage density of $5.0 \times 10^{21}/\text{cm}^3$. Thus depending on the damage concentration profile, it is possible to form amorphous layers that are buried beneath a surface layer that is still crystalline (Figure 2-5). While the long-range order in amorphous films is interrupted there still exists covalent bonding between nearest neighbors due to bond stretching and the formation of 5- and 7-member rings. Amorphous films are typically used to control the as-implanted tail profiles of light ions such as boron since amorphous layers are void of channels found in single crystals. Amorphous layers also have unique properties with regard to their melt temperature and their point defect populations when subsequently recrystallized during thermal annealing.

Thermal Annealing

Following ion implantation, the crystal is highly damaged. There exists a number of Frenkel pairs created by the ion collision cascade in addition to the concentration of the implanted ions themselves. In order to reduce the damage and improve the mobility of carriers, the damage must be removed. This is typically performed using thermal annealing. In addition to promoting the recombination of the Frenkel pairs, the anneal also allows the implanted dopants to move to a substitutional site within the crystalline matrix where they can participate in nearest neighbor covalent bonding and form weakly bound electrons and holes. The diffusion and activation of dopant during this step are particularly important since this controls the junction depth and the resistivity for the shallow source-drain extensions.

Diffusion

During the anneal, dopants diffuse through the material due to several potential gradients. While any type of atom can diffuse through the host matrix, this work will focus on dopant and point defect diffusion through silicon. Fickian diffusion is due to the concentration gradient of the dopant. Point defect enhanced diffusion is driven by the presence of local point defect supersaturations. Fermi-level diffusion results from the formation of vacancy defects and electric field effects are due to gradients of local electric fields on charged ions [May90]. This work will focus on the first two diffusion mechanisms mentioned and each will be detailed below in terms of macroscopic and atomistic behavior.

Macroscopic diffusion

Fick's first law states that in a steady state condition there will be a flux of atoms based on the concentration gradient of those atoms given by

$$J = -D \left(\frac{\partial C}{\partial x} \right) \quad (2.2)$$

where J is the atomic flux [atoms/(cm² sec)], D is the diffusion coefficient dependent on temperature (cm²/sec), C is the concentration of the diffusing species (atoms/cm³), and x is the direction of the gradient (cm). Simply put, on a macroscopic scale, atoms will diffuse from regions of high concentration in a solid to regions of low concentration at a rate defined by D . The diffusion can be determined by

$$D(T) = D_0 e^{\left(\frac{-E_a}{kT} \right)} \quad (2.3)$$

where T is the temperature of the system, D_0 is the pre-exponential constant (cm²/sec), E_a is the activation energy for the diffusion reaction (eV), and k is Boltzmann's constant. See Table 2-1 for a list of D_0 and E_a values for various dopants and other impurities in silicon. Fick's second law can be derived by assuming that the concentration C is time dependent and differentiating Equation 2.2 with respect to time, resulting in

$$\frac{\partial C(x,t)}{\partial t} = D \frac{\partial^2 C}{\partial x^2} \quad (2.4)$$

where t is the time (sec) and D is assumed to be independent of time and space. The change in concentration with respect to time is dependent on the spatial concentration gradient. The diffusivities calculated here will represent the baseline or standard diffusion, and will be used to compare with enhanced diffusion observed due to atomistic effects.

Point defect mediated diffusion

While Fick's laws provide a basis for macroscopic diffusion, they do not consider atomic level reactions and thus have been shown to be inaccurate for many non-equilibrium diffusion conditions. In particular, when diffusion is studied under

conditions where non-equilibrium point defect levels exist, such as during oxidation, nitridation, or following ion implantation, it is found that the diffusivities of diffusing species can be off by several orders of magnitude [Pru74, Fai80].

During diffusion there are four possible methods for a species to diffuse. The first is via substitutional diffusion where the dopant trades lattice positions with a host atom. In this reaction there must be enough energy for both atoms to simultaneously diffuse and is the least favorable reaction. It has been theorized that an alternative diffusion path for substitutional diffusion exists. In this case, a collection of atoms diffuse in a rotation about a single point. In this method the individual barrier energies are minimized. If a vacancy is present next to a substitutional diffusing species, the diffusing atom can move into the vacant lattice site and form a vacancy where the diffusing atom once was. In this reaction, only the energy barrier associated with the diffusing atom moving from its lattice site needs to be met. Finally, the last two mechanisms involve interstitial diffusion. Interstitial and interstitialcy diffusion are both mathematically equivalent. During interstitial diffusion, the diffusing dopant is kicked out of a lattice site by a host atom self-interstitial. The diffusing species then diffuses as a pure interstitial until the process is reversed and a new self-interstitial is created. This process can continue to occur as long as there is an interstitial concentration gradient to promote the kick-out of dopants. During interstitialcy diffusion there exists a binding energy between a diffusing species and a self-interstitial that together occupy a lattice site. By translating the binding energy from one lattice site, leaving behind a substitutional host atom, to a neighboring lattice site, and in the process forming a self-interstitial dopant pair, the diffusing species moves through the lattice.

In silicon semiconductor processing, it has been found that each dopant type exhibits a particular fraction of diffusion that is mediated by either vacancy or interstitial supersaturation [Hu97], where

$$f_v + f_i = 1 \quad (2.5)$$

such that

$$D = (D_v + D_i) \left((1 - f_i) \frac{C_v}{C_v^*} + f_i \frac{C_i}{C_i^*} \right) \quad (2.6)$$

where f_v and f_i are the fraction of vacancy and interstitial diffusion, D is the total diffusivity, D_v and D_i are the vacancy and interstitial mediated diffusivities, and C_i , C_i^* , C_v , and C_v^* are the vacancy, vacancy equilibrium, interstitial, and interstitial equilibrium concentrations, respectively. Note that in reality there is also a fractional diffusion associated with substitutional diffusion but that, in most cases, this value is far below the values of f_v and f_i , and is often assumed to be 0.

Activation

Another purpose of thermal annealing following ion implantation is to allow implanted dopants the energy required for them to diffuse to a substitutional site and become “active.” This means that the dopant atom is participating in the local covalent bonding within the silicon lattice. Due to a difference in the number of valence electrons, the dopant atom creates a weakly bound electron or hole. Since the concentration of electrons and holes dictates the resistivity of the SDE, it is desirable to be able to drive this concentration as high as possible. The basic formula for determining the resistivity, ρ , of material is given by

$$\rho = e(n\mu_n + p\mu_p)^{-1} \quad (2.7)$$

where e is the charge of an electron (-1.6×10^{-19} C), n and p are the electron and hole concentrations (number/cm³), respectively, and μ_e and μ_p are the effective mobility of electrons and holes (cm²/V-s), respectively. In general, however, typically only one carrier type dominates the equation and is dependent on doping. The mobility itself is dependent on scattering from local ionized impurities and shows lower mobility as the active doping concentration increases. Figure 2-6 shows the effect of active dopant concentration on electrons and holes. Figure 2-7 shows the solubility for boron and antimony in silicon. While the phase diagram of dopants in silicon describes the maximum concentration of active dopant under equilibrium conditions, there are phenomena, such as point defect mediated clustering, which can prohibit these concentrations from being achieved. The phase diagram of boron in silicon is shown in Figure 2-8.

Solubility limited activation

Under equilibrium conditions, when the concentration of a solute exceeds the solid solubility predicted by the phase diagram, precipitation of a second phase occurs. This phenomenon has been studied in detail for myriad materials systems. In the silicon-boron system, this precipitate is SiB₃ and is inactive. Discussion exists that perhaps SiB₄ or SiB₆ is the true equilibrium phase [Ase98, Zai01]. For reasons that will become clear in the next section on point defect limited activation, it is difficult to study the precipitation of boron at concentrations of above solid solubility in silicon using conventional methods of either solid source diffusion from the surface or ion implantation-annealing. However, by using rapid liquid phase epitaxy, it is possible to create high concentration metastable systems where solute exists within the matrix above solid solubility without precipitation

occurring. This method has been used by a number of authors to study dopant (B, As, P, Sb) precipitation [Nob89, Rou96, Tak01]. In each case it was discovered that there is a temperature regime above which rapid deactivation can occur. For arsenic and phosphorus dopants, this temperature is as low as 650 °C. In the case of arsenic, the resulting precipitation generates a supersaturation of vacancies. For boron and antimony, the temperature regime for rapid deactivation was 850 °C [Tak01].

Point defect limited activation

In silicon most studies have taken place below the maximum solid solubility of 3%. Under these conditions, one would not expect significant deactivation however, similar to diffusion, activation levels in silicon are highly dependent on local point defect concentrations. The point defects can bind with dopants to form inactive point defect clusters that are submicroscopic and only indirectly observable by electrical and chemical characterization as well as computer based diffusion modeling [Sol96]. This work will focus on boron clustering specifically. A number of different cluster models have been proposed but all observations have shown that increases in the number of either boron or interstitial population will lead to an increase in the amount of boron interstitial clusters (BICs) [Sto97, Co100, Lil00].

Microstructure Evolution

In addition to the diffusion and clustering of dopants and point defects, a number of changes to the microstructure can occur during annealing. Amorphous layers can begin to be recrystallized and a host of extended defects can nucleate and evolve.

Amorphous layer regrowth

Thermal annealing at temperatures greater than 500 °C can result in the recrystallization of amorphous films where the single crystal regions surrounding the

amorphous region act as an epitaxial template [Ols88]. This can lead to recrystallization from two directions for the case of buried amorphous layers. In addition, when recrystallization of amorphous layers occurs, the recrystallized regions are epitaxially grown with a point defect concentration equal to C^* , the equilibrium point defect concentration. Thus damage created during the implantation process is removed. As previously mentioned, this equilibrium value is based on the temperature of the system [Tan85]. For most anneals this results in a point defect concentration that is far below the concentrations observed for non-amorphizing implants. This creates a truncated point defect profile as shown in Figure 2-9. Thus amorphous layers can allow experiments that vary ion implant parameters, such as dose or implant species, without altering the point defect concentration. Following epitaxial recrystallization at low temperatures the only supersaturation of point defects that remain are located in the area beyond the original amorphous-crystalline interface, known as the end-of-range (EOR).

Extended defect evolution

During annealing of ion implanted silicon a number of defect types can form and evolve. These defects were characterized by Jones, and were categorized into five defect classifications [Jon89]. It was also determined that the formation of these defects was affected by several different parameters including ion implant energy, dose, and ion mass. Type I defects are formed by implants that do not exceed the amorphization damage threshold and form at the projected range of the implant and occasionally near the surface. The defects observed are dislocation loops, $\{311\}$ rod-like defects, voids, and stacking fault tetrahedrals. Type II defects are the result of the annealing of amorphous layers either continuous or buried. They are identical to Type I defects except that they are formed at the end of range or just below the original amorphous-crystalline

interface. Type III defects are created as result of poor recrystallization of an amorphous layer. These defects are stacking faults, microtwins, and hairpin dislocations. Type IV defects, also known as clamshell or zipper defects, are the result of a lack of coherency between two crystal interfaces, and are often observed after the recrystallization of buried amorphous layers [Jon86]. Finally, Type V defects are the result of the precipitation of solutes in excess of the solid solubility. Of these defects, this work will be most concerned with Type II and III defects, though care in experimental design will be required to avoid Type IV and V type defects.

For this work the primary Type II extended defects observed are dislocation loops. These defects are agglomerations resulting from the supersaturation of interstitials. Based on computer modeling, it has been proposed that the evolutionary path of these defects during thermal annealing is to first form $\{311\}$ rod-like defects that subsequently unfault to form the dislocation loop [Avc01]. Previous works have shown that these defects can be quite stable even after prolonged high temperature annealing [Pru86] and that their morphology is directly affected by fluxes of point defects [Pan96, Her97]. Thus these defects can be used as a monitor for the presence of point defects. The proximity of these defects to a free surface has been debated [Sol89, Sei97, Li98] without resolution.

Challenges

In the previous sections the fundamentals of ion implantation and thermal annealing were presented with attention to the formation of damage, diffusion of dopants and point defects, activation limits of dopants, and the evolution of amorphous layers and extended defects. This next section will combine these concepts to present a global picture of the challenges that face the scaling of ultra shallow junctions. Namely, the primary method of introducing dopants into silicon is also the cause for both increased

junction depths and increased sheet resistances. It will also present previous findings that attempt to understand, overcome, or circumvent these challenges.

One of the implications of the effect of point defects on dopant diffusion behavior results from the creation of point defects during ion implantation. As previously mentioned, ion implantation creates a supersaturation of both interstitials and vacancies during processing. While many of these Frenkel pairs annihilate during the early stages of annealing, there can still exist an excess of interstitials. While the thermal anneal diffuses these interstitials into the bulk or towards the surface to be annihilated, dopant diffusion can be enhanced over predicted Fickian values during this process. Since this behavior is only observed while the supersaturation of point defects is present it has been termed transient enhanced diffusion (TED). Transient enhanced diffusion has become recognized as one of the greatest challenges to the scaling of source-drain extensions, both vertically and horizontally [Pen85, Sto95].

To understand how to overcome TED, it is first necessary to understand the source of the interstitials, mainly the ion implant. Simple theory stated that while thermal annealing results in the recombination of Frenkel pairs, there would be an excess of interstitials equal to the implanted dose. This became known as the “+1 model.” Later work showed that there was an ion mass effect as well as an implant energy effect that could increase the interstitial supersaturation resulting in an effective plus factor that was different than +1 [Hob00]. Thus accurate predictions of damage cascades during the implant were needed for accurate predictions of the subsequent diffusion. Two of the more popular implant simulators developed were SRIM [Zie02] and UT-MARLOWE [Tas89]. During the annealing of amorphous layers, the recrystallized region is grown

with an equilibrium point defect concentration. Given that the rate of epitaxial regrowth for undoped <100> silicon is greater than 4 $\mu\text{m/s}$ at 700 °C [Ols88], this recrystallization process occurs during the initial ramp of a typical activation anneal of 1000 or 1100 °C. Despite this low level of point defects in the regrown layer, it was found that the amount of TED observed during subsequent annealing could not be explained by merely truncating the implant profile at the amorphous-crystalline interface. This was explained using a “knock on” effect where Frenkel pairs were separated on either side of the a-c interface and thus unable to recombine leaving the excess interstitial in the end of range region [Spe94].

Given that TED is directly correlated to the concentration of point defects above equilibrium levels, it would stand to reason that thermal annealing at higher temperatures, where C^* is higher, would result in less enhanced diffusion. While this theory was found to be true, Agarwal showed that significant enhanced diffusion still occurred during the anneal ramp periods [Aga99]. Even with anneal technology advancements in the ramp up rate, the ramp down rate was limited to the radiative cooling rate of the entire silicon wafer. Current technologies are attempting to utilize localized thermal processing such as flash lamp and laser annealing where only the surface of the wafer is brought to temperature, thus allowing rapid conductive cooling from the bulk of the wafer. Another approach is to use the solid phase epitaxy of amorphous silicon to form shallow junctions, however this process drastically limits the total thermal budget [Bor02, Lin03].

Beyond just understanding TED, it is desirable to be able to accurately predict the diffusion that will be observed for a given process flow in order to reduce the amount of expensive experimental work. One process simulator that has been developed to model

these processes using physical-based models is the Florida Object Oriented Process Simulator (FLOOPS) [Law02]. While transient enhanced diffusion of low dopant concentrations via low point defect concentrations yields results predicted by equation 6 above, upon increasing the damage via higher dose implants, a number of authors observed that the time required for TED to end was often longer than predicted and was dependent on whether the implant was amorphizing [Pen84, Eag96]. This phenomenon was correlated to the formation and slow decay of extended defects, $\{311\}$'s and dislocations loops, that acted as point defect "reservoirs" and slowed the time needed to run out TED [Pen85, Cow86, Pen86, Ser89, Sol89]. Characterization via SIMS also found that an increased formation of BICs, by increasing boron concentration, reduced the number of extended defects due to interstitials being trapped in clusters and not participating in extended defect formation.

Laser Annealing

Since the discovery of the lasers (light amplification by stimulated emission of radiation) by Schawlow in 1958 at Bell Laboratories, science has found a number of uses for them from communication to materials modification. For materials science, it has allowed the investigation of processes that were previously only possible in theory such as the melting of amorphous silicon and non-equilibrium solute trapping in solids. This has in turn opened up new avenues of study for semiconductor process technology such as non-melt laser annealing (NLA) and laser thermal processing (LTP). With the exception of NLA, most of the processes discussed here will pertain to amorphous layers created via the implantation of crystalline layers, the benefit of which will become clear in the following sections.

Melting of Amorphous Silicon

One theory that previously could not be tested was the proposition by Bagley and Chen and separately by Spaepen and Turnbull, that amorphous silicon should have a lower melting temperature than crystalline silicon due to its higher free energy [Bag79, Spa79]. Figure 2-10 shows the free energy curves for crystal, amorphous, and liquid silicon as well as their estimated melting temperatures. It is clear that given the free energy of amorphous silicon, a depression of the melt temperature of 225 to 250 °C with respect to crystalline silicon is expected. However, given the rapid rate of recrystallization of amorphous silicon at elevated temperatures, Figure 2-11, and given the relatively slow rate of heating of conventional furnaces and even flash lamp technologies, it was impossible to verify the true melting temperature of amorphous silicon.

One of the primary advantages offered by laser and electron beam materials modification is the ability to selectively process. This allows heating at rates that are orders of magnitude higher than conventional non-selective annealing since the rate is no longer limited by the bulk material. It was this feature that allowed the study of amorphous silicon melting temperatures by a number of authors, and it was found almost unanimously that the thermodynamic theory was valid. Moreover, it was now shown that given a crystal template upon which to epitaxially grow and by altering the substrate temperature, epitaxial growth from the melt was possible and that the epitaxial growth of silicon could be varied by nearly 14 orders of magnitude, Figure 2-12.

Measuring liquid-solid interfaces

Given the rate of growth of silicon from liquid to solid, it is difficult to monitor the actual rate of the liquid-solid interface during epitaxy. Two methods that have been used

a number of times together are transient reflectance and transient conductance measurements, or TCM. Transient reflectance was first presented by Auston et al. and uses an optical probe reflected off the surface of the wafer [Aus78]. The reflectivity of molten metallic silicon is significantly greater than that of solid silicon, and thus it can be determined when the surface has completely resolidified. However, this technique is only sensitive to the absorption depth of the probe used and says nothing of the position of buried liquid-solid interface. Transient conductance measurements give the molten layer thickness as a function of time by monitoring the conductivity of the surface layer [Gal82]. Given that molten silicon has a 30x higher conductivity than solid silicon, it is easy to determine the relative thickness of the solid and liquid layers but this measurement is insensitive to the exact time at which the liquid layer has been consumed. Thus together TR and TCM can give very accurate measurements of the solid-liquid interface. An example of a TCM measurement is shown in Figure 2-13. While the onset of melting is somewhat discernable via the TCM, it is very clear in the reflectance. Once the layer is fully recrystallized however, the only observable change is in reflectance.

While TCM is not applicable for all laser annealing applications, due to the necessity of having electrical probes in the sample, reflectance measurements provide an excellent non-destructive, in-situ monitoring that can be used for all laser annealing applications. In fact, it is often used for energy density calibration purposes prior to laser annealing since it is known that for a 308 nm excimer laser, the melting temperature of silicon is reached at 1 J/cm^2 .

Altering the solid-liquid interface velocity

From Figure 2-12 it is observed that at any given temperature there is a range over which the epitaxial velocity of silicon can be altered when growing from the liquid phase.

This is accomplished by altering the rate at which heat is removed from the system which is usually done by changing the substrate temperature. However, given the offset in melting temperature between amorphous and crystalline silicon, for a given amorphous layer thickness there exists a range of temperatures that can be created by a laser anneal that will completely melt an amorphous layer without melting into the underlying crystalline region. For purposes of LTP, described later, this range of energy densities is termed the process window. The consequence of this is two-fold. First it indicates that there exists a range of energies for which the melt depth is now independent of the laser energy density. Second, it means that for a given melt thickness, the degree of undercooling can be varied by varying the laser energy density. Poate stated that while different regrowth velocities could be achieved by changing the substrate temperature, ultimately it was the degree of undercooling, with respect to the melt temperature that determined the liquid-solid interface velocity towards the surface [Poa82].

Altering the interface velocity during recrystallization has two effects. The first is that impurities can be trapped in solution at concentrations exceeding solid solubility. This will be discussed more in the next section. The second effect is that the velocity has a direct impact on the morphology of the epitaxial layer. It was shown by a number of authors that if the degree of undercooling exceeded 250 °C, interface velocities of greater than 15 m/s were possible and amorphous silicon could be preferentially formed over single or poly-crystalline silicon. The presence of a crystalline seed requires an even greater amount of undercooling due to the difference in formation energies between hetero- and homogeneous nucleation.

At velocities less than this critical value, variations in either the velocity of the interface or the degree of undercooling can lead to differing densities of epitaxy related defects. Cullis showed that at laser energy densities that were just high enough to obtain single crystal epitaxy, high densities of microtwins were observed that originated from the region of the original amorphous crystalline interface. By increasing the laser energy density, the density of these twin defects decreased. Upon reaching the end of the laser energy density process window, the density of twins was smallest and the few remaining epitaxy defects were occasional hair-pin dislocations that originated at the location of the amorphous crystalline interface and extended up towards the surface along the [113] direction. Once the process window was exceeded, no epitaxial defects were observed [Cul81].

It was shown by Campisano, and later Banisaukas and Baek, that annealing the material at 450 °C for 30 minutes prior to laser melting would result in a more defect free epitaxy layer [Cam80, Ban00a]. Banisaukas determined that this was a result of the planarization of the amorphous crystalline interface and allowed for more uniform template for crystal growth [Ban00b]. It was also shown that any process that decreased this interfacial roughness, including ion dose rate [Ban01] during amorphization and substrate temperature during ion induced amorphization, would garner the same result.

Non-equilibrium Solute Trapping

Much of the early investigations of laser annealing focused on the laser's ability to create highly active layers by using the rapid recrystallization velocity of thin silicon melts on crystal silicon to trap substitutional impurities at levels far above equilibrium. The ability to trap dopants in substitutional sites is based on the interfacial distribution

coefficient, k_0 , or more importantly, the velocity dependent non-equilibrium distribution coefficient, k' ,

$$k_0 = \left. \frac{C_s}{C_l} \right|_{eq} \quad \text{and} \quad k' = \frac{C_s}{C_l} \quad (2.8, 2.9)$$

where C_s and C_l are the concentrations of solute in solid and liquid, respectively [Til53].

It was found that for the resolidification velocities observed for silicon liquid-solid interfaces, on the order of several meters per second, the value of k' often exceed k_0 and begins to approach unity for most dopants. Table 2-2 shows values for equilibrium and non-equilibrium cases.

The upper limits of solute trapping were tested by Larson et al., who observed boron activation levels as high as $1.25 \times 10^{21}/\text{cm}^3$. Using X-ray diffraction, it was found that strains as large as 1.3% existed one dimensionally along the surface normal without the formation of dislocations to relieve the strain [Lar78]. White et al. studied the incorporation of other dopant types using Rutherford Backscattering (RBS) and determined the maximum concentration was anywhere from 4 – 500 times greater than the predicted phase diagram equilibrium solubility. The results are included in Table 2-3 [Whi80]. For less soluble elements, such as indium, it was observed that sufficiently high concentrations, above $1.5 \times 10^{20}/\text{cm}^3$, could lead to imperfect epitaxy and the formation of “cells” [Bae80, Cul81, Nar81]. Moreover, the substrate temperature during laser annealing dictated the morphology of these cells, and thus was dependent on the liquid-solid interface velocity. This supported the theory that meta-stable solubility was in fact determined the quench rate, k' , since high incorporation levels resulted in a smaller cell structure [Cul81]. The dependence of substrate orientation on solute trapping was studied by a number of authors, and again it was found that due to slower regrowth

velocities for $\{111\}$ planes, a smaller concentration of solute was trapped, when compared to $\{100\}$ growth planes [Bae81, Azi87]. Another observed phenomenon was that high concentrations of some dopants (Ga and B) could increase the absorption coefficient of silicon thus leading to lower process window laser energy densities [Bea79, Gab02].

One area that has benefited from the use of lasers for creating meta-stable solubility is the field of dopant deactivation. These studies have also shed light into the mechanisms for dopant-point defect cluster formation. Rousseau et al. performed studies on the deactivation of arsenic. In several studies it was shown that the deactivation of arsenic provides a source of interstitials, suggesting then that arsenic deactivation is via an arsenic-vacancy cluster formation [Rou94a Rou94b, Rou97]. This in turn led to findings on the effect of active and inactive arsenic on carrier mobility [Rou96]. This work was expanded by Takamura et al. who found that deactivation for phosphorus and arsenic occurred at much lower temperatures (600 °C) than observed for boron and antimony (900 °C). It was also suggested that both phosphorus and arsenic deactivate by clustering with a vacancies and releasing interstitials, where as boron and antimony deactivated via precipitation [Tak01]. A similar result was more previously shown using more conventional processing by Dokumaci [Dok95].

Laser Thermal Processing

In recent years two preferred methods of laser annealing have emerged, laser spike annealing (LSA) and laser thermal processing (LTP). The first uses a micro- or millisecond lasers pulse to anneal ion implanted crystalline silicon while the latter uses the benefits of the liquid to solid crystallization discussed in the previous sections. Both processes have shown the ability to create source-drain junctions capable of meeting

future technology nodes [Tal98, Yu99, Mur00, Tal00, Par01, Yam02, Kim02]. In addition, LTP has been shown to be suitable for the formation of uniform buried layers for the control of short channel effects [Ver95, Ver96]. This work focuses on LTP and the challenges it faces. By far the largest challenge facing LTP is integration into the conventional IC process flow. Two of these integration issues are presented below.

Shrinking of the process window

Due to the complexity of films and structures on IC surfaces, a growing issue for all light based annealing including both RTA and LTP, is the formation of interference patterns during the rapid annealing process. This results in non-uniform annealing across the surface of the wafer or die. In addition, one of LTP's primary advantages, the presence of a laser energy density process window, begins to fade due to the complexity of the IC surface. It has been observed that in densely patterned areas of the silicon, there is a shift in the process window, with respect to low density regions, due to differences in both reflectance and absorption of the laser energy. Given that for LTP only one laser pulse is used, this results in a shrinking of the process window range. This is best represented in Figure 2-14. One solution to this problem is the use of phase-switch blanket layers. These layers allow the process window range to be extended to values similar to that for blanket wafers.

Post LTP thermal cycling

Another challenge facing the integration of LTP is its sensitivity to subsequent thermal annealing. Following source-drain formation, a number of thermal cycles, including silicide formation, must be performed. Given the meta-stable condition of the laser formed junctions and the presence of interstitials created during the amorphization implant, there exists the possibility that deleterious phenomenon observed in

conventional processing, such as extended defect formation, enhanced diffusion, and deactivation due to dopant clustering could also be observed for laser formed junctions. In initial studies, enhanced diffusion was observed during post-LTP thermal annealing and was similar in magnitude to conventional processing [Mur00, Jon00, Kur02]. However, extended defect formation was drastically different. It is the purpose of this work to understand how these phenomena differ from conventional processing and how variations in the laser energy density within the process window may affect these phenomena.

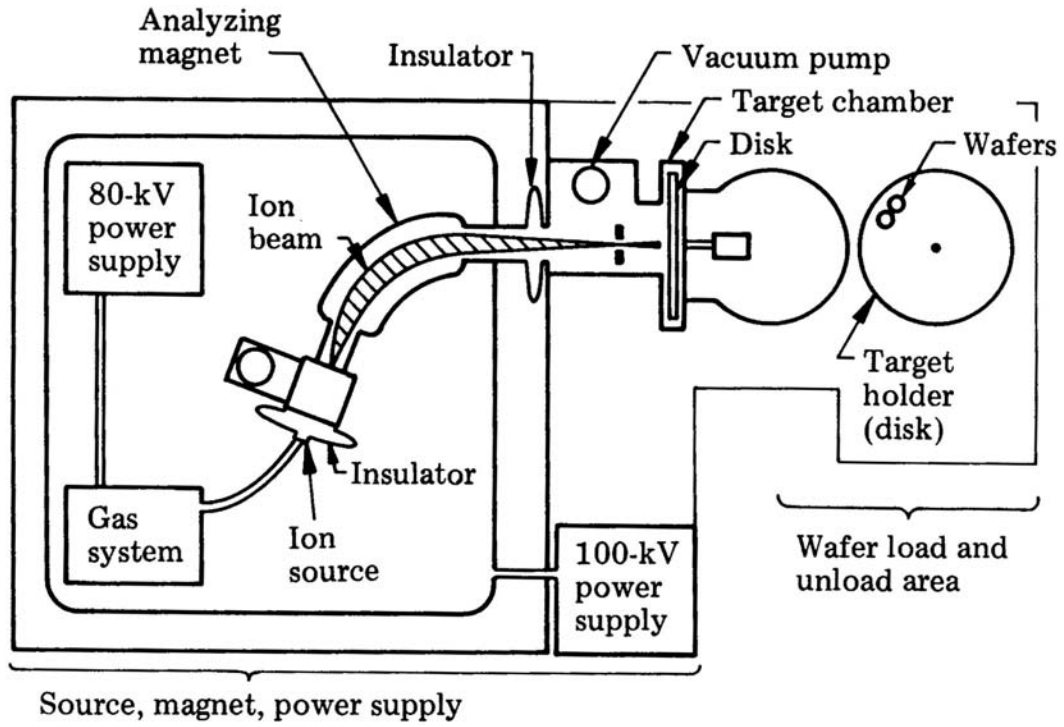


Figure 2-1. Schematic of a commercial ion-implantation system [May90].

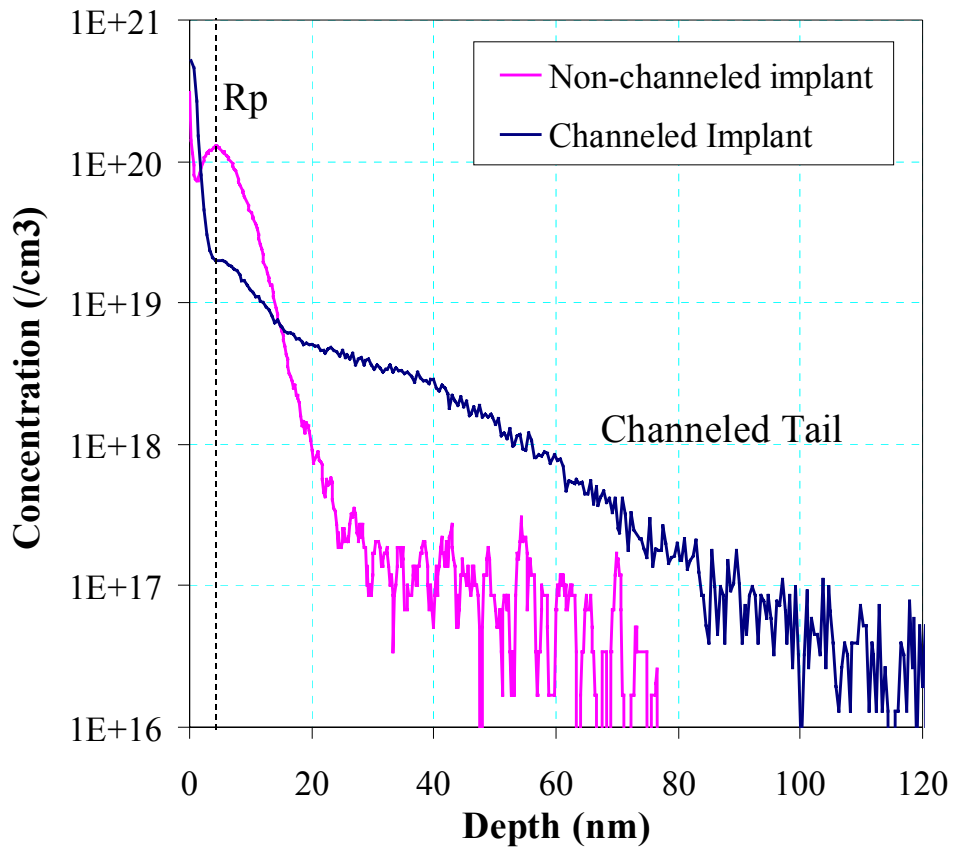


Figure 2-2 Implant profile showing the difference between a channeled implant into crystalline silicon and one implanted into an amorphous layer. The implant is a 1 keV B^+ implant at a dose of $1 \times 10^{14}/\text{cm}^2$. Note that while there is a significant surface spike for both profiles, the projected range of each is still observed to be around 5 nm.

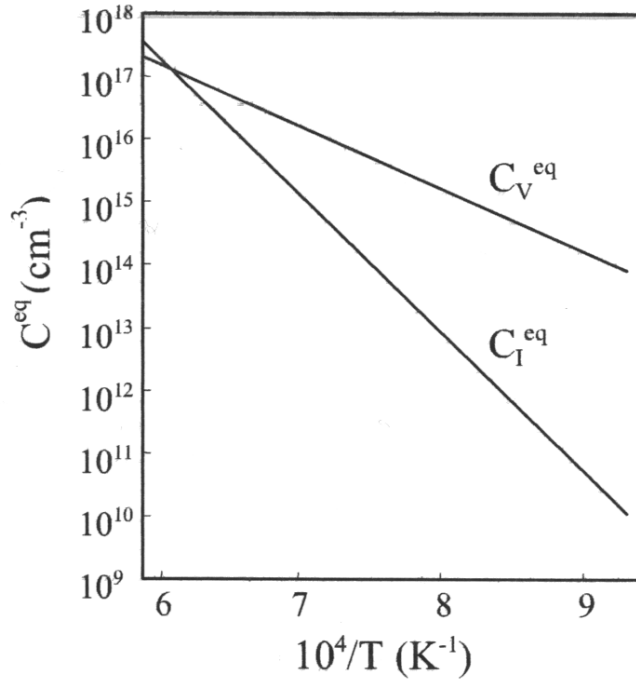


Figure 2-3 Equilibrium concentrations of interstitials and vacancies as a function of inverse temperature. These values dramatically impact the effects of point defect mediated diffusion [Tan85].

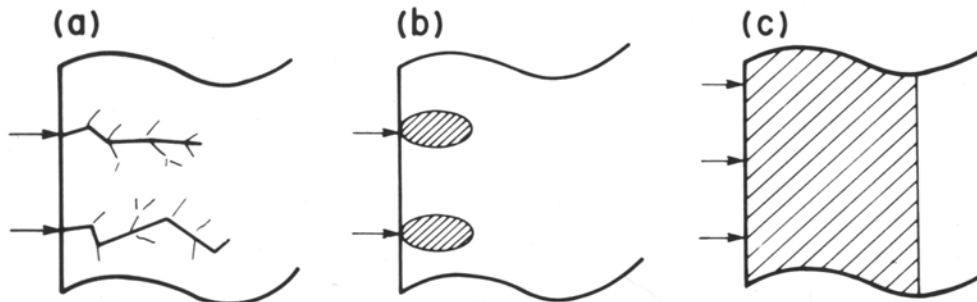


Figure 2-4 Damage cascades created by different ion masses. Light ions will create a) damage along their trajectories without resulting in amorphization. Heavy ions in low doses will create b) isolated amorphous pockets while higher doses result in c) overlapping amorphous regions [Poa82].

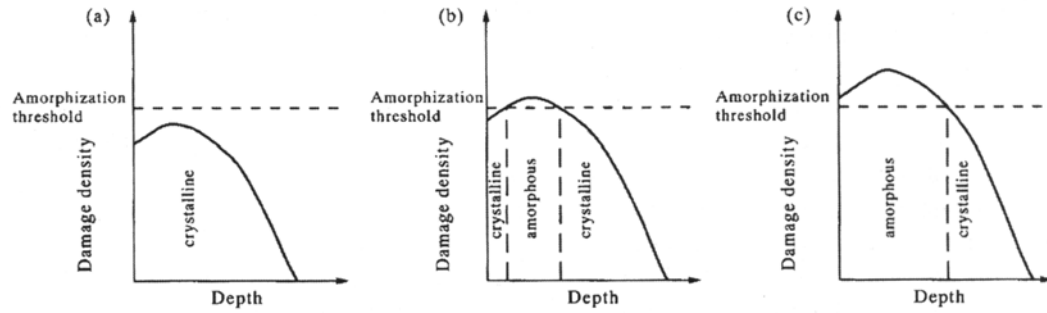


Figure 2-5 Representation of how different concentrations of damage can result in a) crystalline, b) buried amorphous, and c) continuous amorphous layers. Note that each has a slightly higher damage dose [Key01].

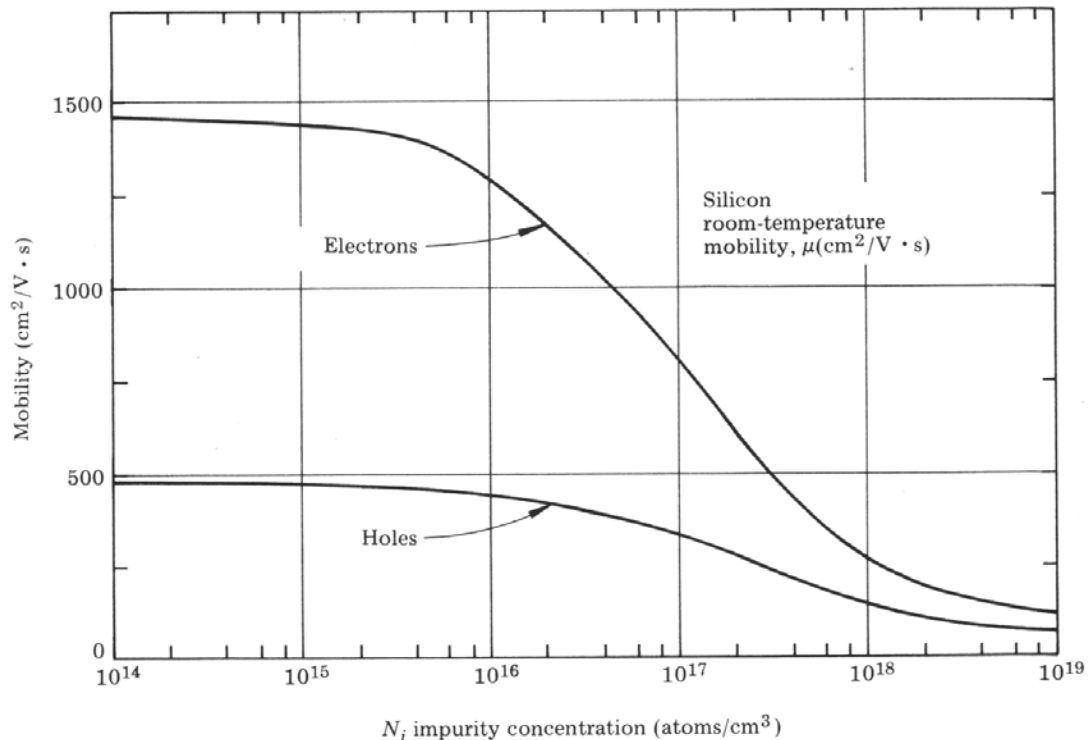


Figure 2-6 Effect of active doping concentration on the mobility of carriers. Note that these values are ideal and assume scattering from ionized impurities only. A number of other factors, such as precipitates or defects (extended and volume) can lower these values [May90].

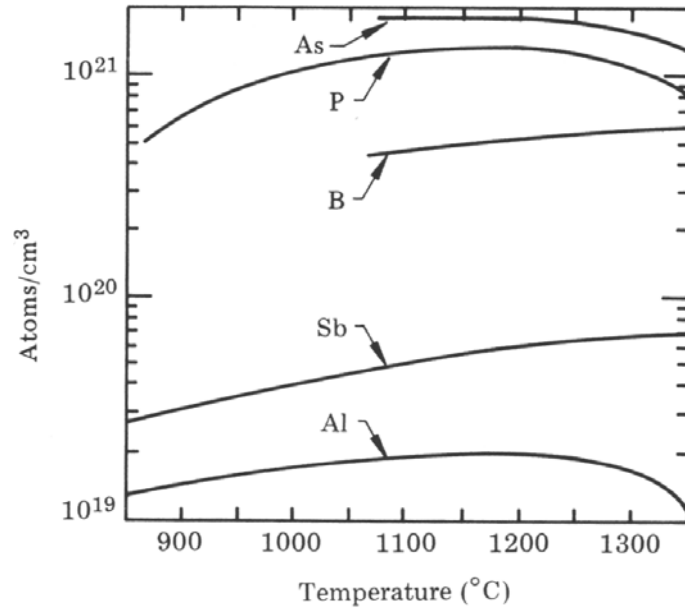


Figure 2-7 Solubility of various dopants in silicon as a function of temperature [May90].

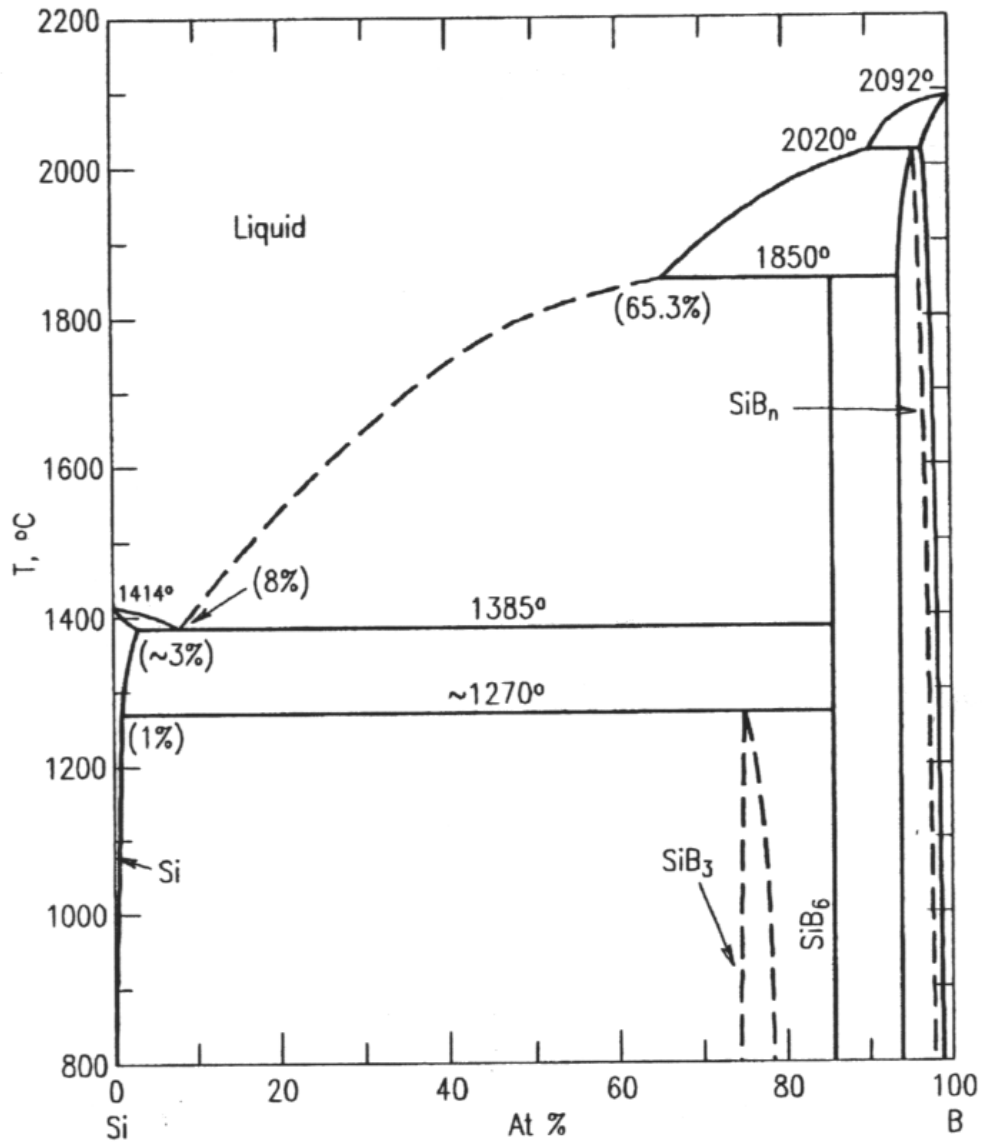


Figure 2-8 Phase diagram of boron and silicon. With respect to semiconductor processing and science, typical boron concentrations are much less than 3%, the solid solubility [Ole84].

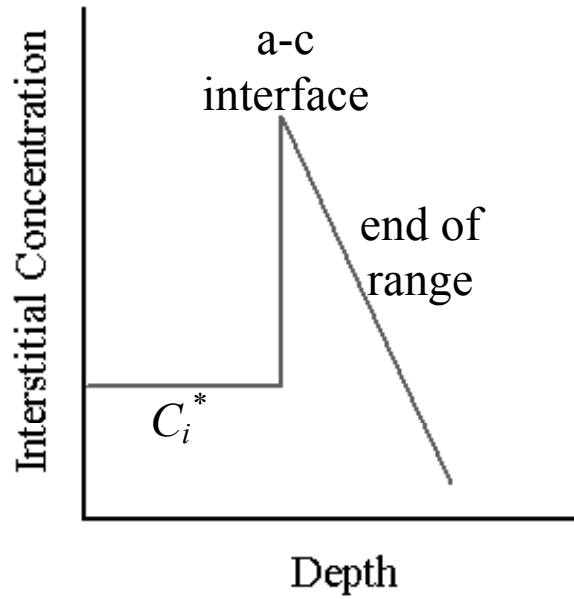


Figure 2-9 Diagram showing a typical interstitial profile following the solid phase epitaxy of an ion implantation induced amorphous layer. The end of range region is the result of the truncated implant tail. During solid phase epitaxy, the epitaxy layer is formed with an equilibrium concentration of interstitials dependent on the anneal temperature (Figure 2-3).

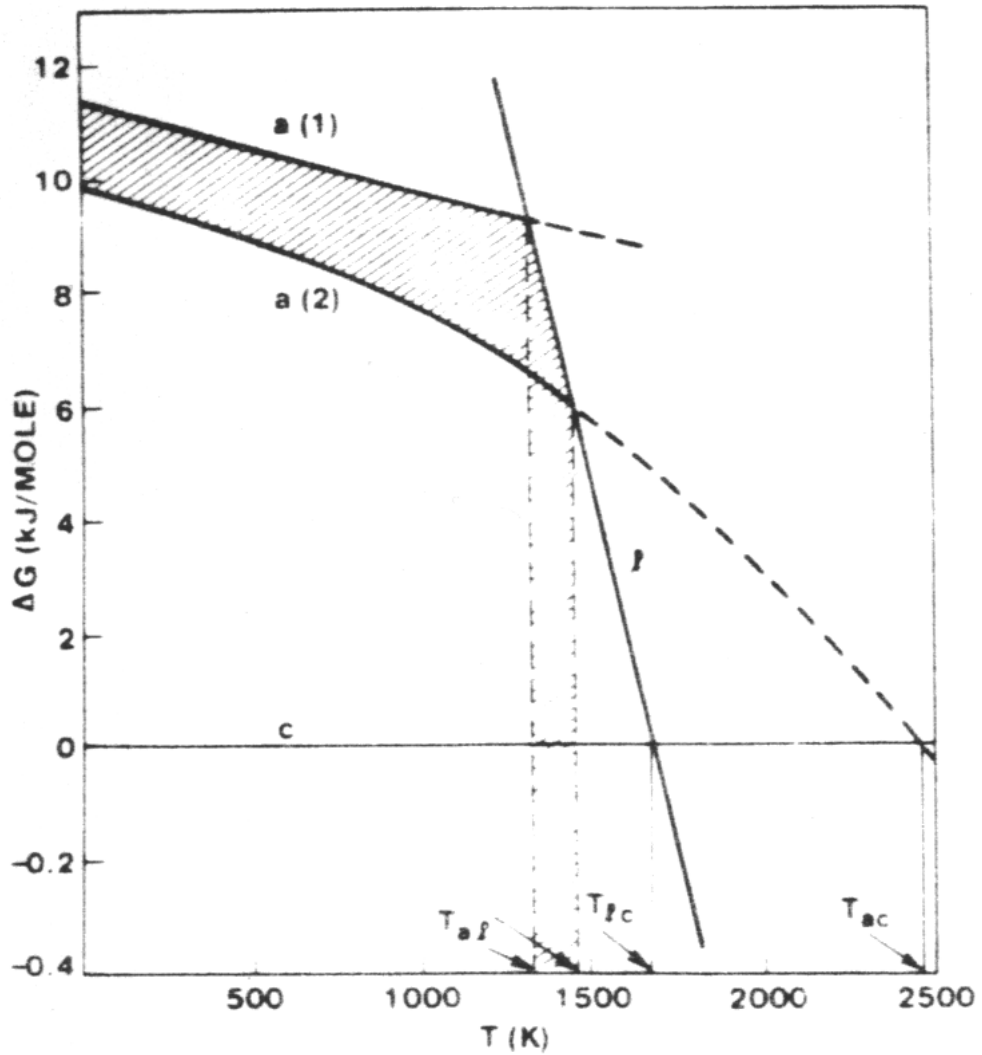


Figure 2-10 Gibbs free energy differences for Si crystal (c), metallic liquid (l), and amorphous (a). The melting temperature for each phase is given by the intercept between two free energy curves. The two amorphous free energy curves are due to two estimates of the heat capacity. The intersection of free energy curves dictates the equilibrium temperature between two phases [Don 85].

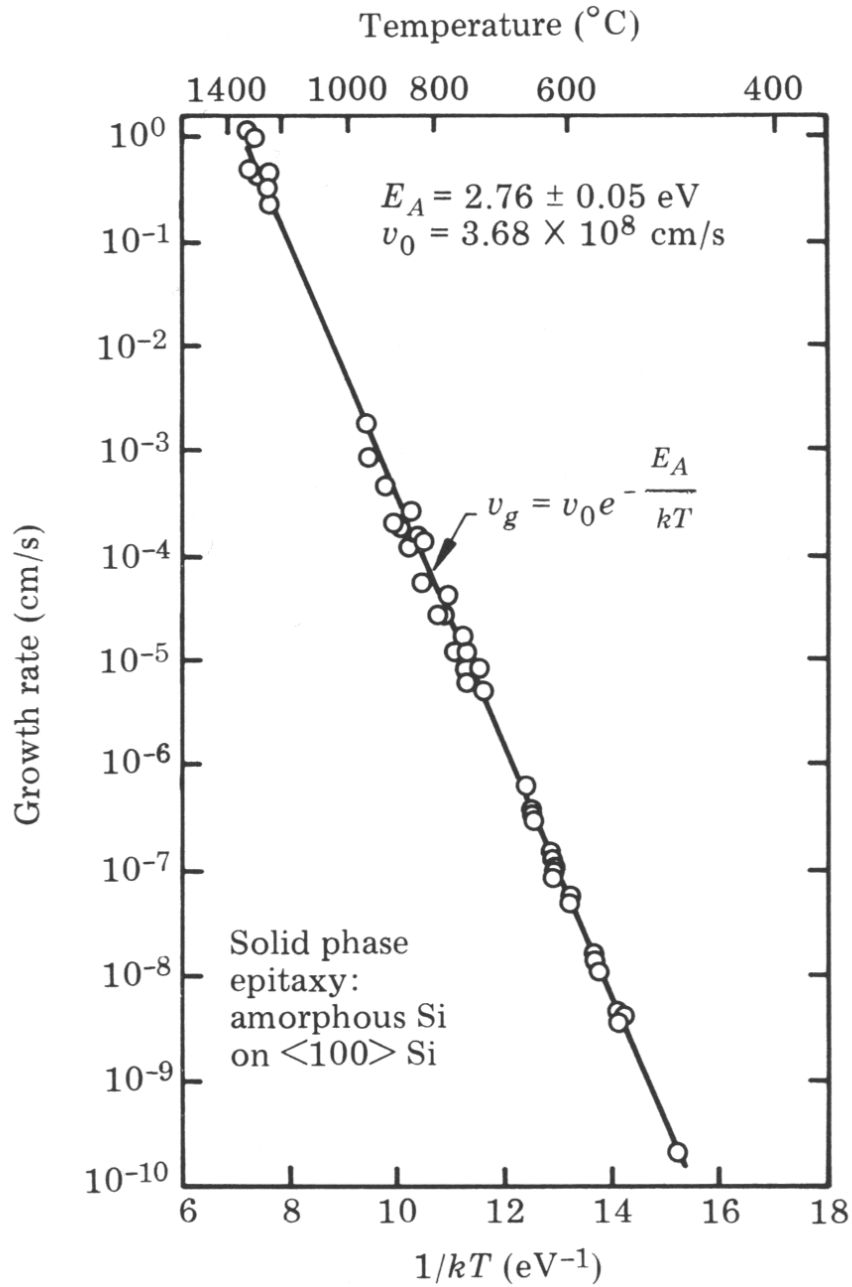


Figure 2-11 Solid phase epitaxy growth rate of undoped amorphous silicon in the $\langle 100 \rangle$ direction as a function of inverse temperature [Ols88].

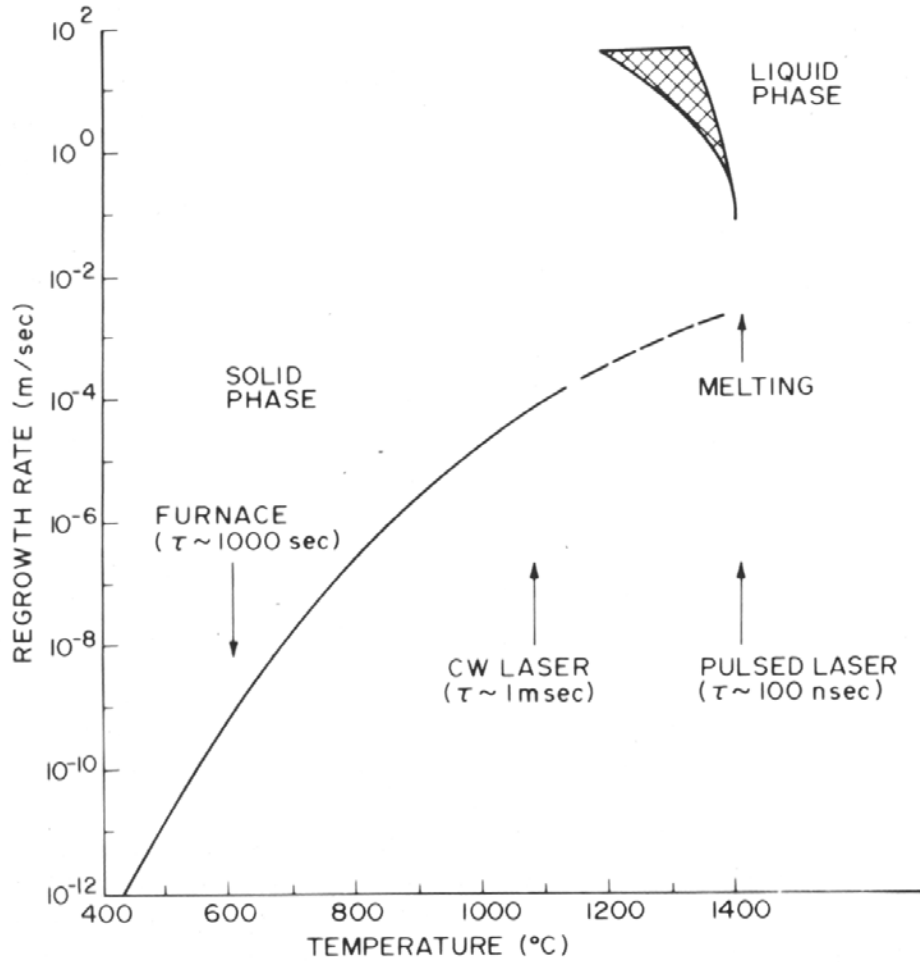


Figure 2-12 Recrystallization velocity of silicon from both amorphous layers (solid line) and metallic melt (hashed area) created by data from furnace and laser annealing. Note that the dashed line above 1250 °C is due to the predicted melting of amorphous silicon due to a higher Gibb's free energy than crystalline silicon [Poa82].

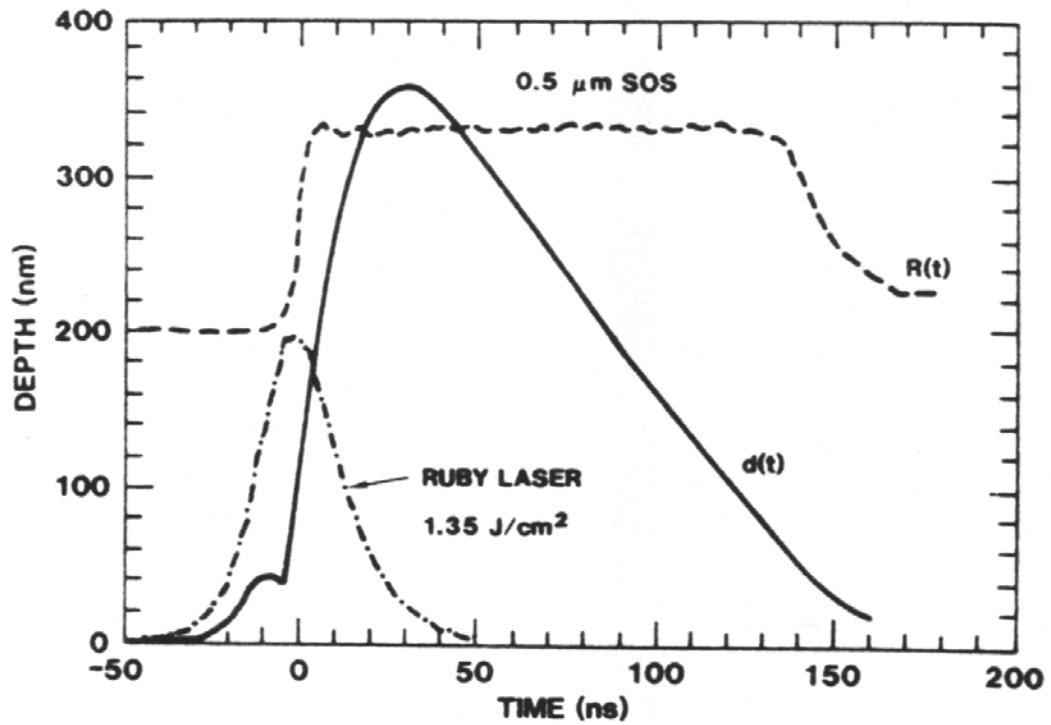


Figure 2-13 An example of transient conductance and reflectance measurement. Note that the reflectance curve $R(t)$, can determine the exact time of both melting and solidification, but only conductance measurement, $d(t)$, can determine the depth of the melt [Pee85].

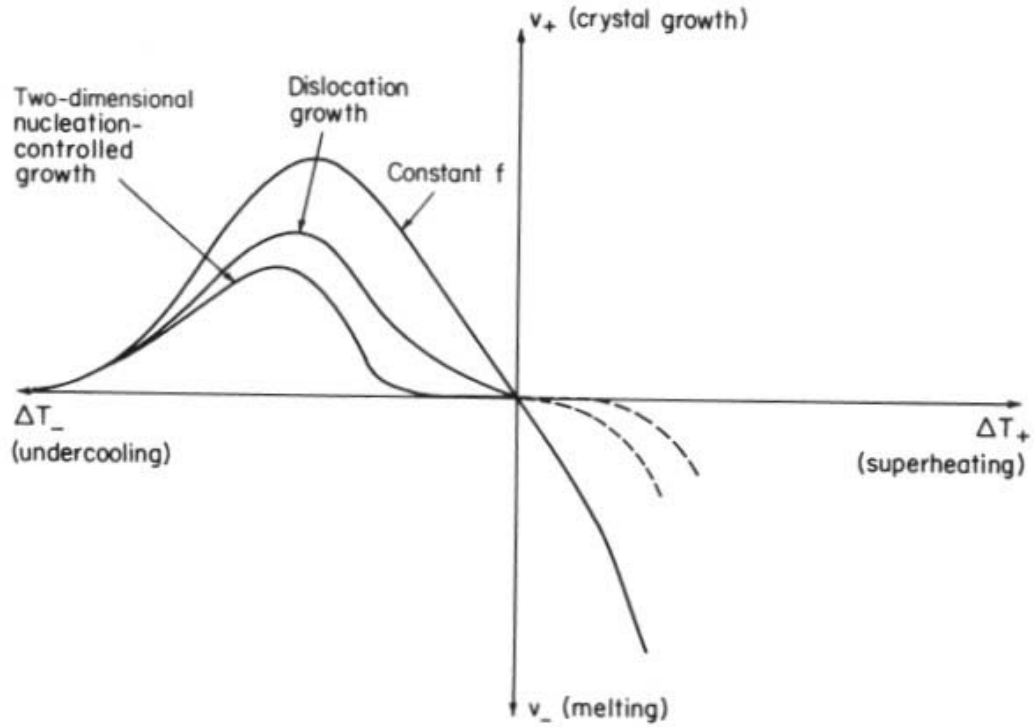


Figure 2-14 Diagram of different undercooling regimes and associated crystal growth velocities. *Constant f* defines the fast growth direction $\langle 100 \rangle$ for silicon, while *Dislocation growth* defines both dislocation and slow growth directions $\langle 111 \rangle$. Note that with sufficient undercooling, amorphous regrowth becomes preferential to crystal growth [Poa82].

Table 2-1 Diffusion parameters D_0 and E_A for dopants boron and antimony in silicon [May90].

Element	D_0 (cm ² /s)	E_a (eV)
B	0.76	3.46
Sb	12.9	3.98

Table 2-2 Equilibrium segregation coefficient, k_0 , and non-equilibrium coefficient, k' , values for dopants. Note that the value for k' is at a solid-liquid interfacial velocity of 2.7 m/s [Poa82].

Element	k_0	k'
B	0.8	~1.0
Sb	0.023	0.7

Table 2-3 Maximum equilibrium solid solubility, C_s^0 , of dopants arsenic, antimony, and gallium, as well as the maximum meta-stable solubility, C_s^{max} , achievable using rapid liquid-solid epitaxy [Whi80].

Element	C_s^0 (/cm ³)	C_s^{max} (/cm ³)
As	1.5×10^{21}	6×10^{21}
Sb	7×10^{19}	1.3×10^{21}
Ga	4.5×10^{19}	4.5×10^{20}

CHAPTER 3 MICROSTRUCTURAL STUDIES

During conventional silicon processing there are a number of thermal cycles that the silicon is exposed to in order to activate dopants, form silicides, and deposit insulators. It is crucial that we understand how laser thermal process (LTP) formed shallow junctions behave when subjected to these thermal cycles. It is also important that we understand how variations in the laser energy density can affect the annealing behavior of these junctions. An experimental outline including steps used to process the material will be presented. Characterization of the material will primarily be performed using transmission electron microscopy (TEM), which will be discussed as it pertains to the presented work. The focus of the chapter will be on the evolution of defects resulting from the laser induced liquid phase epitaxy and those resulting from the supersaturation of interstitials introduced by the pre-amorphization implant. Discussion of these results and those from Chapter 4 will be included in Chapter 5.

Characterization

This chapter will employ two characterization methods, transmission electron microscopy and variable angle spectroscopic ellipsometry. Both characterization techniques will be briefly outlined with emphasis on how each will be used in this work and the limitations of the technique.

Transmission Electron Microscopy (TEM)

Transmission electron microscopy (TEM) uses a high-energy monochromatic electron beam to analyze a material. Unlike most forms of microscopy that rely on

reflected or emitted signals, TEM collects the transmitted electron signal. Therefore samples prepared for TEM must be thin enough to allow the electrons to pass through. Some of the electrons that pass through the sample are scattered by defects or other structures in the material. This scattering can occur by blocking or deflecting the electron beam in the case of three-dimensional particles. It can also occur in strain fields where the Bragg condition is met, which is the case in two-dimensional defects such as dislocation lines. By imaging using either the directly transmitted or deflected electrons these defects or structures can be observed. Using stereological techniques, quantitative data on these defects can be produced. It is important to note that since TEM offers only a projected image of defects in the sample defects at different depths can overlap in the final image. This work will use plan view and cross section TEM to study the evolution of epitaxy related defects and interstitial based dislocation loops.

In addition to high magnification microscopy, when used on crystalline materials, electron diffraction patterns can be obtained that give insight as to the nature of the crystal. For this work, the primary use of diffraction is to determine if the recrystallized regions formed following liquid phase epitaxy are single crystal or poly-crystalline. In addition, imaged structures have characteristic patterns that are observed in the diffraction patterns. In this study, the crystal defects that will be analyzed are dislocations, dislocation loops, stacking faults, and microtwins.

Variable Angle Spectroscopic Ellipsometry (VASE)

Ellipsometry is an optical technique that uses polarized light to probe the dielectric properties of a sample. The most common application of ellipsometry is the analysis of very thin films. By analyzing the change in polarization of the light that is reflected from the sample, ellipsometry can yield information about layers that are thinner than the

wavelength of the light itself, down to a single atomic layer. Depending on what is already known about the sample, the technique can probe a range of properties including the layer thickness, morphology, or chemical composition. For purposes of this work, ellipsometry was used to quickly determine the thickness of amorphous layers created by Si^+ implantation. While not a different material, amorphous silicon exhibits different optical properties than bulk crystalline silicon, making ellipsometry a viable technique. Ellipsometry was also used to ensure that large oxides were not accidentally produced during annealing cycles, conventional or laser. One of the primary limitations of ellipsometry is that the accuracy of measurements is dependent on having smooth interfaces between measured layers.

Experimental Outline

Silicon wafers (<100> n-type and p-type Czochralski 10-20 ohm-cm) received a preamorphizing 15 keV Si^+ implant to a dose of $1 \times 10^{15} / \text{cm}^2$ to create a 32 nm continuous amorphous layer, as determined via both VASE and XTEM. Select wafers were then doped with either a 1 keV B^+ or a 5 keV Sb^+ implant to a dose of $1 \times 10^{14} / \text{cm}^2$. So that electrical characterization of the junctions could be performed, Chapter 4, samples implanted with B^+ used n-type silicon and those receiving Sb^+ used p-type silicon. Background dopant concentrations were less than $1 \times 10^{16} / \text{cm}^3$. All implants were performed on unmasked silicon that received a 10:1 buffered oxide etch prior to implantation. No tilt or twist was used during ion implantation. The wafers were then laser annealed using a 308 nm ultraviolet (UV) XeCl excimer laser. Energy densities used varied from 730 to 850 mJ/cm^2 , with pulse durations of approximately 20 nanoseconds. The spot size of the laser was $5 \times 5 \text{ mm}^2$, however, only the inner $4 \times 4 \text{ mm}^2$

region was used during investigations. This was done so as to eliminate the problems associated with “roll-off” of the laser energy density near the edges of the beam.

Thermal annealing was performed in either a conventional tube furnace or in a rapid thermal annealing (RTA) system. The tube furnace consisted of a 3 inch diameter quartz tube inside a Lindberg furnace. A flowing high purity N₂ ambient was supplied and exhaust gas was run through a liquid bubbler to prevent back flow of gas into the furnace. The system was N₂ purged for 5 minutes prior to beginning the annealing process. The temperature was regularly calibrated using an Omega chromal-alumel type K thermocouple. For this particular system it was found that steady state temperatures were only reached after 3 hours. Samples were placed into a quartz boat and inserted approximately 5 cm into the furnace for 3 minutes before being pushed into the hot zone of the furnace. Thermocouple measurements indicate this area was generally less than 400 °C for a hot zone furnace temperature of 750 °C. The purpose of this was to drive off excess adsorbed water vapor on the sample and boat as well as to allow the assembly to heat up to temperature faster. Some wafers received a thermal anneal prior to laser annealing in order to smooth the amorphous-crystalline interface. These anneals were either 400 °C for 60 minutes or 450 °C for 30 or 60 minutes.

Rapid thermal anneals were performed in an AG Associates RTP system. A flowing high purity N₂ ambient and pre-anneal purge time of one minute was used. For all anneals in this system, a pre-soak anneal of one minute at 250 °C less than the peak temperature was used just before the ramp to peak temperature. The purpose of this pre-soak was to drive off excess water vapor, increase the ramp rate during the ramp to the peak temperature, and minimize over- and under-shoot of the peak temperature.

Plan-view TEM samples were made by coring 3 mm discs from bulk material. The discs were then polished down to approximately 100 microns. The surface of interest, the laser processed side, was protected with wax and a 25% HF-75% HNO₃ etch was dripped onto the backside of the sample until a hole was formed on the surface of interest. The region immediately surrounding this hole is typically of sufficient thickness for TEM. The wax was then removed using n-Heptane and imaged in TEM.

Cross-section TEM samples were formed by cutting the sample into 1 mm wide strips. Two strips were then bound together using a thermally cured epoxy (Gatan Bond) with the surfaces of interest in contact with one another. Additional “dummy” strips of silicon were also bound to either side of sample strips so that the sample was large enough to be manipulated without much difficulty. The silicon-epoxy stack structure was then cored into a 3 mm disc and polished down to 100 microns. A Southbay dimpling tool was then used to form a semi-spherical indentation in the stack, with a final silicon thickness at the bottom of the indentation between 5 and 20 microns. The sample was then milled in a Gatan ion mill at an angle of 14° with two incident 3 keV 0.5 mA Ar⁺ ion beams. The two beams milled from opposite sides of the sample until a hole was formed in the middle of the sample at the surface of interest. The sample was then imaged in TEM.

As-LTP Defect Density

Prior to laser annealing VASE and TEM were used to determine the amorphous layer depth. Figure 3-1 shows a cross section image of the surface prior to LTP. From this image it is determined that the amorphous layer is 32 nm in thickness and continuous to the surface. A high contrast, heavily damaged region is also observable just below the

amorphous layer. Immediately following laser annealing, the samples were analyzed to determine the process window as well as view the effect of the laser energy density on the epitaxial defect density. Figure 3-2 shows the cross sectional morphology immediately following LTP at a laser energy density of 770 mJ/cm^2 . From this image it is observed that the surface region contains a number of defects that extend from the surface to the position of the original amorphous crystalline interface (seen in Figure 3-1). Also note that the damaged layer that existed below the amorphous layer still appears to be present after the laser anneal. If the cross section image of a material laser annealed at 825 mJ/cm^2 , Figure 3-3, is compared to that at 770 mJ/cm^2 , it is obvious that the epitaxial region is free of epitaxial defects and that the high contrast region absent.

Figure 3-4 (a-f) shows a series of PTEM images and diffraction patterns from samples laser annealed at energy densities between 730 to 850 mJ/cm^2 . For samples receiving laser anneals of less than 750 mJ/cm^2 , Figure 3-4a, a heavily defected material is observed with the corresponding diffraction pattern showing a ring pattern associated with polycrystalline grains. This indicates that the melt front did not penetrate completely to the underlying crystalline layer resulting in the formation of polycrystalline silicon grains during the subsequent solidification. For all samples annealed with laser energy densities of 750 mJ/cm^2 and above, polycrystalline ring patterns are not observed. Thus it is determined that 750 mJ/cm^2 marks the start of the LTP process window for this experimental setup. Figure 3-5 shows an enlarged image of the diffraction pattern along the $\{100\}$ and $\{111\}$ zone axis of the polycrystalline sample.

Material laser annealed in the range of 750 to 800 mJ/cm^2 , Figure 3-4 b-d, shows what appear to be type-III regrowth related epitaxial defects in plan view. While there is

no evidence of stacking fault “streaking” in the diffraction pattern or additional spots that correlate to twin spots, Figure 3-6, it is believed that this is due to the fairly thin laser melted region with respect to the slope of the thin sample region. Previous work on thicker laser melted regions by Cullis did show the presence of both streaking and twin spots [Cul81]. It must be noted that occasionally there are additional spots observed believed to be due to double diffraction, but these were not indexed. These spots were not observed for all samples laser annealed between 750 and 800 mJ/cm². It is believed that the absence is again due to the relatively thin region in which the defects exist and were only visible when diffraction was performed at the extreme edges of the sample hole. It is observed that as the laser energy density increases, Figure 3-4 b-d, there is a decrease in the number density of these epitaxial defects. This is believed to be due to a reduction in the liquid-solid interface velocity that is due to less undercooling as shown by Poate et al [Poa82].

For laser energy densities beyond 800 mJ/cm², Figure 3-4 e-f, there are a negligible number of observable defects. Similarly, the additional spots were not observed in diffraction even at the edge of the sample hole, Figure 3-7. It has been previously observed that for samples beyond the process window, defect free epitaxial growth occurs. This was also supported by XTEM in Figure 3-3. Thus it was determined that 800 mJ/cm² marks the end of the process window, giving a total process window range for this material of approximately 50 mJ/cm². Figure 3-8 shows a plot of epitaxial defect density as a function of the laser energy density for materials laser annealed between 730 and 825 mJ/cm².

The rest of this chapter will assume that material laser annealed between 750 and 800 mJ/cm² is in the process window. Additional work was done, Appendix A, to determine the effect of variance of the laser anneal energy densities. It was often observed that the measured energy density for a given setting would vary by as much as ± 15 mJ/cm². It was determined via comparison of plan view TEM that this was in fact due to measurement errors in the energy recording equipment rather than in the power source for the laser. While other authors [Gab02] found that high doses of boron (between 1×10^{15} and 1×10^{16} /cm²) can effectively decrease where the process window begins, but not the range, it was found that 1×10^{14} /cm² within a 32 nm film, or a 3.1×10^{19} /cm³ concentration, was too low to have a noticeable effect when compared to non-doped material.

Comparing Conventional and LTP

Samples that were laser annealed at 0 and 770 mJ/cm² and then thermally annealed at 750 °C for 2 hours were analyzed and compared to understand differences resulting from the laser melt process and conventional processing. Figure 3-9 shows the difference after the anneal both in plan view and in cross section. With respect to the laser-annealed material, two distinct defect types were analyzed, the epitaxial defects originating from the laser anneal and the dislocation loops formed at the end of range by the agglomeration of interstitials introduced by the pre-amorphization implant.

Defect Analysis

Because of the nature in which TEM is performed and the large depth of field of the electron beam, defects located at two different z-positions can appear to occupy the same space in the final projected image. Thus it became necessary to develop a stereological method of defect quantification that allowed distinction between the various

defect types. This method is developed and discussed in Appendix B along with the stereological methods used to quantify both defect types. This method is used throughout this work.

Evolution of EOR Dislocation Loops

The morphology of end-of-range dislocation loops in laser-processed silicon is dramatically different from that of conventional material, Figure 3-9. For LTP material the most noticeable difference is the reduced size of the loops that form, 38 nm for conventionally processed material compared to 17 nm average loop size for laser processed material. In addition, the trapped interstitial density in those loops is also observed to be significantly 80% less, 4.4×10^{13} compared to $8.7 \times 10^{12}/\text{cm}^2$.

Evolution of Epitaxial Defects

If attention is focused to only the evolution of the epitaxial defects, Figure 3-10, it is observed that after a short 6 second anneal at 750 °C, there is an increase in the width and contrast of the visible defects, Figure 3-10a-b. It is observed that the number of low contrast “striped” stacking faults or microtwins decreases leaving behind a number of high contrast line defects. Study of these defects using $\mathbf{g \cdot bxu}$ analysis revealed that while these were indeed planar defects and most likely dislocation lines, they were not purely edge or screw type, making characterization difficult. Additional spots were no longer observed in diffraction. Continued annealing from 6 seconds to 100 minutes at 750 °C shows little change in the defect structure, Figure 3-10 b-d. However, once the anneal time surpasses 2 hours, Figure 3-11 a, a slow reduction in the number of line dislocations is observed. By 4 hours, most of the line dislocations have dissolved, Figure 3-11 a-d. Figure 3-12 shows the quantitative evolution of the epitaxial defect density as a function

of laser energy density for several anneal times at 750 °C. If the same material is instead annealed at 900 °C, Figure 3-13 a-d, a similar but dramatically faster evolution occurs. Therefore if these defects were to be a source of interstitials or a trap site for interstitials, their evolution would affect the local point defect population and therefore possibly affect the dislocation loop evolution.

Effect of Laser Power on Loop Evolution

This next section will analyze how variations in the laser anneal energy density affect the morphology during thermal annealing. Material laser annealed at 750, 770, 800, and 825 mJ/cm² was thermally annealed at 750 °C for 2 hours and imaged in PTEM, Figure 3-14. Note that the first three are within the process window and the latter is beyond. It was observed that as the laser energy density was increased within the process window, there was an increase in the average dislocation loop size from 17 to 21 nm. The dislocation loop number density varied between 3×10^9 and 5×10^9 /cm², with the materials laser annealed at the higher laser fluences (770 and 800 mJ/cm²) having the higher number density. There was an increase in the trapped interstitial concentration from 7.3×10^{12} to 1.2×10^{13} /cm² as the laser energy density increased. However, once the process window was exceeded, both the loop number density and the trapped interstitial concentration drop off, presumably due to the melting of the interstitial rich region just below the original amorphous-crystalline interface. However, the average loops size continues to increase up to 24 nm for the 825 mJ/cm² material.

If the material is further annealed up to 8 hours, Figure 3-15, it is observed that both the 750 and 770 mJ/cm² samples continue to show an increase in trapped interstitial concentration. However, both the 800 and 825 mJ/cm² samples show a drastic

dissolution of their dislocation loops. Figure 3-16 plots the time evolution of the trapped interstitial densities as a function of the laser anneal energy density. It was observed that for a 2 hour anneal at 750 °C, increasing the laser anneal energy density results in an increase of the number of interstitials trapped in dislocation loops. Furthermore, upon continued annealing there is a delay in the formation of the dislocation loops for lower laser energy densities, while those higher in the process window and beyond it show rapid dislocation loops dissolution. Figure 3-17 plots both the average loop size and number density of dislocation loops. While the average loop size is observed to slowly decrease, there is actually an increase in the number density of loops for materials laser annealed at 750 and 770 mJ/cm². This trend is opposite of conventional coarsening, or “Ostwald ripening,” where growth of larger loops are fed by the dissolution of smaller ones. However, if the images are scrutinized it is found that while the average loop size is decreasing, it is due to the formation of smaller loops and not due to larger loops feeding the growth of smaller loops. Thus the new loops are being fed by the release of interstitials from another source, possibly the regrowth related defects.

If the trapped interstitial concentration is plotted as a function of the changing regrowth related defect density, Figure 3-18, it can be seen that there is a trend indicating that as the epitaxial defect density decreases due to annealing, the trapped interstitial density in loops increases. Note that the data for the 800 mJ/cm² material is not included since it started with an epitaxial defect density very near to the TEM detection limit, but for this material there is a dissolution of dislocation loops between 2 and 4 hours. This suggests that it is the presence of these regrowth related defects that captures interstitials and inhibits the formation of dislocation loops. The true nature of these epitaxial defects

could be determined if their density could be altered independent of the laser anneal energy density. This is possible by using very low temperature anneals prior to laser annealing and will be examined in Chapter 5.

Summary

This chapter investigated the formation and evolution of extended defects in laser thermal processed silicon during subsequent thermal annealing. For the implant conditions used, it was determined that the process window was between 750 and 800 mJ/cm². Type III regrowth related defects were observed in material laser annealed within this process window. This defect density was highest at the start of the process window and decreased as laser energy density increased. Once the energy density exceeded the process window, epitaxy defects were no longer observed. During post-LTP thermal annealing, these regrowth defects were seen to evolve and subsequently dissolve after annealing at 750 °C. The time required to anneal out these defects was dependent on their initial as-LTP number density, which was in turn dependent on the laser energy density used for the anneal. Annealing at 900 °C resulted in a more rapid dissolution of these defects.

The evolution of the interstitial mitigated dislocation loops was dramatically different from that of conventionally processed material. While in both processing methods the loops were formed at the end of range, for laser process material the loops were significantly smaller. This suggests either a different evolutionary path for these defects or simply less interstitials available to form these extended defects. This will be discussed more in Chapter 5. When analyzing dislocation loops for laser-processed material, it was found that increasing the laser energy density within the process window

led to more interstitials trapped in loops. Once the process window was exceeded, the trapped interstitial concentration rapidly dropped off. Given that these extended defects are composed of interstitials, it can be reasoned that exceeding the process window results in consumption of the interstitial rich silicon located at the end of range of the pre-amorphization implant and thus reducing the total number of interstitials in the system.

What is unclear is if the increase in trapped interstitial concentration is directly due to the increase in the laser anneal energy density or rather the resulting density of epitaxial defects. Given that for all thermal anneal recipes analyzed in this study there appeared to be a direct correlation between the remaining epitaxial defect density and the trapped interstitial concentration, there is strong evidence that the epitaxial defects, while present, are inhibiting the participation of interstitials in the loop evolution process. This phenomenon will be further discussed and this theory tested in Chapter 5.

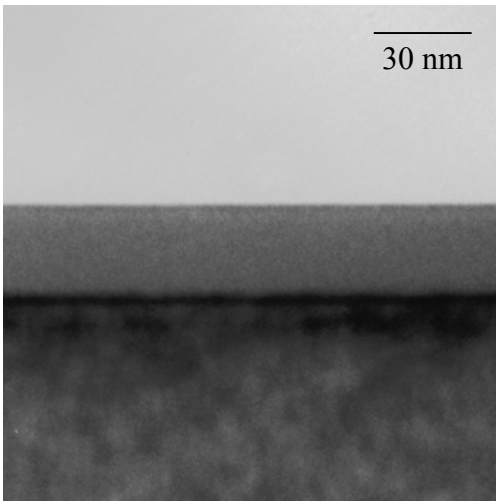


Figure 3-1. Cross section image of material implanted with 15keV Si^+ at a dose of $1 \times 10^{15}/\text{cm}^2$. A continuous amorphous layer is observed between the surface and 32 nm.

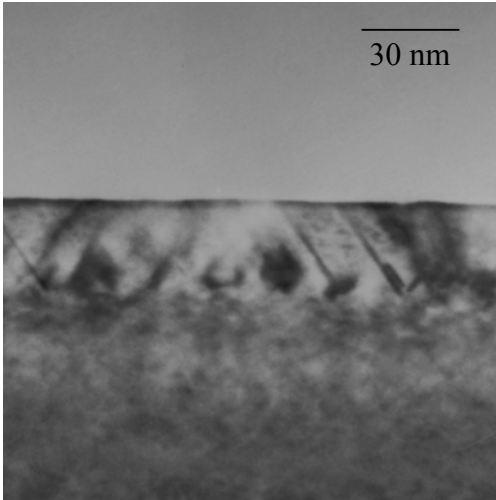


Figure 3-2. Cross section image of material in Figure 3-1 laser annealed at 770 mJ/cm². Note the presence of twins and faults that span from the previous location of the amorphous crystalline interface up to the surface. (Implant conditions: 15 keV Si⁺ 1x10¹⁵/cm², 1 keV B⁺ 1x10¹⁴/cm²)

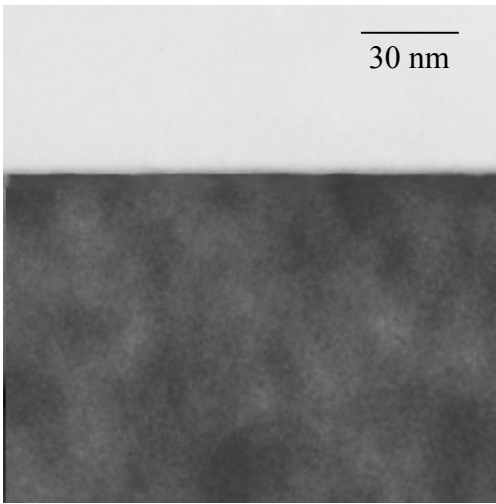


Figure 3-3. Cross section image of material in Figure 1 laser annealed at 825 mJ/cm². Note that it is impossible to determine the depth of the melt due to the lack of defects or residual damage from the implant. (Implant conditions: 15 keV Si⁺ 1x10¹⁵/cm², 1 keV B⁺ 1x10¹⁴/cm²)

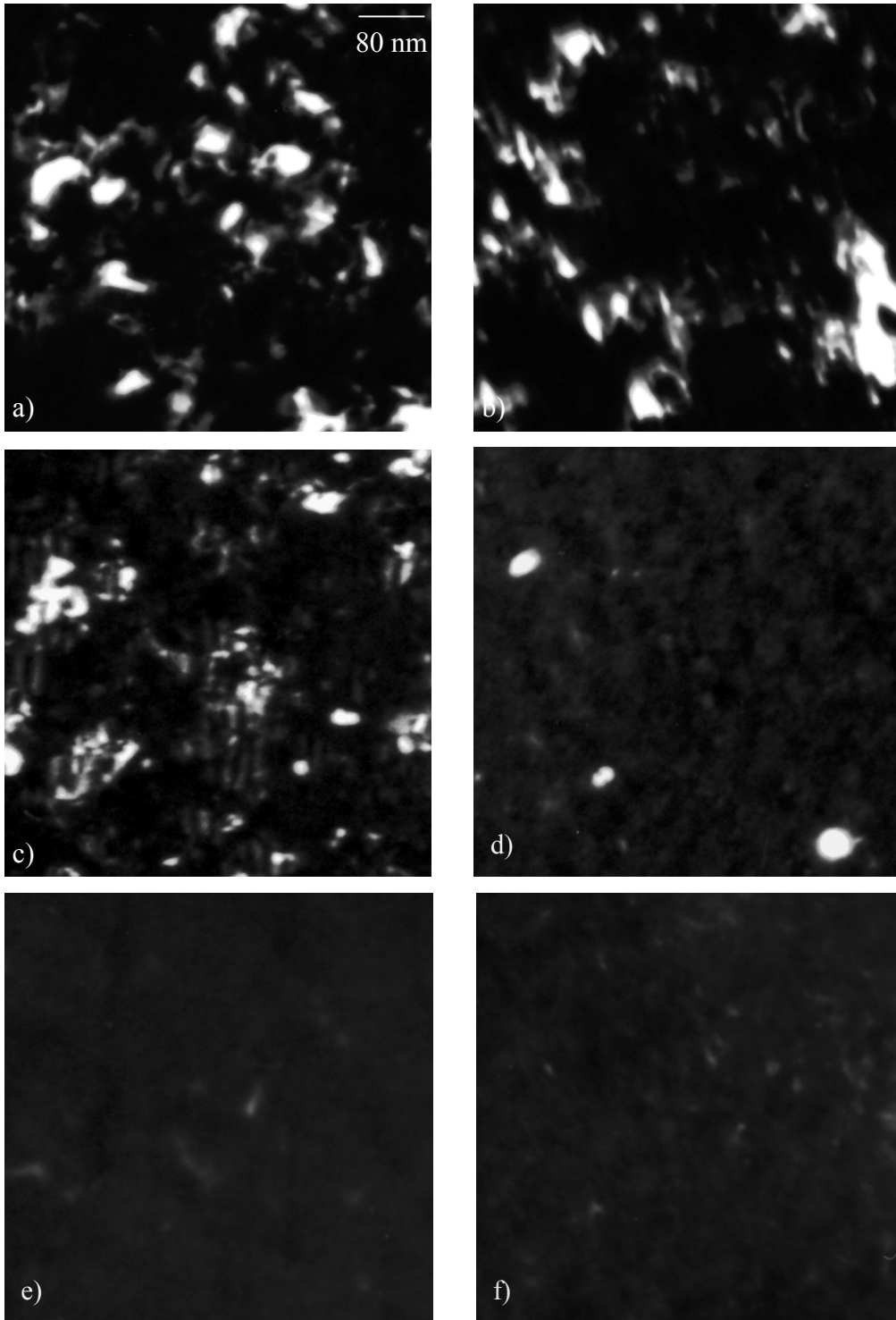


Figure 3-4. Plan view image of material laser annealed at a) 730, b) 750, c) 770, d) 800, e) 825, and f) 850 mJ/cm². Based XTEM in Figure 3-2, what are believed to be dislocation lines, stacking faults, and twins are observed. (Implant conditions: 15 keV Si⁺ 1x10¹⁵/cm², 1 keV B⁺ 1x10¹⁴/cm²)

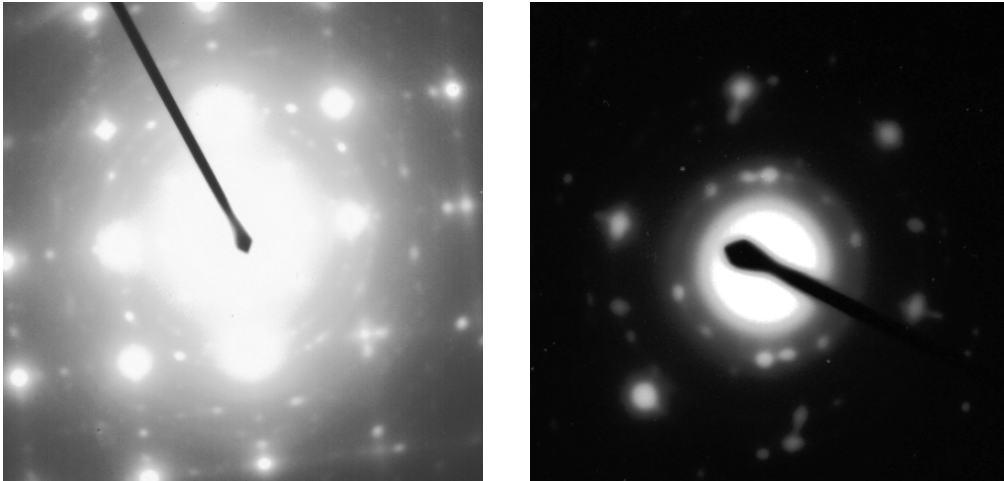


Figure 3-5 Diffraction pattern of 730 mJ/cm^2 material showing a poly-crystalline ring pattern. This indicates that the melt did not completely consume the amorphous layer, and that this laser energy density is below the process window. (Implant conditions: $15 \text{ keV Si}^+ 1 \times 10^{15}/\text{cm}^2$, $1 \text{ keV B}^+ 1 \times 10^{14}/\text{cm}^2$)

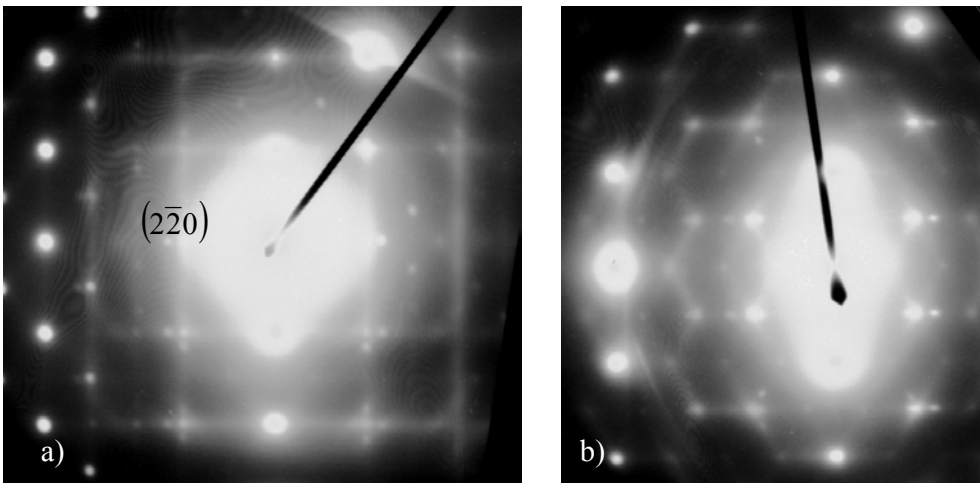


Figure 3-6 Diffraction pattern of 770 mJ/cm^2 material observed down the a) $\{100\}$ and b) $\{111\}$ zone axis. Additional spots are observed but these do not match those typically observed for twins, which are normally observed to be a reflection across the $\{111\}$ -type twin boundary. (Implant conditions: $15 \text{ keV Si}^+ 1 \times 10^{15}/\text{cm}^2$, $1 \text{ keV B}^+ 1 \times 10^{14}/\text{cm}^2$)

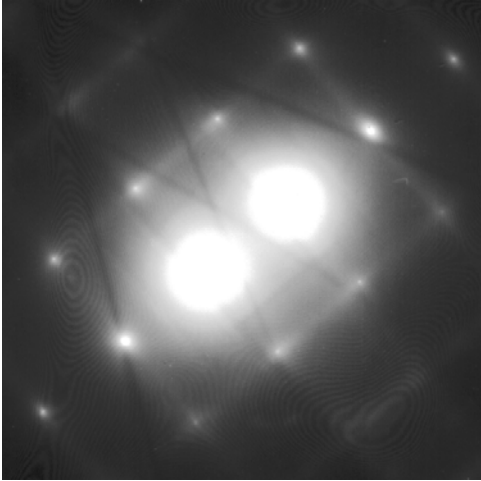


Figure 3-7 Diffraction pattern of 825 mJ/cm² material observed down the {100} zone axis. No additional spots or streaking is observed. (Implant conditions: 15 keV Si⁺ 1x10¹⁵/cm², 1 keV B⁺ 1x10¹⁴/cm²)

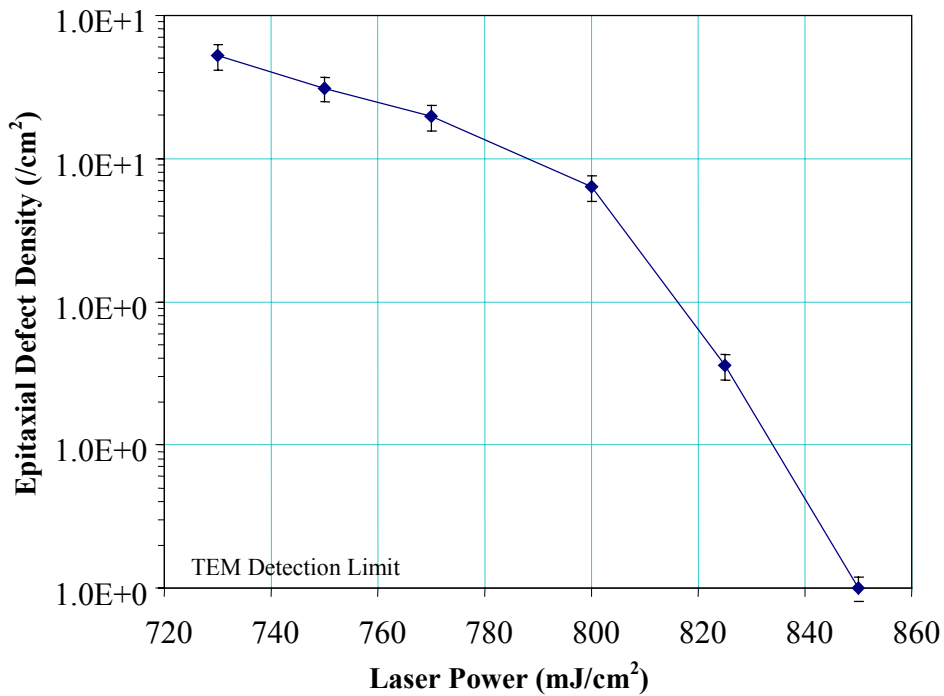


Figure 3-8 Epitaxial defect density as a function the laser energy density. Once the process window is exceeded at 800 mJ/cm² the defect density drops off rapidly towards the TEM detection limit of 1x10⁷/cm².

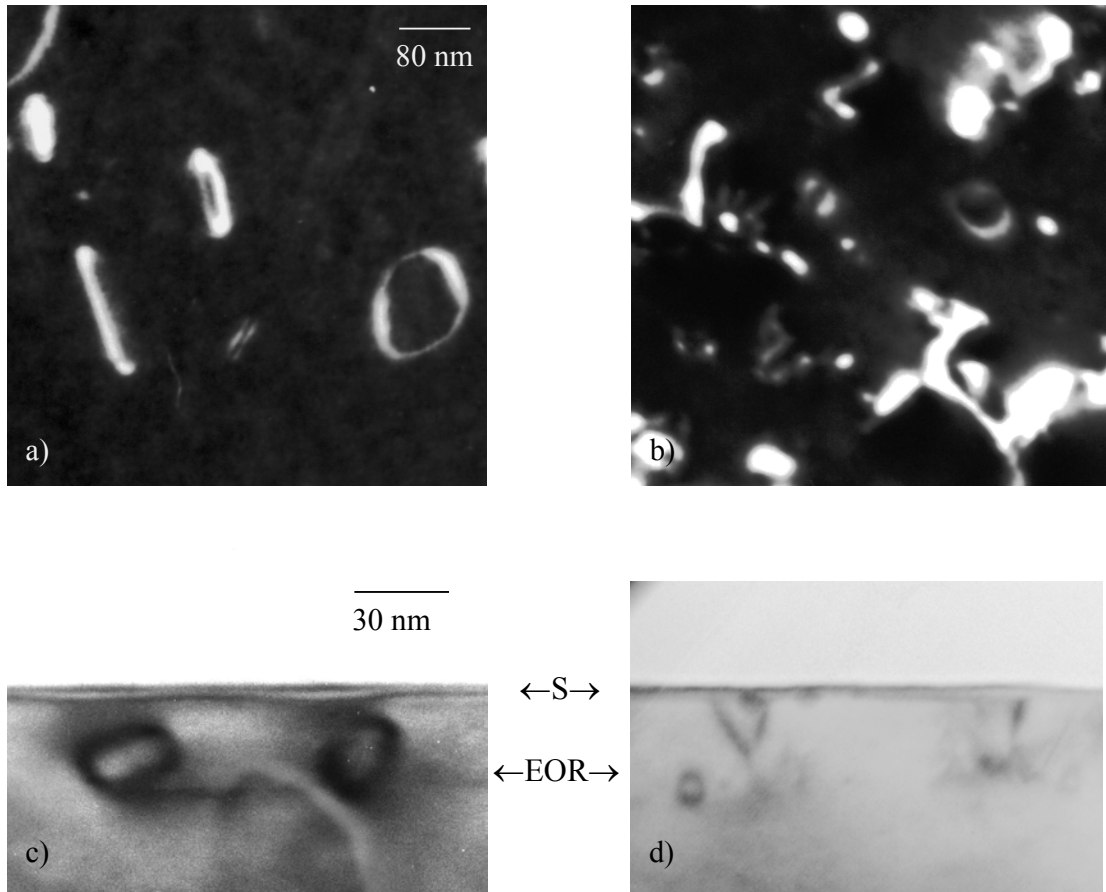


Figure 3-9 Images comparing defect evolution in plan view (a, b) and in cross section (c, d) for conventionally processed material (a, c) and material having received a laser anneal of 770 mJ/cm^2 (b, d) prior to thermal annealing. Both material sets were annealed at $750 \text{ }^\circ\text{C}$ for 2 hours in a furnace. The conventionally processed material shows larger dislocation loops than the laser annealed material. Loops form at the end of range for both material sets. (Implant conditions: $15 \text{ keV Si}^+ 1 \times 10^{15}/\text{cm}^2$, $1 \text{ keV B}^+ 1 \times 10^{14}/\text{cm}^2$)

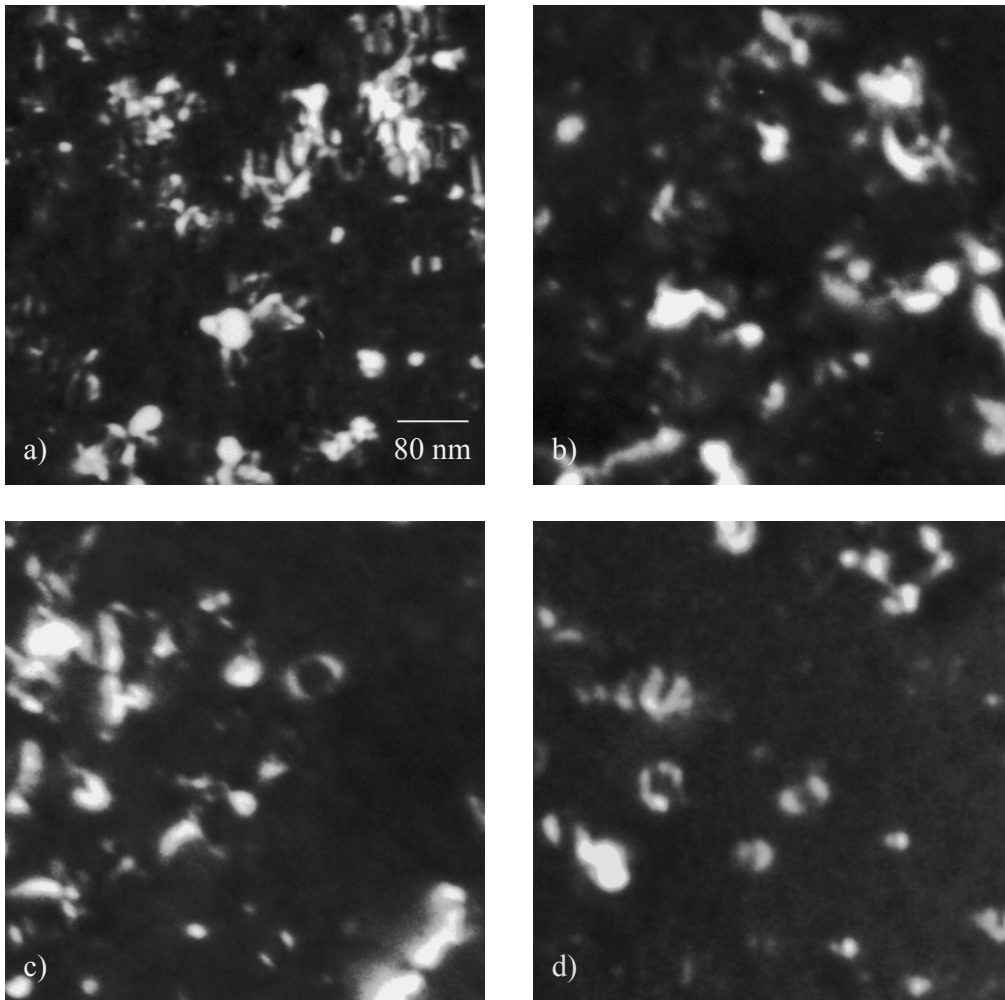


Figure 3-10 Series of plan view images showing the evolution of defects in material laser annealed at 770 mJ/cm^2 and then subsequently thermally annealed at $750 \text{ }^\circ\text{C}$ for times of a) 0 s, b) 6 s, c) 60 s, and d) 100 min. A shift in contrast is observed between 0 and 6 seconds. It is believed this is due to the annealing of out of faults and twins. After 6 s the additional spots observed in as-LTP diffraction material were no longer seen. (Implant conditions: 15 keV Si^+ $1 \times 10^{15}/\text{cm}^2$, 1 keV B^+ $1 \times 10^{14}/\text{cm}^2$)

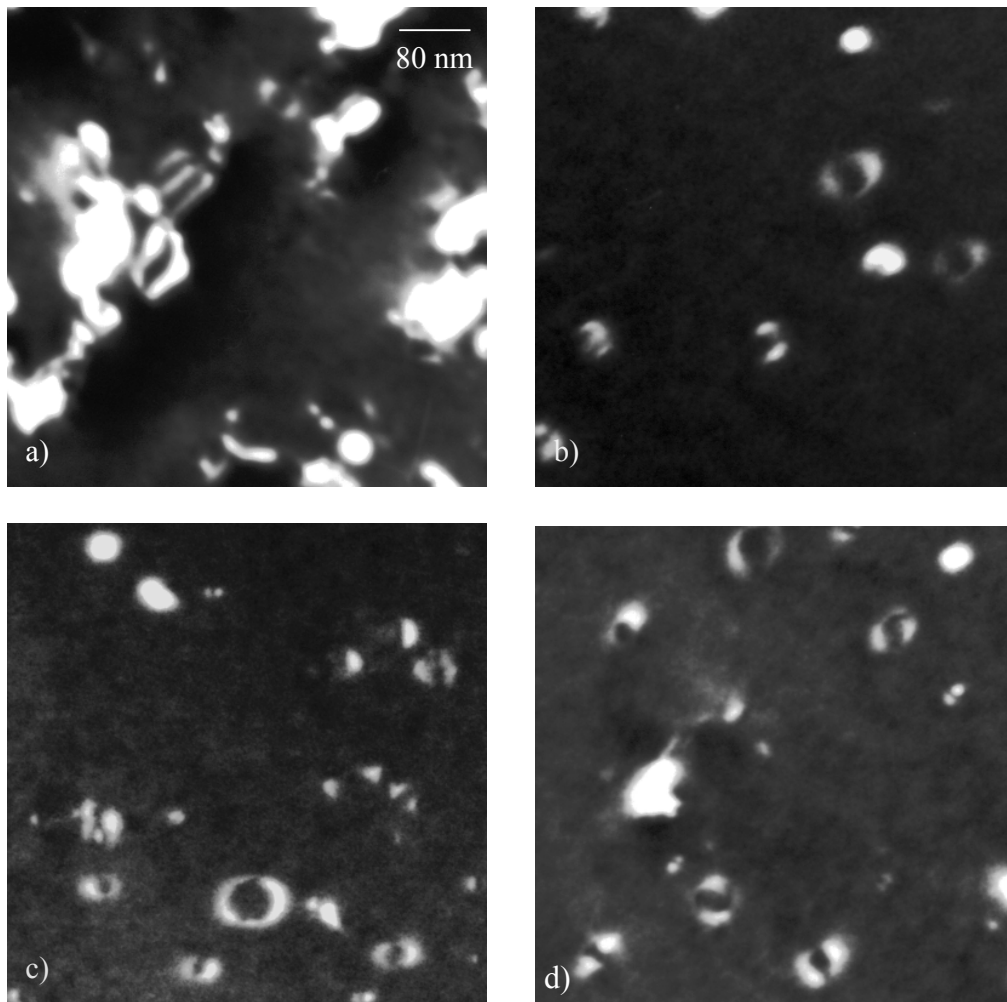


Figure 3-11 Series of plan view images showing the evolution of defects in material laser annealed at 770 mJ/cm^2 and then subsequently thermally annealed at $750 \text{ }^\circ\text{C}$ for times of a) 2 h, b) 4 h, c) 6 h, and d) 8 hours. For this material set the epitaxial defects are completely dissolved between 2 and 4 hours. (Implant conditions: $15 \text{ keV Si}^+ 1 \times 10^{15}/\text{cm}^2$, $1 \text{ keV B}^+ 1 \times 10^{14}/\text{cm}^2$)

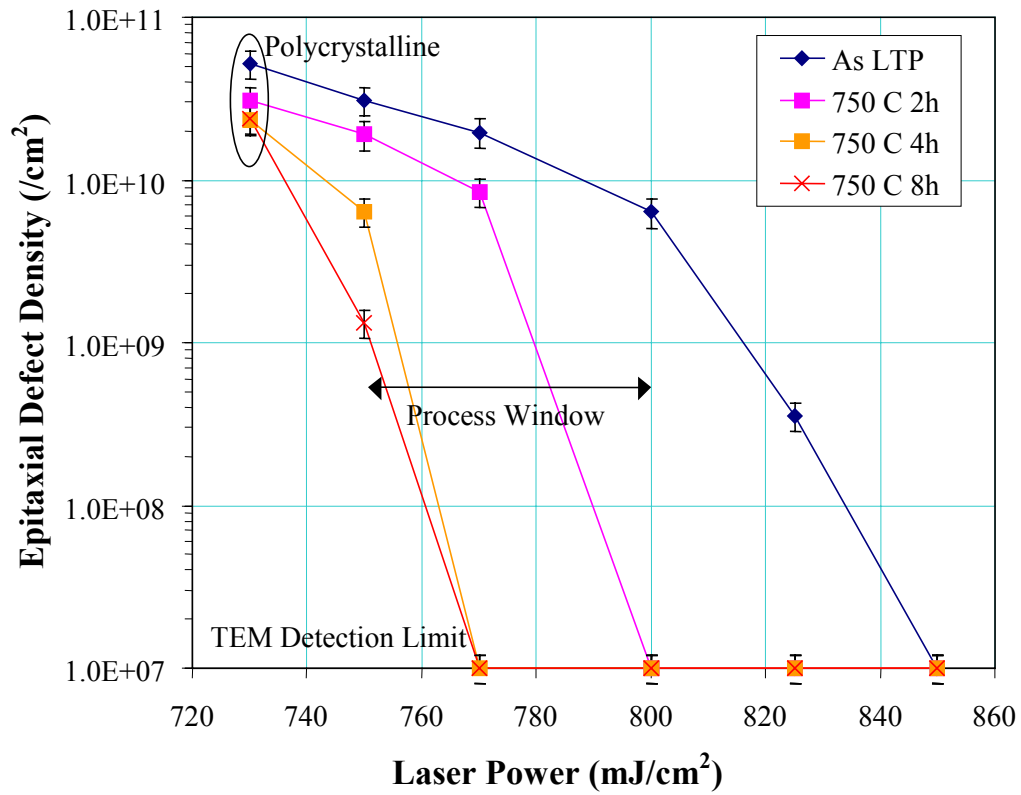


Figure 3-12 The evolution of the regrowth related defect density as a function of laser energy density at 750 °C. The initial as-LTP density determines the time required to dissolve the defects.

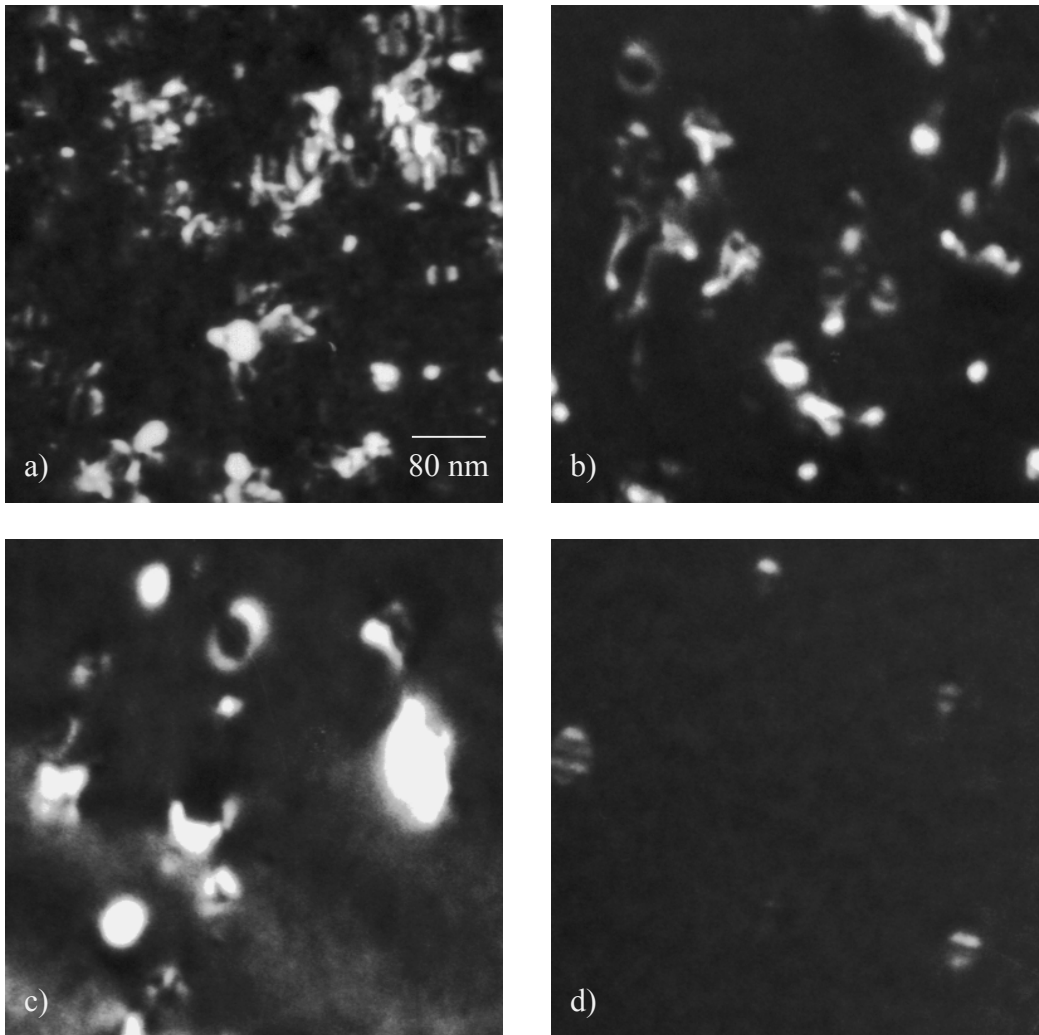


Figure 3-13 Series of plan view images showing the evolution of defects in material laser annealed at 770 mJ/cm^2 and then subsequently thermally annealed at $900 \text{ }^\circ\text{C}$ for times of a) 0 s, b) 6 s, c) 5 m, and d) 100 minutes. For this material set the epitaxial defects are completely dissolved between 6 seconds and 5 minutes. (Implant conditions: $15 \text{ keV Si}^+ 1 \times 10^{15}/\text{cm}^2$, $1 \text{ keV B}^+ 1 \times 10^{14}/\text{cm}^2$)

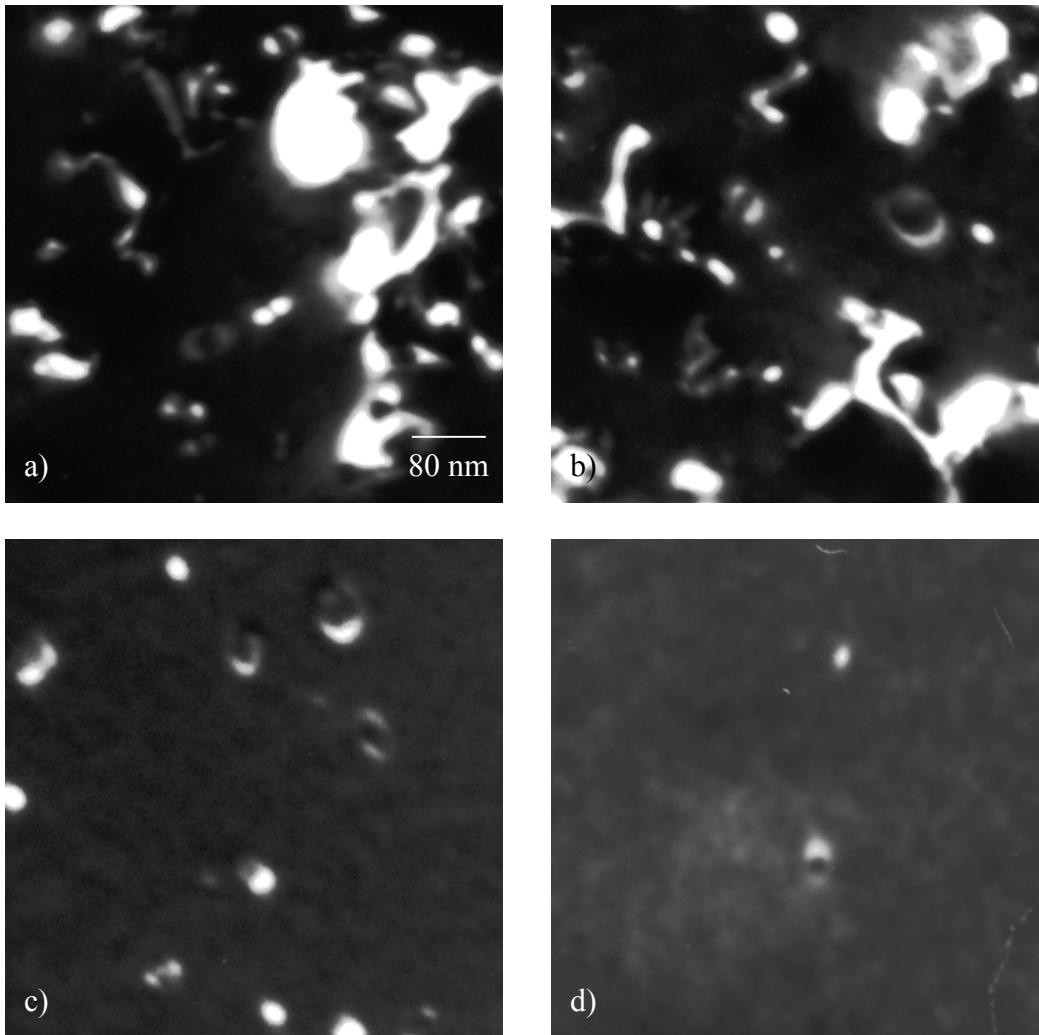


Figure 3-14 Images comparing the annealing behavior for samples within the process window. Material was laser annealed at a) 750, b) 770, c) 800, and d) 825 mJ/cm^2 and then thermally annealed at $750\text{ }^\circ\text{C}$ for 2 hours. The area inside loops increased as the energy density used during laser annealing increased. Upon surpassing the process window at $800\text{ mJ}/\text{cm}^2$, however, the area inside loops drops dramatically. (Implant conditions: $15\text{ keV Si}^+ 1 \times 10^{15}/\text{cm}^2$, $1\text{ keV B}^+ 1 \times 10^{14}/\text{cm}^2$)

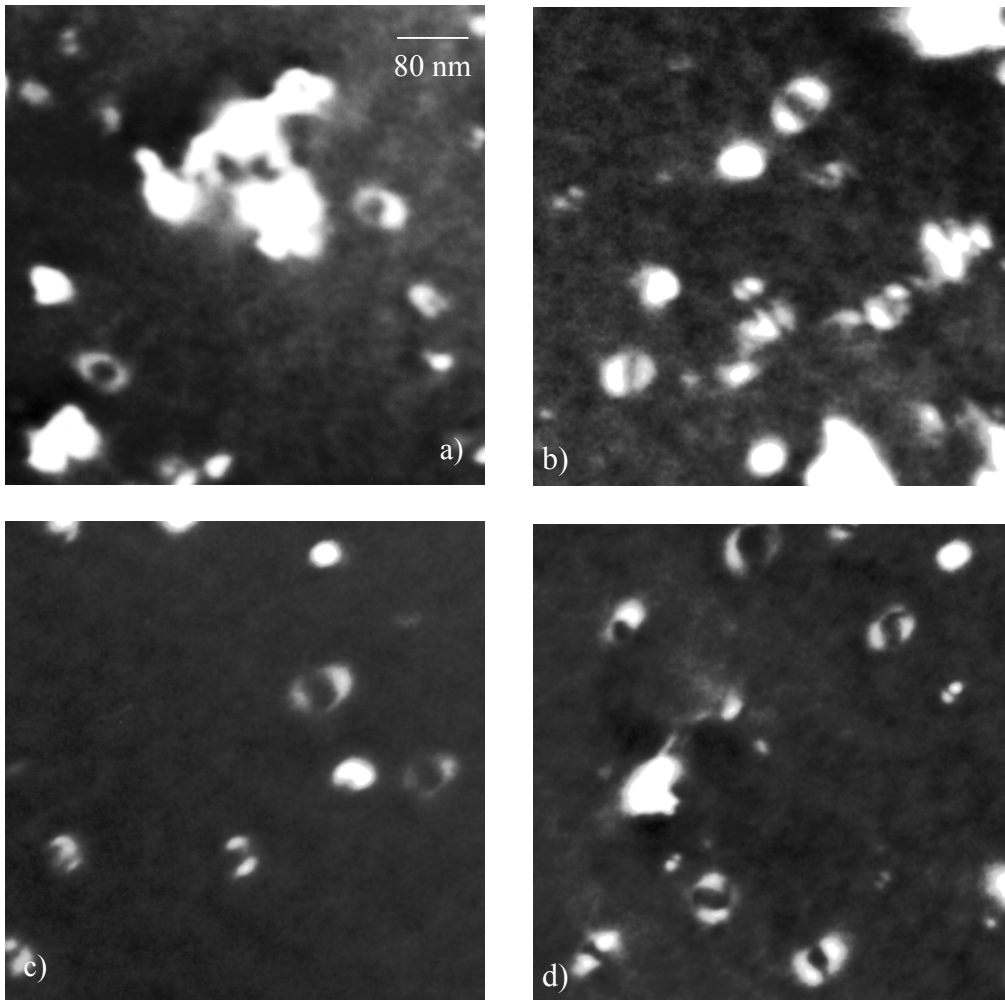


Figure 3-15 Images showing material laser annealed at 750 mJ/cm^2 and then subsequently thermally annealed at $750 \text{ }^\circ\text{C}$ for a) 4 and b) 8 hours. In comparison there is a smaller area bound by dislocation loops than material receiving a 770 mJ/cm^2 laser annealed and then thermal annealed at $750 \text{ }^\circ\text{C}$ for c) 4 and d) 8 hours. (Implant conditions: $15 \text{ keV Si}^+ 1 \times 10^{15}/\text{cm}^2$, $1 \text{ keV B}^+ 1 \times 10^{14}/\text{cm}^2$)

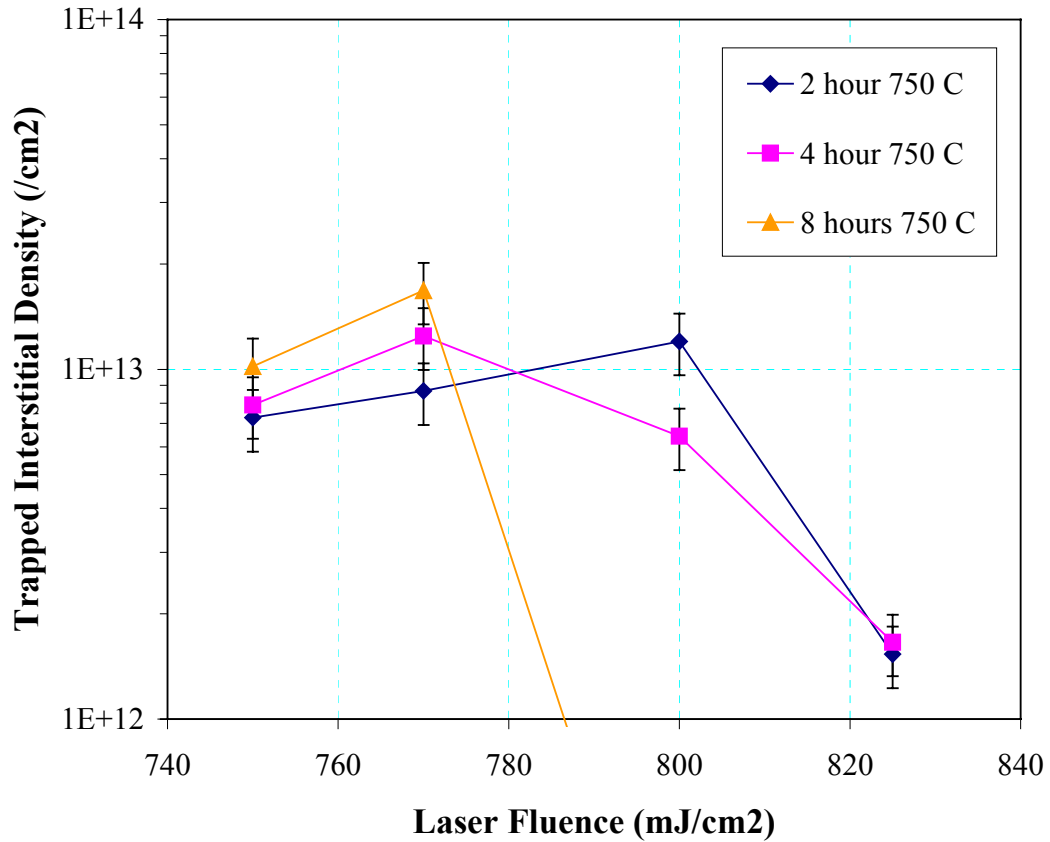


Figure 3-16 Trapped interstitials in dislocation loops as a function of laser energy density at an anneal temperature of 750 °C. Data for anneals of 2, 4, and 8 hours is included. It is observed that for all materials (750, 770 and 800 mJ/cm²) there is a maximum trapped interstitial density of about 1x10¹³/cm². Furthermore, this maximum density is reached at different times for each material possibly indicating the effect of epitaxial defects. (Implant conditions: 15 keV Si⁺ 1x10¹⁵/cm², 1 keV B⁺ 1x10¹⁴/cm²)

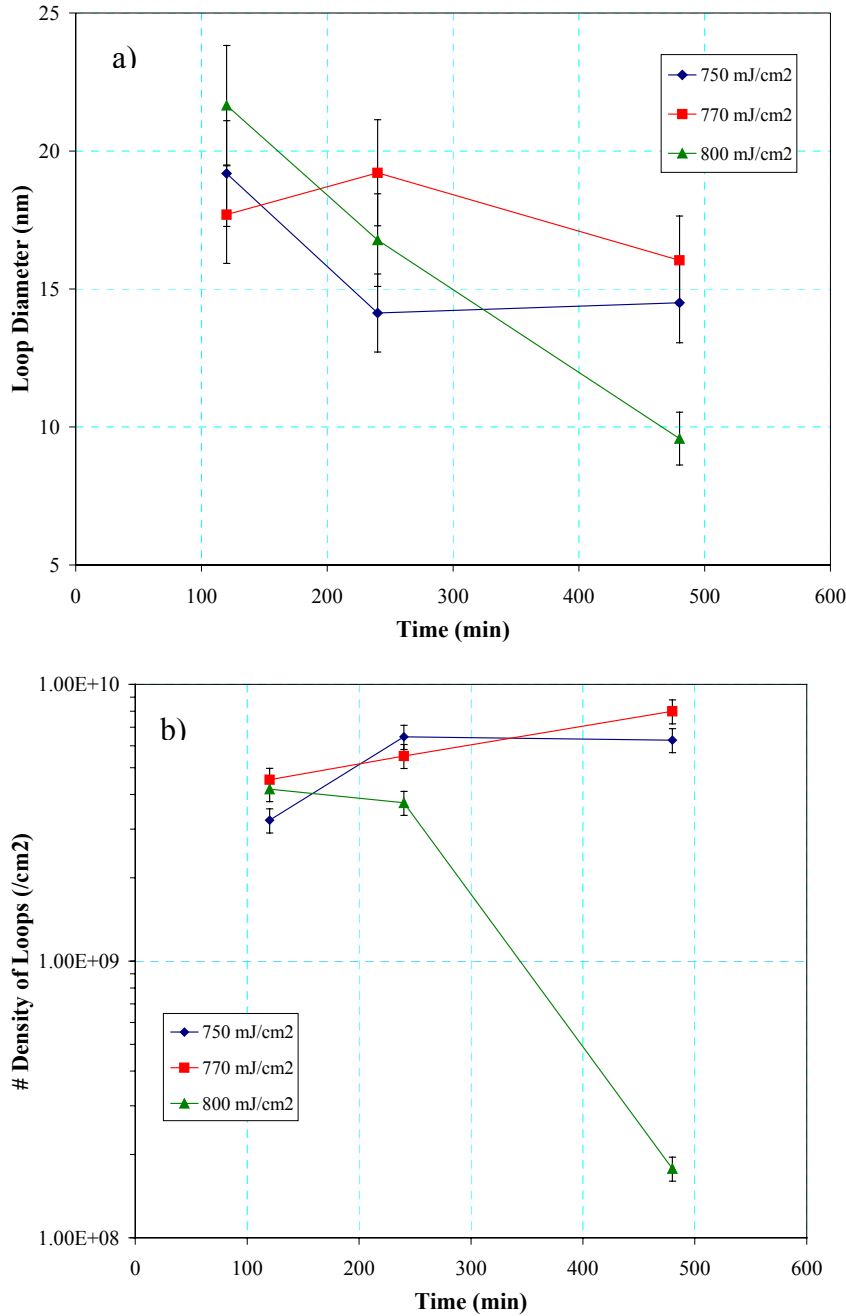


Figure 3-17 Plots showing both the a) average loop size and b) number density of loops as a function of time for each material in the process window. It is observed that there is actually an increase in the number density of loops along with a small decrease in their average size for both the 750 and 770 mJ/cm² materials, a trend that is opposite of standard coarsening behavior. For the high laser power material, there is a steady decrease in both number density and average loops size. (Implant conditions: 15 keV Si⁺ 1x10¹⁵/cm², 1 keV B⁺ 1x10¹⁴/cm²)

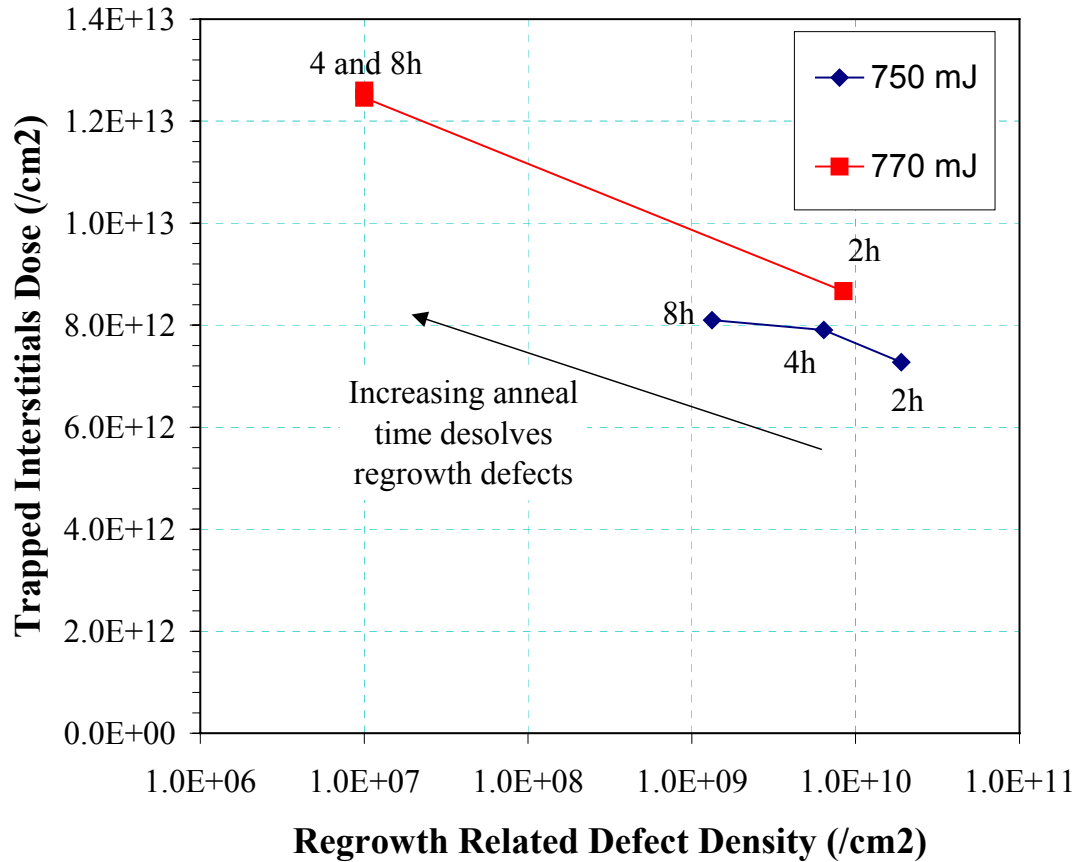


Figure 3-18 Plot showing the trapped interstitial density in dislocation loops as a function of the epitaxial defect density for laser annealed material (750 and 770 mJ/cm²) at an annealing temperature of 750 °C. Anneal time increases from the right side of the plot to the left and data is included for 2, 4, and 8 hours anneals. There is a general trend of increasing trapped interstitial population with decreasing epitaxial defect density suggesting that the dissolution of the regrowth related defects is releasing trapped interstitials. (Implant conditions: 15 keV Si⁺ 1x10¹⁵/cm², 1 keV B⁺ 1x10¹⁴/cm²)

CHAPTER 4 DIFFUSION AND ACTIVATION STUDIES

During conventional silicon processing there are a number of thermal cycles that the silicon is exposed to in order to activate dopants, form silicides, and deposit insulators. It is crucial that we understand how laser thermal process (LTP) formed shallow junctions behave when subjected to these thermal cycles. It is also important that we understand how variations in the laser energy density can affect the annealing behavior of these junctions. An experimental outline including steps used to process the material will be presented. Characterization of the material will be performed using secondary ion mass spectroscopy (SIMS), four-point probe (4PP), spreading resistance profiling (SRP), and Hall effect measurement. The focus of the chapter will be on the diffusion, and deactivation behavior of laser annealed material.

Characterization

This chapter uses four different tools for characterization of material. It is important to understand the limitations and the kind of data that can be provided by each of the tools. Following is a brief summary of secondary ion mass spectrometry, spreading resistance profiling, four-point probe, and Hall effect measurement.

Secondary Ion Mass Spectrometry (SIMS)

Secondary ion mass spectrometry combines physical sputtering with mass spectrometry to create a chemical characterization technique. By using a constant sputtering and dynamic ion counting followed by depth profiling, chemical dopant concentration as a function of depth can be determined. In the silicon semiconductor

industry this technique is most often used to determine the dopant profiles for both as-implanted and annealed materials. It must be noted that while SIMS can give an accurate measurement of metallurgical junction depth, it says nothing regarding the electrical junction depth or the activation of dopant in the silicon. Care must also be taken when considering the results from SIMS as it relies heavily on the use of reference standards for determining dopant concentrations. Ion mixing as well as crater measurement errors can also lead to errors. The most significant source of error comes during the initial stages of depth profiling before a steady state sputtering condition is obtained. In prior years this error was typically insignificant, but as junctions become shallower, this source of error dominates. For this work, dynamic SIMS was used to analyze the concentration-depth profiles of boron and antimony doped junctions both following laser processing and following thermal annealing.

Spreading Resistance Profiling (SRP)

Similar to SIMS, SRP allows for the characterization of a dopant depth profile. However, unlike the SIMS, SRP allows the determination of the active dopant concentration as a function of depth as well as the electrical junction depth. This is achieved by first creating a shallow bevel, typically on the order of thousandths of a degree, that extends from the surface of the silicon down towards the bulk. An electrical probe is then stepped along the bevel as the resistivity is measured. By assuming a mobility of carriers in the region, the active concentration is extracted as a function of depth. It is this assumption that can lead to errors in SRP, especially for materials such as laser processed silicon that have a high density of extended and point defects within the current path and in the vicinity of the p-n depletion region. In this work, SRP was used to determine if certain clustered peaks observed in SIMS were electrically active.

Four Point Probe (4PP)

Four point probing is a fast and non-destructive characterization process that applies a voltage potential to the surface of the sample using two electrical contacts. The voltage induces a current that is measured by another set of contacts. The result, by Ohm's Law, is a resistance that can be in turn be correlated to a sheet resistance by using sample size correction factors. It is important to note that while 4PP gives a sheet resistance, it does not indicate the depth of the junction, the active concentration of dopant, or the mobility of the carriers in the material.

Hall Effect Measurement

In 1879 Edwin H. Hall found that if a thin gold plate is placed in a magnetic field, which is at right angles to its surface, an electric current flowing along the plate can cause a potential drop at right angles both to the current and the magnetic field. Termed the Hall effect, this takes place because electrically charged particles (in this case electrons) moving in a magnetic field are influenced by a Lorentz force and deflected laterally. In order to determine both the mobility and the active dose, both resistivity measurements, similar to 4PP, and Hall measurements are needed. The van der Pauw technique is widely used in the semiconductor industry to determine the resistivity of uniform samples [Van58] and is used in this work. The Hall effect can also be used to determine the carrier type (electrons or holes). The primary drawback to Hall effect rests in the difficulty of forming ohmic contacts on high resistivity samples such as those with very low dopant concentrations. It is also highly sensitive to electrical defects.

Experimental Outline

One set of silicon wafers (<100> n-type and p-type Czochralski 10-20 ohm-cm) received a preamorphizing 15 keV Si⁺ implant to a dose of 1×10^{15} cm⁻² to create a 32 nm

continuous amorphous layer, as determined via both VASE and XTEM, in Chapter 3. Select wafers were then doped with either a 1 keV B⁺ or a 5 keV Sb⁺ implant to a dose of $1 \times 10^{14} \text{ cm}^{-2}$. So that electrical characterization of the junctions could be performed, samples implanted with B⁺ used n-type silicon and those receiving Sb⁺ used p-type silicon. Background dopant concentrations were less than 10^{16} cm^{-3} . All implants were performed on unmasked silicon that received a 10:1 buffered oxide etch prior to implantation. No tilt or twist was used during ion implantation. Some wafers received a thermal anneal prior to laser annealing in order to remove implant damage or to smooth the amorphous-crystalline interface. The wafers were then laser annealed using a 308 nm ultraviolet (UV) XeCl excimer laser. Energy densities used varied from 730 to 850 mJ/cm^2 , with pulse durations of approximately 20 nanoseconds. The spot size of the laser was $5 \times 5 \text{ mm}^2$.

Thermal annealing was performed in either a conventional tube furnace or in a rapid thermal annealing (RTA) system. The tube furnace consisted of a 3 inch diameter quartz tube inside a Lindberg furnace. A flowing high purity N₂ ambient was supplied and exhaust gas was run through a liquid bubbler to prevent back flow of gas into the furnace. The system was N₂ purged for 5 minutes prior to beginning the annealing process. The temperature was regularly calibrated using an Omega chromal-alumel type K thermocouple. Samples were placed into a quartz boat and inserted approximately 5 cm into the furnace for 3 minutes before being pushed into the hot zone of the furnace. Thermocouple measurements indicate this area was generally 400 °C for a hot zone furnace temperature of 750 °C. The purpose of this was to drive off excess adsorbed

water vapor on the sample and boat as well as to allow the assembly to heat up to temperature faster.

Rapid thermal anneals were performed in an AG Associates lamp based RTP system. A flowing high purity N₂ ambient and pre-anneal purge time of one minute was used. For all anneals in this system, a pre-soak anneal of one minute at 250 °C less than the peak temperature was used just before the ramp to peak temperature. The purpose of this pre-soak is to drive off excess water vapor, increase the ramp rate during the ramp to the peak temperature, and minimize over- and under-shoot of the peak temperature.

Secondary ion mass spectroscopy was performed at the University of Central Florida's Advanced Materials Processing and Analysis Center (AMPAC). The tool used was an Adept 1010 quadropole system developed by Physical Electronics. For boron doped samples, a 2 keV, 40-50 nA oxygen beam was used for sputtering. For antimony doped material, a 3 keV, 20 nA cesium beam was used. The incident beam angle was 41° for both sample types. Crater measurement was performed with a Dektak3 profilometer. Measured profile dose was calculated using reference samples. Spreading resistance profiling was performed at Solecon Laboratories. A bevel angle of 0.00206 was used with a probe step increment of 2 microns. Hall effect measurements were performed using tungsten probes contacted to indium corner contacts. The forced current was typically at 10 μA, with a magnetic field of 3 kG. Measurements were performed at room temperature.

Diffusion Studies of LTP Silicon

This next section examines the effect thermal annealing has on the diffusion of dopant in laser thermal processed silicon. It will begin by defining the process window,

this time using SIMS, and will be followed by diffusion studies of boron and antimony. The effect of laser energy density within the process window on this behavior will also be studied. Material laser annealed at energy densities beyond the process window will be considered in a later section.

Retained Dose Calibration

It was found that for all processing conditions the measured retained dose fluctuated between 1.06×10^{14} and $2.84 \times 10^{14}/\text{cm}^2$, which is up to ~ 3 x greater than the implant dose measured by the implant tool. Given the fact that the ion implantation steps were performed at industrial facilities at Motorola and the difficulty in SIMS for measuring low concentration profiles, it is believed that this deviation is due to SIMS ion count error rather than error during the implantation step. With regards to laser annealing parameters, no correlation was found to exist between the laser energy density used and the measured retained dose suggesting that any dose loss due to the laser annealing step was uniform or below the SIM detection limit. It was found that samples that received post-LTP thermal anneals showed a higher retained dose than as-laser annealed material. Given the broader dopant profiles of the thermally annealed material and the highly unlikely case of spontaneous generation of dopant, this suggests that the majority of the SIMS error was within the surface region. This is a well-known SIMS error and is attributed to the non-steady state conditions that exist when sputtering begins. So that an effective comparison could be made between profiles, all SIMS profiles within this work have been normalized to a $1.0 \times 10^{14}/\text{cm}^2$ dose and assume that any dopant loss is uniform between samples and independent of processing conditions.

Defining the Process Window

In the previous chapter plan view transmission electron microscopy was used to define the process window, which was found to start at 750 mJ/cm^2 and end near 800 mJ/cm^2 . Another method of characterizing the process window is using SIMS. By matching up the profiles and determining the depth for a particular dopant concentration, it can be determined for what range of powers a similar junction depth is created. Figure 4-1 shows the boron SIMS profiles of samples laser annealed between 730 and 900 mJ/cm^2 . There was no subsequent thermal anneal. It is observed that at a concentration of $1 \times 10^{18}/\text{cm}^3$, there is a constant junction depth of approximately 38 nm for laser energy densities of 800 mJ/cm^2 and below. The concentration of $1 \times 10^{18}/\text{cm}^3$ was selected since the noise increases dramatically for concentrations below this making an accurate determination of the junction depth difficult. This finding supports the findings in Chapter 3 that suggest that 800 mJ/cm^2 marks the end of the process window. Determining the start of the process window using SIMS can be difficult and is unclear in this figure. For laser energy densities below the process window, it would be expected that junction depths would be shallower indicating a shallower melt depth. At a concentration of $1 \times 10^{18}/\text{cm}^3$, this is not observed. However, if the SIMS profiles are examined above $1 \times 10^{19}/\text{cm}^3$, a more significant “snow plow” effect, or non-uniform segregation, of the boron is observed for the 730 mJ/cm^2 material, than for those between 750 and 800 mJ/cm^2 . This observation is not explainable by the literature that claims that as the energy density drops and the epitaxial velocity increases, there should be a greater incorporation of boron into the solid. Nonetheless, it is measurably different in 730 versus 750 mJ/cm^2 material. While this in itself does not determine whether the 730 mJ/cm^2 material is in the process window, when supported with the polycrystalline

diffraction patterns observed in Chapter 3, it can be stated with confidence that this material is below the process window. For the rest of this chapter we will consider the process window to be between 750 and 800 mJ/cm² based off of SIMS results in this chapter and TEM work in the previous chapter.

Diffusion of Boron

In the previous chapter it was observed that there was still enough of a supersaturation of interstitials present in the end of range after the laser anneal to form dislocation loops during subsequent thermal annealing. It is therefore expected that we should see evidence of interstitial mediated transient enhanced diffusion of boron. Figure 4-2 compares the effect of a thermal anneal on conventional material versus laser processed material. While the initial profiles are dramatically different, after a 750 °C 2 hour anneal, they appear very similar, especially in the tail diffusion area. Also present in both is a peak centered near the original amorphous-crystalline interface. This peak is slightly deeper for the conventionally processed material. Figure 4-3 shows the SIMS profiles of material laser annealed between 750 and 800 mJ/cm² and then thermally annealed at 750 °C for 2 hours. Included is one of the original as-LTP profiles for reference. The first significant observation is that there is significant enhanced boron tail diffusion for all laser anneal energy densities. Using literature values for boron diffusion [May90], we find that the standard boron diffusivity for this anneal would be less than 2 nm. It is also observed that there is an increase in diffusion as the laser energy density is increased within the process window. The increase in boron tail diffusion is supported via a boron concentration drop in the near surface region (about 10 nm). Coincident with this surface diffusion is the formation of immobile boron peaks located at 30 nm, or the original amorphous crystalline interface. In conventional processing these peaks are

typically associated with boron-interstitial clusters that are known to be both inactive and immobile. It is also possible that these peaks are due to boron getting to defects, either dislocations running to the surface or about dislocation loops that form at the end of range. However, TEM analysis of material laser annealed at 800 mJ/cm^2 and thermal annealed at $750 \text{ }^\circ\text{C}$ for 2 hours shows only the presence of end of range dislocations. Therefore, for this processing condition, the peak can only be attributed to either boron interstitial clustering or getting to end of range dislocation loops, both commonly observed phenomena. Further experimentation is required to determine this.

It is known that these boron clusters dissolve at a measurable rate at temperatures greater than $850 \text{ }^\circ\text{C}$. Figure 4-4 shows that thermal annealing of the material at $900 \text{ }^\circ\text{C}$ for 100 minutes leads to the dissolution of these peaks for 770 and 800 mJ/cm^2 laser energy densities, thus suggesting that dopant clustering is a possibility. However, comparison with TEM, Figure 4-5, shows that this anneal also results in the dissolution of a majority of extended defects for material laser annealed at 770 mJ/cm^2 and all of the defects laser annealed at 800 mJ/cm^2 . If the anneal time is decreased to 5 minutes for a $900 \text{ }^\circ\text{C}$ anneal, it is found that for the 770 mJ/cm^2 laser annealed material, we see little evidence of a peak in SIMS, Figure 4-6, yet a large number of dislocation loops remain as observed in TEM, Figure 4-7. No peak or dislocation loops are observed for the 800 mJ/cm^2 material. This gives strong support to the suggestion that the observed peaks are indeed due to boron interstitial clustering. Given the possibility that interstitial behavior might be affected by the evolution of the epitaxial defects, as was suggested from findings in Chapter 3 regarding dislocation loops evolution, material was isothermally annealed at $750 \text{ }^\circ\text{C}$ between times of 15 minutes and 8 hours as seen in Figure 4-8. One

observation is that even at the longest anneal time of 8 hours, the material laser processed at 770 mJ/cm^2 never diffuses as deep as the 800 mJ/cm^2 material. It is also observed that while diffusion is over within 15 minutes for the 800 mJ/cm^2 material, the enhancement for the 770 mJ/cm^2 material is still significant between 2 and 4 hours of annealing and only ends sometime between 4 and 8 hours. This result will be discussed more in Chapter 5, but it is interesting to note that complete dissolution of the epitaxial defects also occurs between 2 and 4 hours.

Diffusion of Antimony

Antimony has an opposite enhanced diffusion behavior relative to boron. Rather than being enhanced by a supersaturation of interstitials, antimony is enhanced via a vacancy supersaturation. Therefore, doping the material with antimony and performing the above experiments can give understanding of the vacancy saturation levels. Figure 4-9 shows the initial antimony SIMS profiles as well as those that have received a $750 \text{ }^\circ\text{C}$ 2 hour anneal. The initial antimony profiles have the same junction depth as the boron doped material, indicating that the dopant did not affect the process window. After the thermal anneal, the antimony profiles appear unchanged. This suggests that there was little to no flux of vacancies. Unfortunately, the precision of the SIMS tool was unable to determine if there was actually a retarded antimony diffusion that would be expected due to an interstitial supersaturation.

Activation Studies of LTP Silicon

In the previous section SIMS was used to analyze the diffusion behavior of boron and antimony during post-LTP thermal processing. While SIMS can give insight as to the retained dopant dose and an estimate of the junction depth, electrical characterization is required to determine the electrical junction depth as well as the degree of deactivation.

In this section three electrical characterization techniques are employed to analyze the change in electrical behavior of laser processed samples.

Four Point Probe

Every doped sample that was used in these studies received sheet resistance measurements prior any further characterization. Since 4PP offers a quick and inexpensive electrical characterization, it was determined that by probing prior to more time consuming or expensive characterization sample error due to mechanical error in the laser or human error could be avoided. Figure 4-10 shows the sheet resistance of boron doped material laser annealed between 730 and 900 mJ/cm². It is observed that there is a significant drop in sheet resistance, 8250 to 4120 ohms/sq, as the laser energy density is increased from 730 to 750 mJ/cm². Due to previous investigations of the activation of boron by Murto et al. [Mur00], as well as finding in Chapter 3, it is believed that this is due to the transformation of the film from polycrystalline to single crystal and a resulting increase in the hole mobility. As the energy density is increased, the sheet resistance continues to decrease, but at a much slower rate. From energy densities of 750 to 800 mJ/cm² it is known from SIMS that the junction depth is constant, but there is a reduction in the number of epitaxial defects, thus possibly increasing the carrier mobility. Once the end of the process window is reached, continuous increase in laser energy density results in little change in the sheet resistance. While the junction depth is increasing the increase in mobility associated with a decrease in carrier concentration is relatively small. At laser energy densities of 900 mJ/cm², the sheet resistance was observed to fluctuate greatly. While some material showed sheet resistances similar to those as similar energy densities, some material would show significantly greater sheet resistances. While further characterization was not performed on these anomalous samples, it is believed

that this was a result of inconsistencies in the laser power or possibly ablation of the surface and loss of dopant. A similar test was performed on samples doped with antimony, and therefore n-type, and a similar trend was observed, Figure 4-11.

Upon thermal annealing at 750 °C of the boron doped laser processed material there is an increase in sheet resistance for material laser annealed at the end of the process window, 800 mJ/cm², that is not observed for any other laser energy density, Figure 4-12. For the other two energy densities in the process window there is a drop in sheet resistance after 20 seconds of annealing at 750 °C, followed by an increase in sheet resistance for all laser energy densities after 2 hours of annealing. This sheet resistance evolution as a function of laser energy density is more clearly observed in Figure 4-13. Here it is observed that for times between 10 seconds and 2 hours, the sheet resistance of the 800 mJ/cm² material is actually higher than in the lower energy density material. Similar anneals on antimony doped material, Figure 4-14 showed a decrease in sheet resistance that was independent of the laser energy density for the observed annealing times of 20 seconds and 2 hours.

It must be noted that occasionally there was some difficulty in establishing a good ohmic contact for samples that were as-LTP. If forward and reverse currents were not within 10%, the sample was cleaned and the orientation with respect to the probe tips would be changed until the currents were within 10%. If after five attempts an ohmic contact could not be achieved, that sample was eliminated. This difficulty in achieving ohmic contact to the material was observed not only during 4PP measurements but also during SRP and Hall measurements, discussed next. It must also be noted that this phenomenon was never observed for samples that received a thermal anneal. It has also

not been observed as a problem for lower resistivity material as shown by a number of authors.

Spreading Resistance Profiling

During SIMS analysis of post-LTP thermally annealed material a boron peak was observed around 30 nm. While other characterization methods might allow estimated guesses regarding the electrical behavior of this peak, SRP is the only method used that allows direct measurement of the activation within this region. It was previously determined via TEM and annealed SIMS profiles that this region was not a result of boron gettering by extended defects and that boron-interstitial clustering was the likely phenomenon responsible for this peak. Two samples were sent for SRP, both having received laser anneals at 800 mJ/cm^2 . One sample was left as-LTP while the other was thermally annealed at $750 \text{ }^\circ\text{C}$ for 2 hours. It was observed that when the standard mobility for holes in silicon was assumed, the integrated dopant dose and profile was dramatically low, 1×10^{12} rather than $1 \times 10^{14}/\text{cm}^2$ for the non-thermally annealed material. If the profile is normalized to the SIMS dose the profiles more evenly match and the electrical junction depth is precisely at 30 nm, the depth of the original amorphous-crystalline interface. Figure 4-15 shows the results of the SRP as well as those from SIMS of the same material. Very similar profiles are observed between the SIMS and SRP of the thermally annealed material, with the exception of peaks at the surface and 30 nm for the SIMS. This indicates that either these regions are not electrically active or the SRP was not sensitive enough to detect these regions. If the annealed profile is integrated to determine a total active dose, a value of $1.3 \times 10^{13}/\text{cm}^2$. This value will be compared to Hall measurement results in the next section.

Hall Effect Measurement

So that a correction factor for the Hall sample sizes used in this work, $4 \times 4 \text{ mm}^2$, could be determined, as-LTP material was measured at room temperature. It was assumed that observed values would be uniform and independent of laser energy density. However, it was found that consistent measurements at room temperature were not possible, as shown in Figure 4-16. This phenomenon is very similar to that observed for non-thermally annealed samples used in four point probe sheet resistance measurements. In addition, often the majority carrier was determined to be electrons rather than holes for p-type material. The opposite was observed for n-type material. Figure 4-16 neglects measurements that indicated the opposite carrier type. In similar solid phase epitaxy work, Lindfors suggested that the end of range damage caused by the amorphizing implant generated sufficient leakage currents that the underlying substrate layer was being measured rather than the doped region and that this source of leakage could be eliminated by cooling the material below $250 \text{ }^\circ\text{C}$ [Lin03]. This was found to be somewhat true for LTP material and upon cooling to below this temperature; a consistent measurement of hole carriers was observed. During these measurements, the measured active dose varied between 8.5×10^{13} and $1.0 \times 10^{14} / \text{cm}^2$ with an error of as much as 20%, though was no longer dependent on the laser energy density, Figure 4-17. Due to the difficulties in obtaining accurate Hall measurements on non-thermally annealed material, non-laser annealed samples were furnace annealed at $1000 \text{ }^\circ\text{C}$ for 10 minutes. The purpose of this anneal was to intentionally remove all damage created by both the implantation and to activate the entire implanted dose. Hall measurement of the active dose for this material was found to be about $1.3 \times 10^{14} / \text{cm}^2$ with a measurement error of

less than 10%, also shown in Figure 4-17. It is unknown whether there was any significant dopant loss during this high temperature anneal. Given that this result is similar to those that were not annealed but cooled below 250 °C, no form factor was used.

Similar to material that was measured with the four point probe, it was observed that any sample that received a thermal anneal of 750 °C or greater did not show a large measurement error or incorrect carrier type. Figure 4-18 shows the effects of a 750 °C 2 hour anneal on the active dose of boron. It is observed that there is a dramatic decrease in the active dose of boron for the 800 mJ/cm² material relative to material that received laser anneals at other energy densities. This dose of $1.8 \times 10^{13}/\text{cm}^2$ is very similar to the $1.3 \times 10^{13}/\text{cm}^2$ observed in SRP. Not only does this possibly indicate that the Hall size correction factor of x1 is valid, but it also indicates that an accurate estimation of the active concentration of boron can be determined by truncating the SIMS profile at the base of the near surface concentration depression. Repeating this SIMS truncation process with the 750 and 770 mJ/cm² material gives a SIMS estimated active dose of 5.0×10^{13} and $3.2 \times 10^{13}/\text{cm}^2$, respectively. These values are similar to those measured via Hall of 3.5×10^{13} and $3.8 \times 10^{13}/\text{cm}^2$. By comparison, analysis of the antimony doped material shows little deactivation during the 120 minute anneal at 750 °C, Figure 4-19. If the boron doped material is subjected to a 900 °C thermal anneal, Figure 4-20, it is observed that there is a deactivation of boron between 0 and 5 minutes. The magnitude of the deactivation is similar to that observed for the 5 minute anneal at 750 °C and a similar dependence on the laser energy density is observed. However, upon further annealing for 100 minutes, the deactivation process is reversed and nearly the entire implanted dose becomes active. Also, the dependence on the energy density is decreased.

Again, if the primary method of deactivation at these boron concentrations is via the formation of BICs, this would correspond to the dissolution of those defects.

Summary

This chapter investigated the diffusion and the deactivation of laser thermal processed material during thermal annealing. For the implant conditions used, it was determined using SIMS that the process window was between 750 and 800 mJ/cm². This result supported the findings of Chapter 3. A high transient enhanced diffusion was observed during post thermal annealing of boron-doped samples indicating a flux of interstitials. The enhancement was similar in magnitude to that of conventionally processed material suggesting that the source of interstitials was primarily from the end of range damage created during the silicon pre-amorphization step. Material laser annealed at the end of the process window resulted in the same boron dopant profile as that of conventional material. No enhanced diffusion was observed for antimony doped material indicating there was little or no flux of vacancies. The amount of enhanced diffusion of boron was observed to be dependent on the energy density used during the laser annealing. It was also observed that the time to TED saturation was longer for material laser annealed in the middle of the process window when compared to material laser annealed at the end of the process window.

This chapter also analyzed the effects of thermal annealing on the electrical behavior of laser processed material. Using spreading resistance profiling, it was determined that boron concentration peaks observed in SIMS were inactive and most likely the result of boron-interstitial clustering. Analysis of material using four point probing showed that just following laser annealing there was a continual, though non-linear, decrease of sheet resistance as the laser energy density increased, for both boron

and antimony doped material. The most dramatic decrease in sheet resistance was observed as the minimum process window threshold was crossed. While there was a dependence of sheet resistance on the laser energy density during thermal processing for boron doped material, there was little to no dependence for antimony doped material. Further analysis using Hall effect measurements of the active dose confirmed that these differences were due to deactivation of the boron that was dependent on the laser energy density, while antimony doped material showed little or no deactivation. Once the post-LTP anneal temperature was raised to 900 °C, however, the dependence of deactivation on the laser energy density reduced, and dopant that was inactive after 5 minutes was reactivated after 100 minutes of annealing.

Thus using both chemical and electrical characterization methods, it was observed that two interstitial mitigated phenomena, transient enhanced diffusion and boron interstitial clustering, were both observed to be affected by the energy density used during the laser anneal of silicon. In those same experiments, antimony, a vacancy diffuser and low solubility impurity, was shown to be unaffected. In chapter 3, a possible correlation between the density of epitaxial defects and dislocation loop formation was made. This suggested it was not the laser energy density that affected the interstitials but rather the epitaxial defect density that resulted from variations in the laser energy density. Given that similar trends were observed in experiments in this chapter with regards to interstitial behavior, it is suggested that the same phenomenon is being observed, but further experimentation is required. Chapter 5 will explore and further discuss the result of this chapter as well as provide further evidence to support the theory of epitaxial defect retardation of interstitial based phenomena.

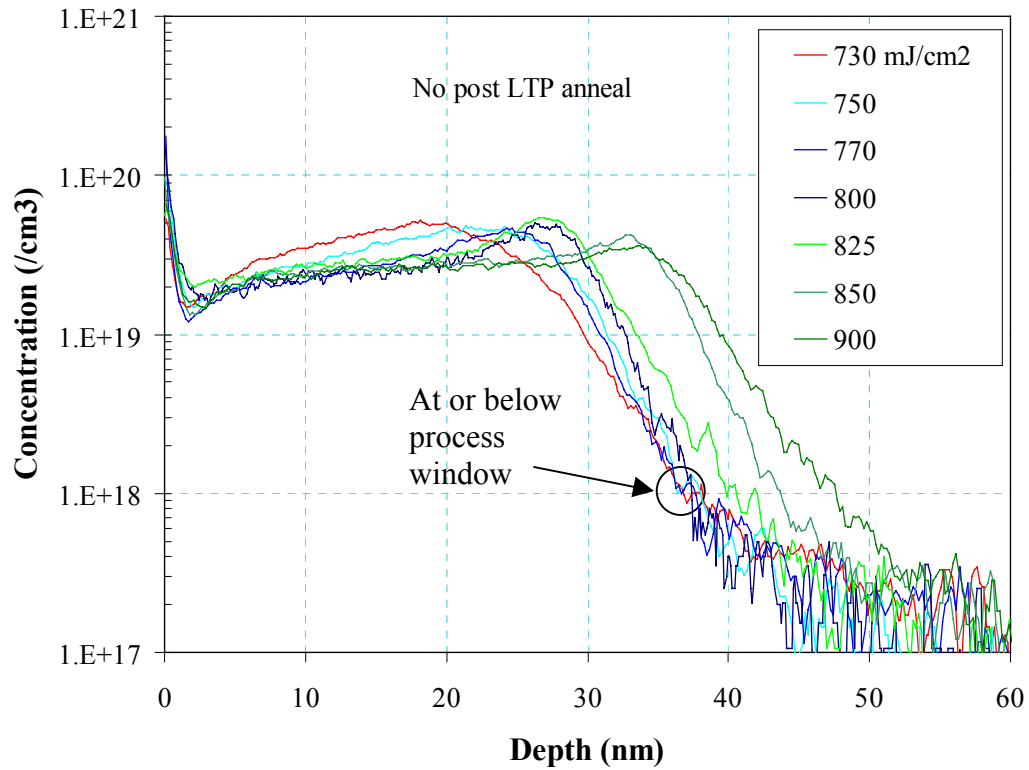


Figure 4-1 SIMS of boron doped laser processed material. Laser energy densities from 730 up to 900 mJ/cm^2 are shown. Materials determined to be in the process window are shown in varying shades of blue. Materials determined to be above the process window are shown in shades of green, while that one which is below is in red. (Implant conditions: 15 keV Si^+ $1 \times 10^{15}/\text{cm}^2$, 1 keV B^+ $1 \times 10^{14}/\text{cm}^2$)

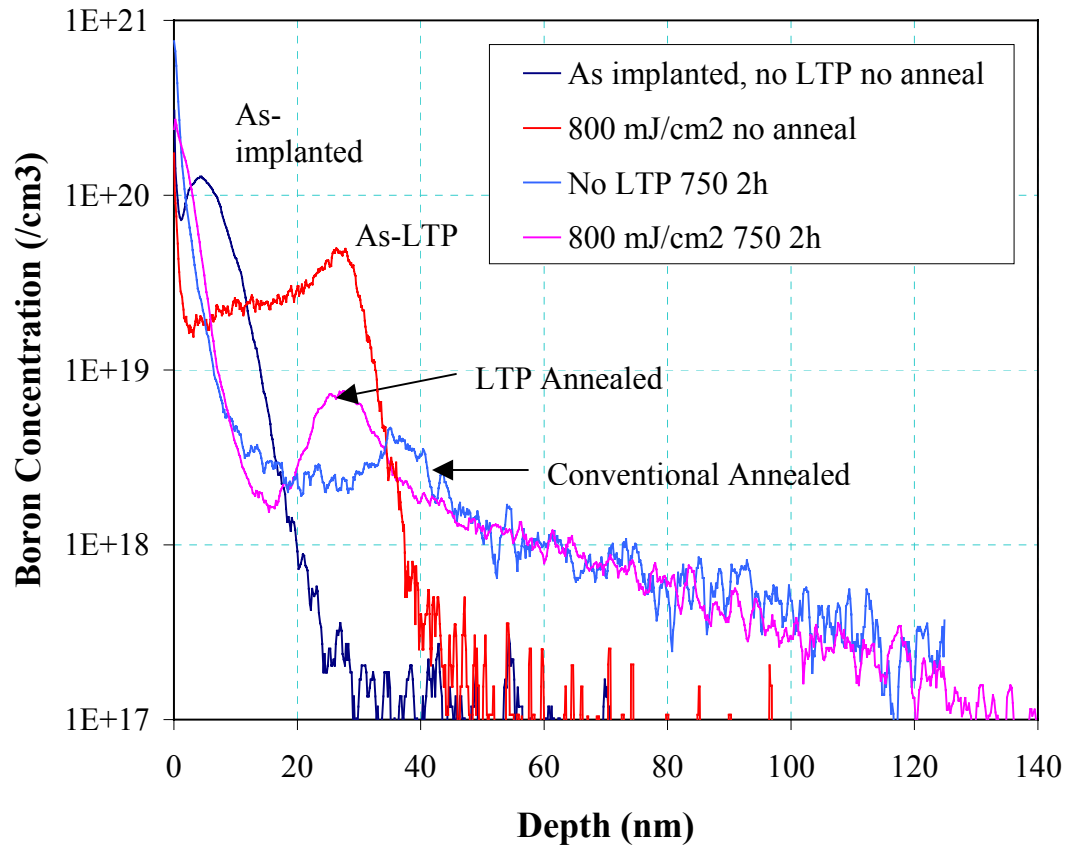


Figure 4-2 SIMS of boron comparing diffusion in conventionally processed material and that having first received a laser anneal at an energy density of 800 mJ/cm². While the initial profiles are different, the final diffused profiles are relatively similar. (Implant conditions: 15 keV Si⁺ 1x10¹⁵/cm², 1 keV B⁺ 1x10¹⁴/cm²)

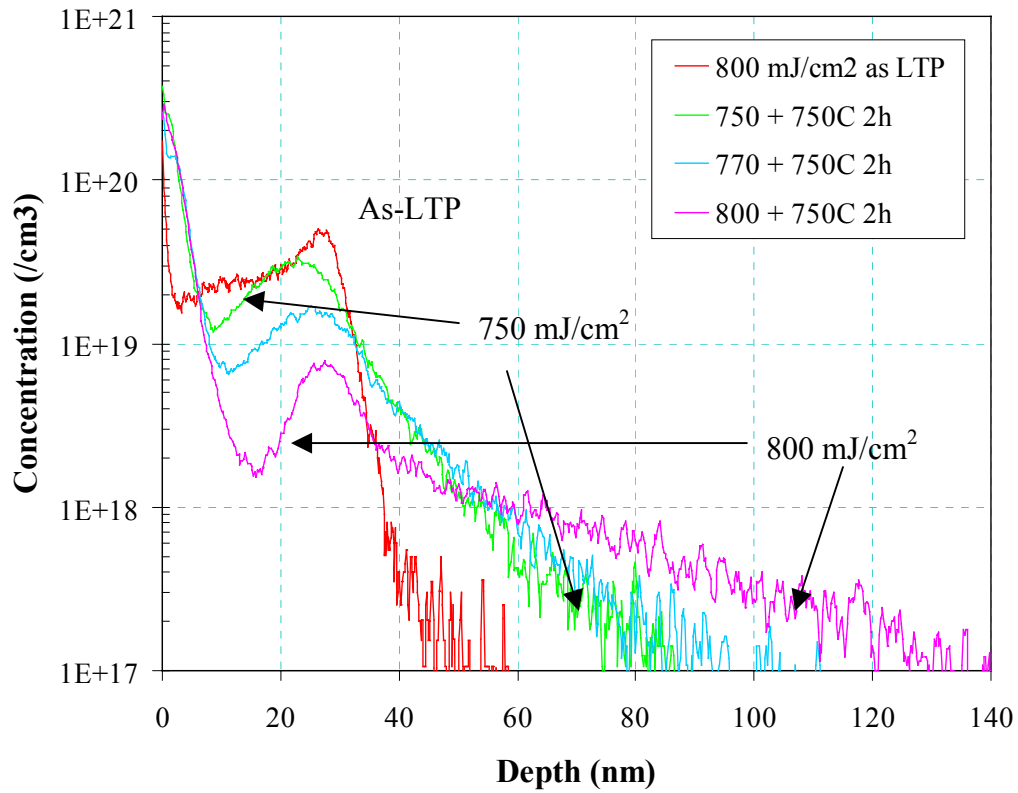


Figure 4-3 SIMS of boron doped laser processed material having received a 750 °C 2 h anneal. It is observed that diffusion increases as the laser energy density used during LTP increases from 750 to 800 mJ/cm^2 . A drop in concentration near the surface supports tail diffusion. The non-annealed profile for the 800 mJ/cm^2 material is shown for junction motion reference purposes. (Implant conditions: 15 keV Si^+ $1 \times 10^{15}/\text{cm}^2$, 1 keV B^+ $1 \times 10^{14}/\text{cm}^2$)

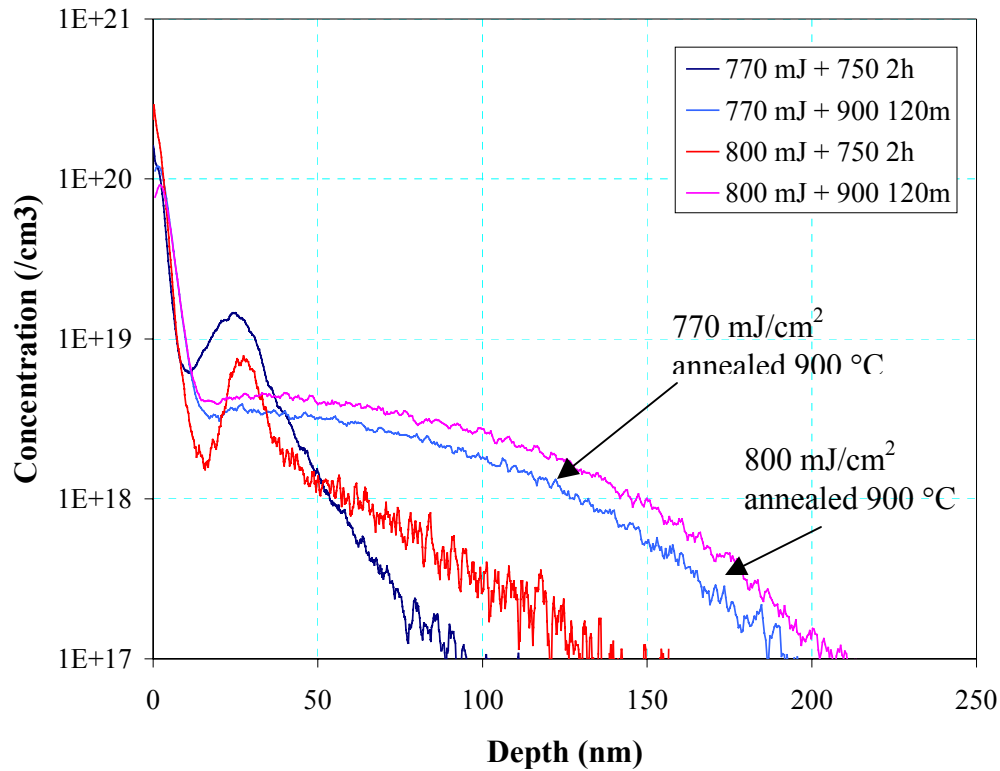


Figure 4-4 SIMS of boron doped laser processed material subsequently thermally annealed at 900 °C for 100m. It is observed that this anneal breaks up the peaks located near 30 nm. Again more diffusion is observed for the high laser energy density processed material. Materials receiving laser anneals of 770 and 800 mJ/cm² and annealed at 750 °C are also shown. (Implant conditions: 15 keV Si⁺ 1x10¹⁵/cm², 1 keV B⁺ 1x10¹⁴/cm²)

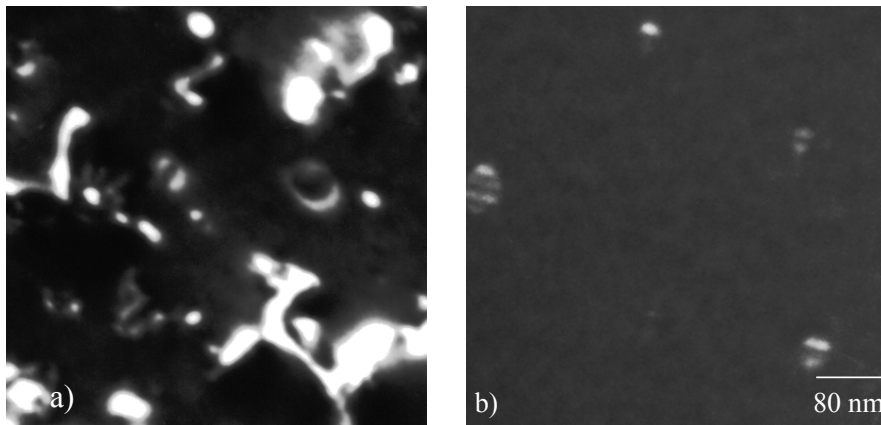


Figure 4-5 PTEM of material laser annealed at 770 mJ/cm² and then thermally annealed at 750 °C for 2h and 900 °C for 100m. It is observed that the higher anneal is enough to dissolve most of the defects. (Implant conditions: 15 keV Si⁺ 1x10¹⁵/cm², 1 keV B⁺ 1x10¹⁴/cm²)

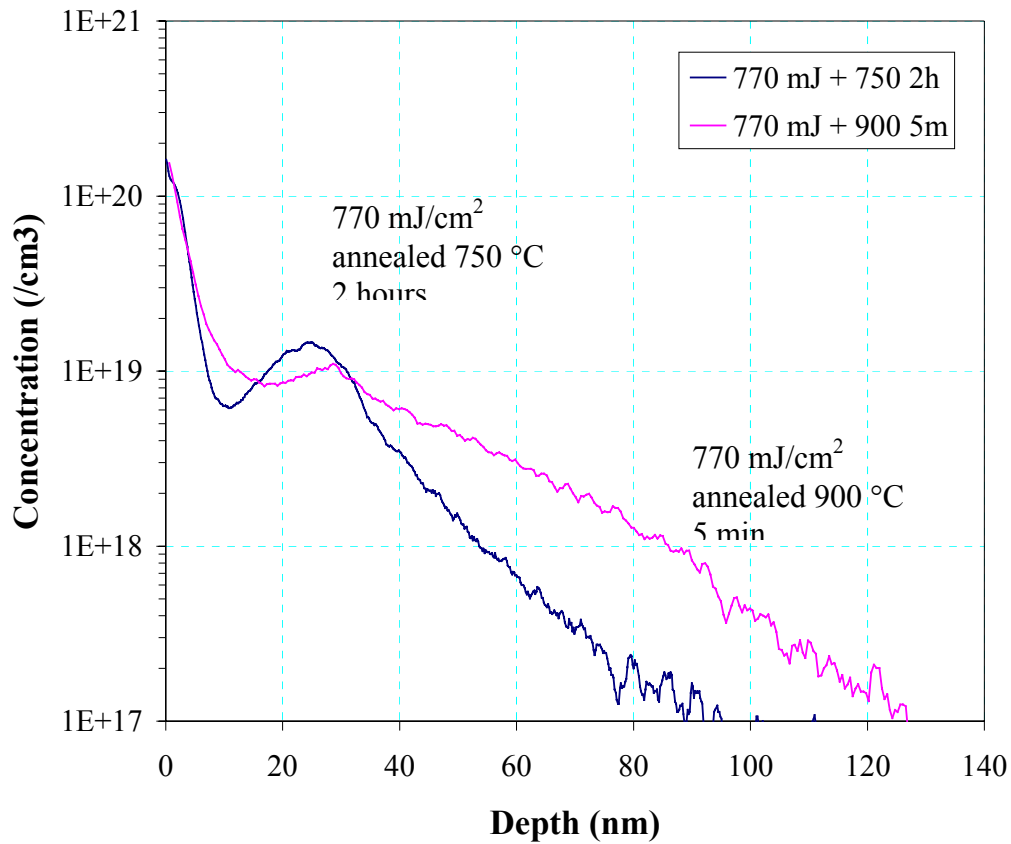


Figure 4-6 SIMS of boron doped laser processed material (770 mJ/cm^2) subsequently thermally annealed at $900 \text{ }^\circ\text{C}$ for 5 m. It is observed that this anneal breaks up the peaks located near 30 nm. The same material annealed at $750 \text{ }^\circ\text{C}$ for 2 h is also shown. (Implant conditions: $15 \text{ keV Si}^+ 1 \times 10^{15}/\text{cm}^2$, $1 \text{ keV B}^+ 1 \times 10^{14}/\text{cm}^2$)

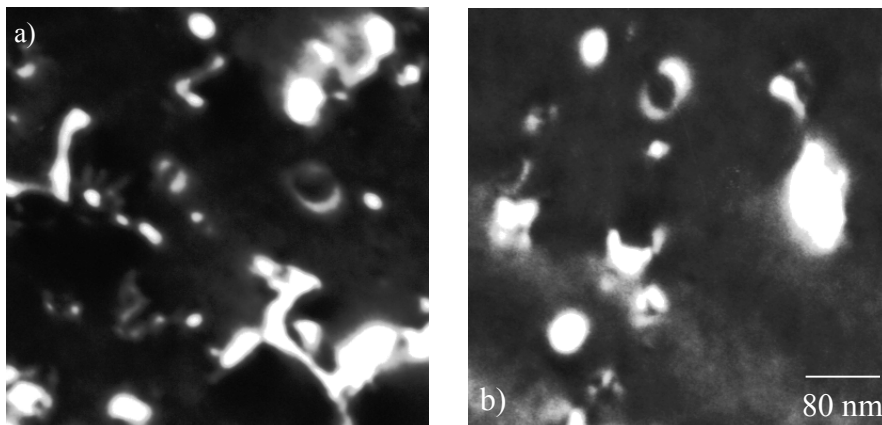


Figure 4-7 TEM of material laser annealed at 770 mJ/cm^2 and then thermally annealed at $750 \text{ }^\circ\text{C}$ for 2h and $900 \text{ }^\circ\text{C}$ for 5 m. Dislocation loops are observed in both material sets yet only the lower temperature anneal shows the presence of a strong peak. This implies that the peak is due to boron-interstitial clustering. (Implant conditions: $15 \text{ keV Si}^+ 1 \times 10^{15}/\text{cm}^2$, $1 \text{ keV B}^+ 1 \times 10^{14}/\text{cm}^2$)

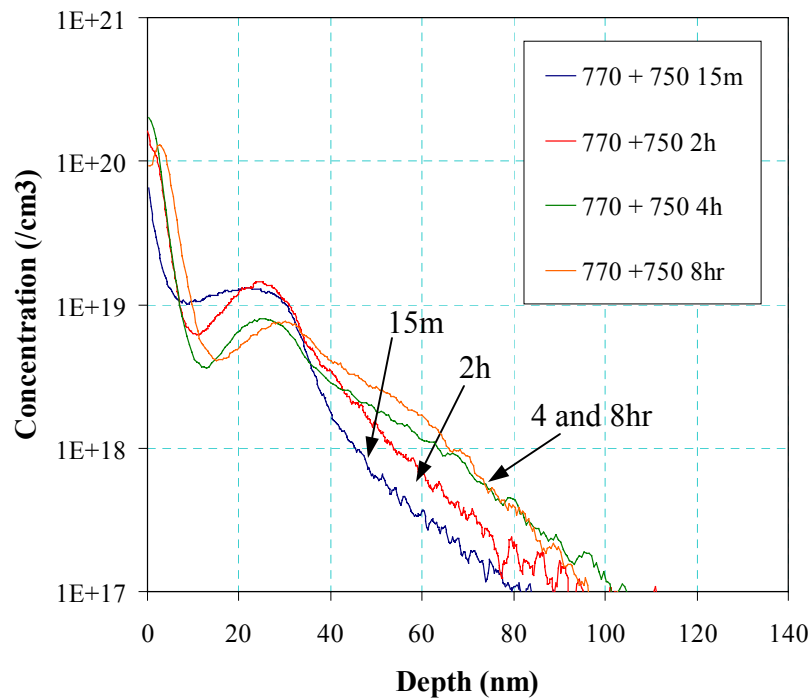
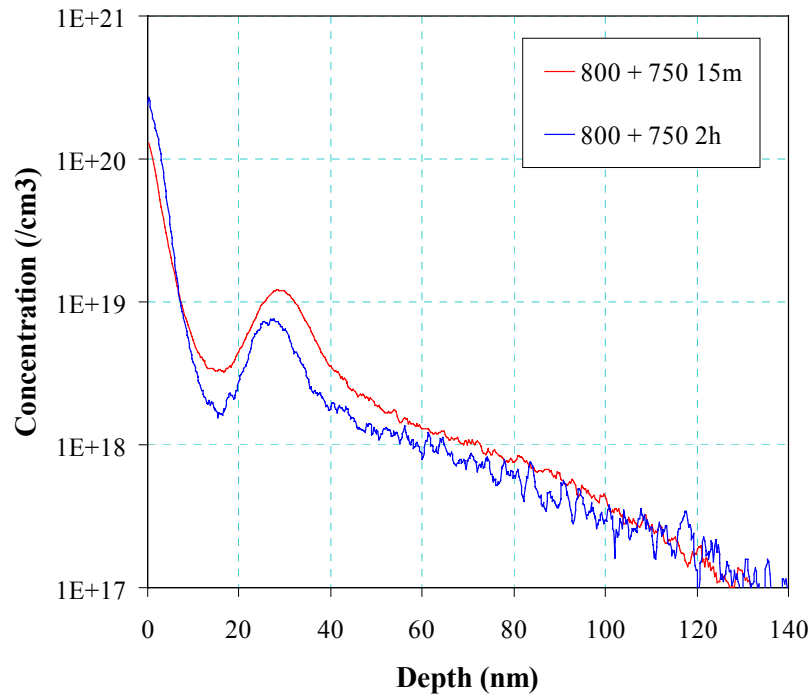


Figure 4-8 SIMS boron profile showing the difference in time to saturation for enhanced diffusion for material laser annealed at 770 compared to 800 mJ/cm². Anneal Temperature is 750 °C. (Implant conditions: 15 keV Si⁺ 1x10¹⁵/cm², 1 keV B⁺ 1x10¹⁴/cm²)

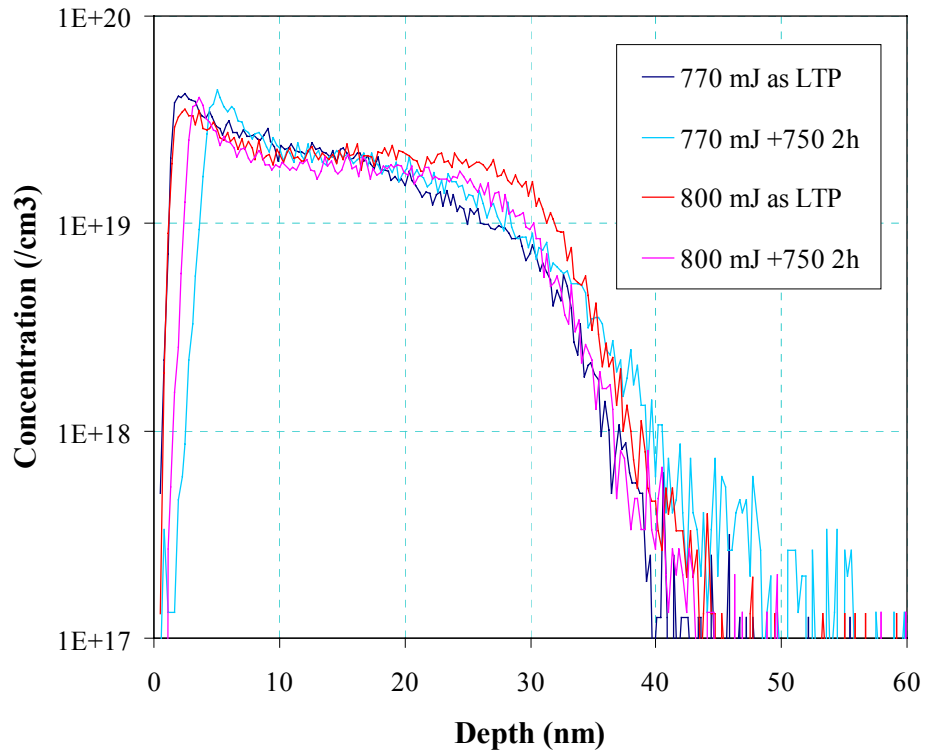


Figure 4-9 SIMS of antimony doped laser processed material (770 and 800 mJ/cm²). Two as-LTP as well as two post-LTP anneals at 750 °C 2h are shown. It is observed that there is no enhanced diffusion suggesting there is little to no flux of vacancies. (Implant conditions: 15 keV Si⁺ 1x10¹⁵/cm², 5 keV Sb⁺ 1x10¹⁴/cm²)

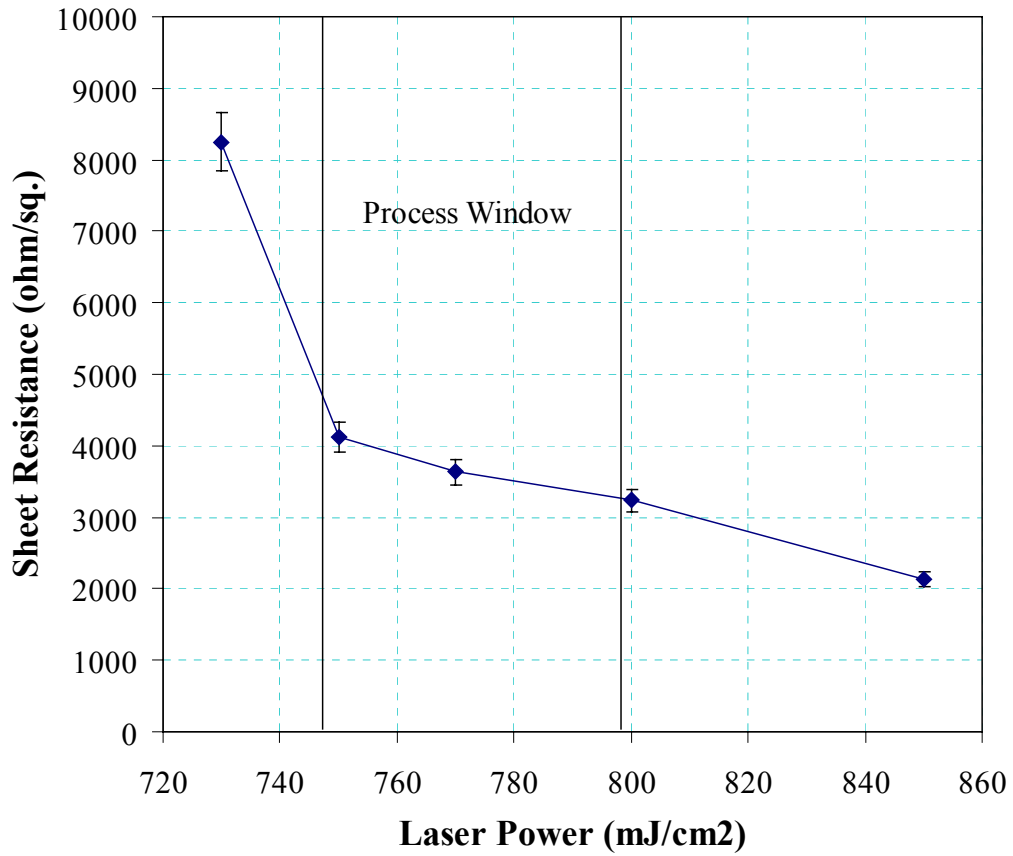


Figure 4-10 Sheet resistance for boron doped laser processed material as a function of the laser energy density. (Implant conditions: 15 keV Si⁺ 1x10¹⁵/cm², 1 keV B⁺ 1x10¹⁴/cm²)

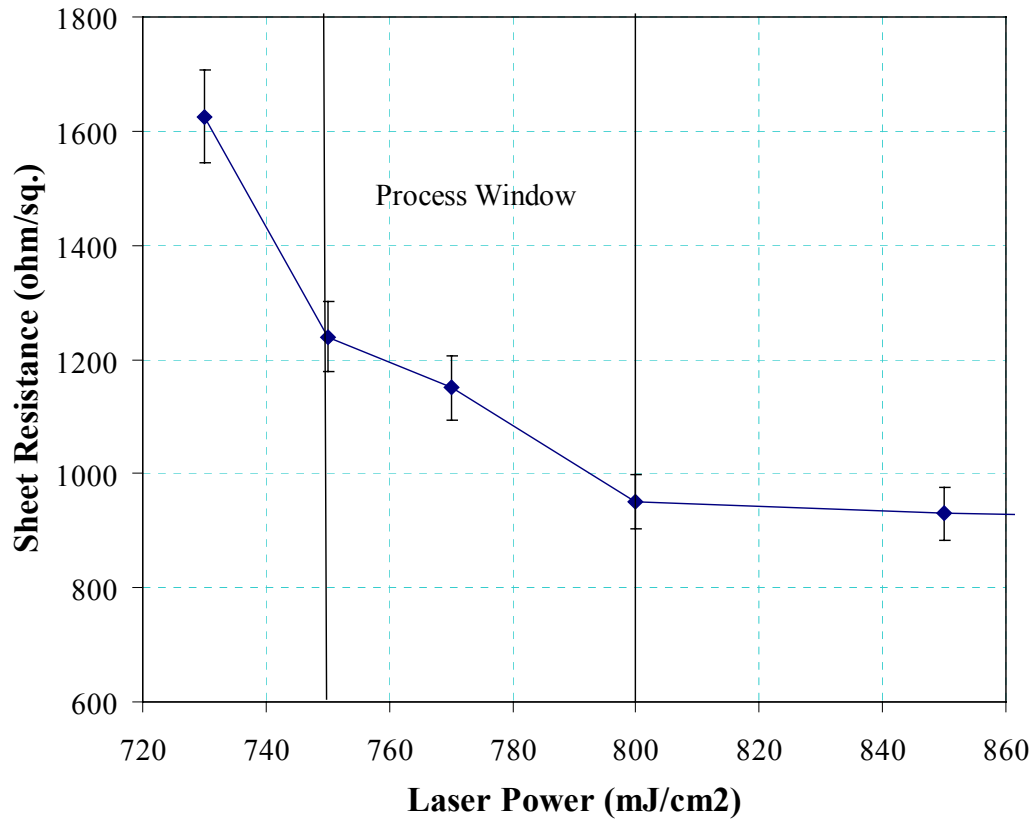


Figure 4-11 Sheet resistance for antimony doped laser processed material as a function of the laser energy density. (Implant conditions: 15 keV Si⁺ 1x10¹⁵/cm², 5 keV Sb⁺ 1x10¹⁴/cm²)

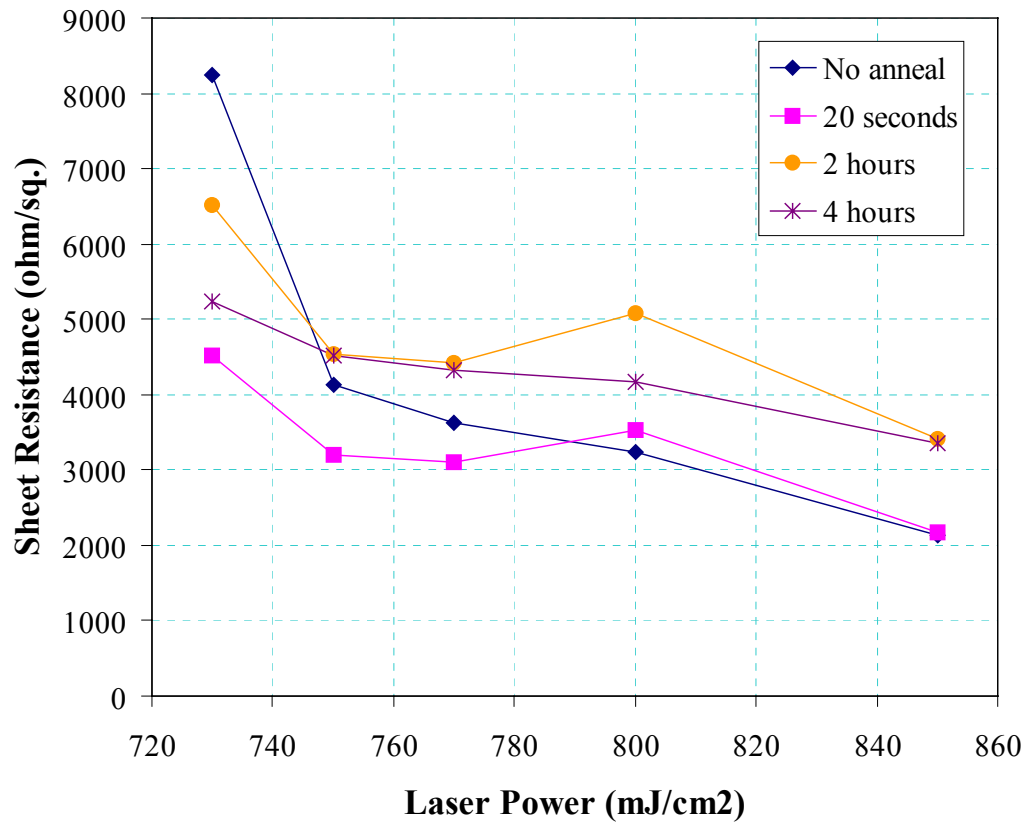


Figure 4-12 Sheet resistance for boron doped laser processed material as a function of the laser energy density. The material was then subjected to a 750 °C anneal for times between 20 s and 4 hours. (Implant conditions: 15 keV Si⁺ 1x10¹⁵/cm², 1 keV B⁺ 1x10¹⁴/cm²)

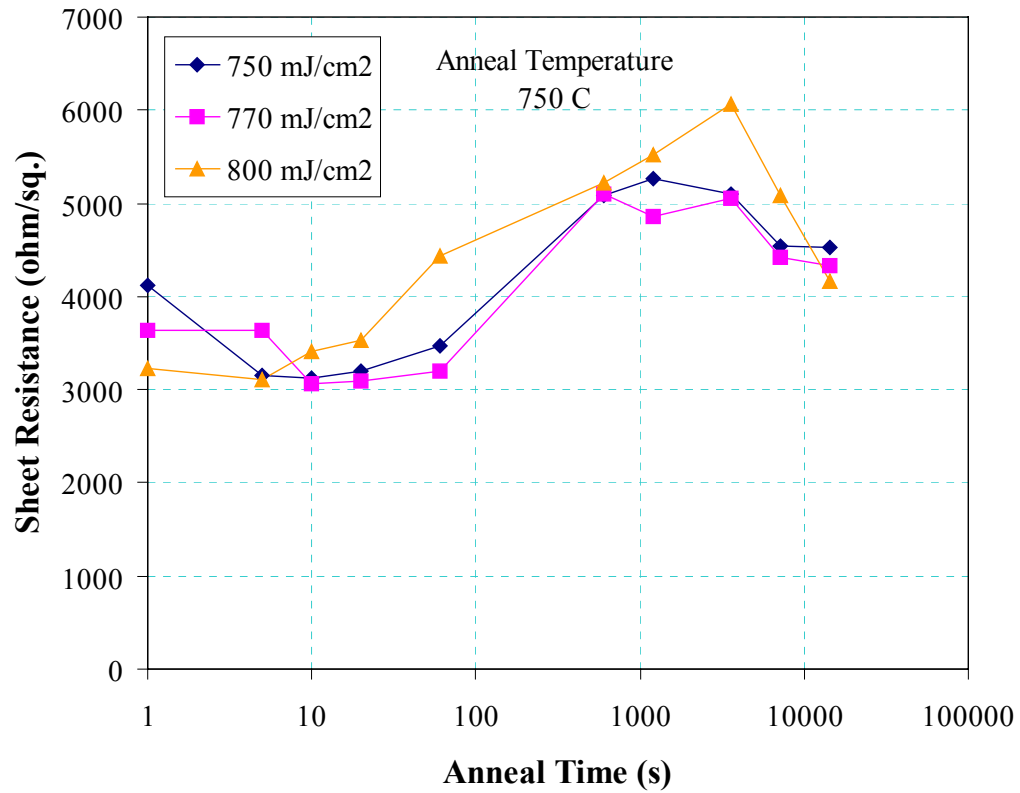


Figure 4-13 Sheet resistance of boron doped LTP material as a function of time at 750 °C for process window material laser annealed at 750, 770, and 800 mJ/cm². (Implant conditions: 15 keV Si⁺ 1x10¹⁵/cm², 1 keV B⁺ 1x10¹⁴/cm²)

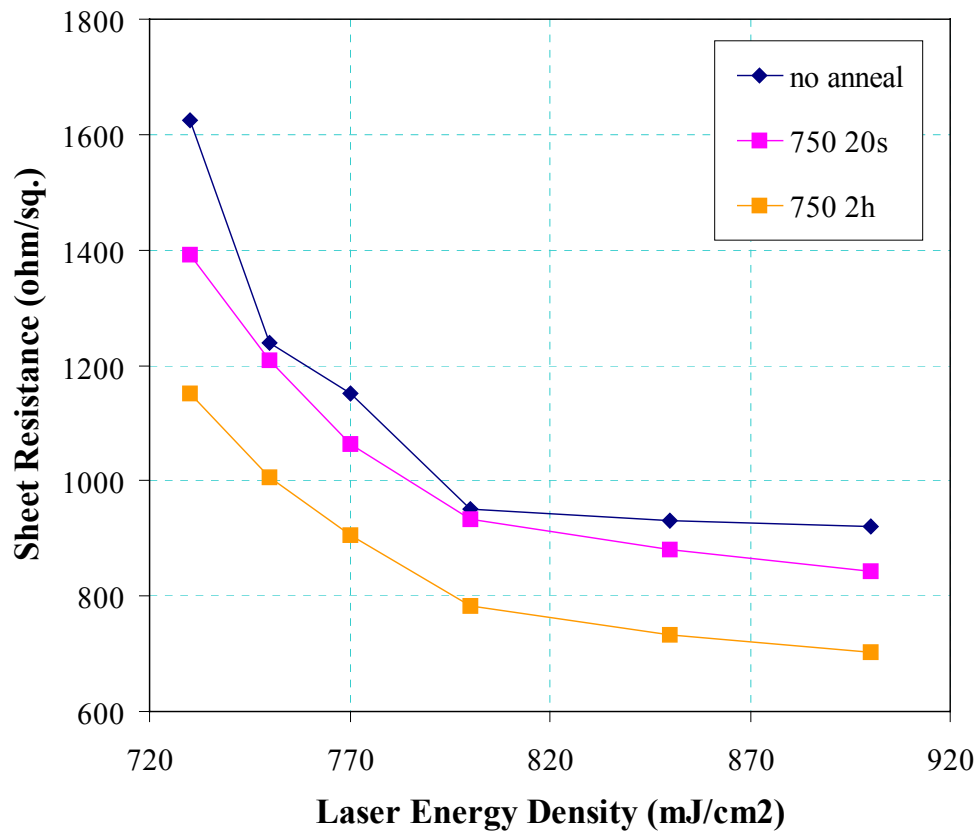


Figure 4-14 Sheet resistance for antimony doped laser processed material as a function of the laser energy density. The material was then subjected to a 750 °C anneal for times between 20 s and 2 hours. (Implant conditions: 15 keV Si⁺ 1x10¹⁵/cm², 5 keV Sb⁺ 1x10¹⁴/cm²)

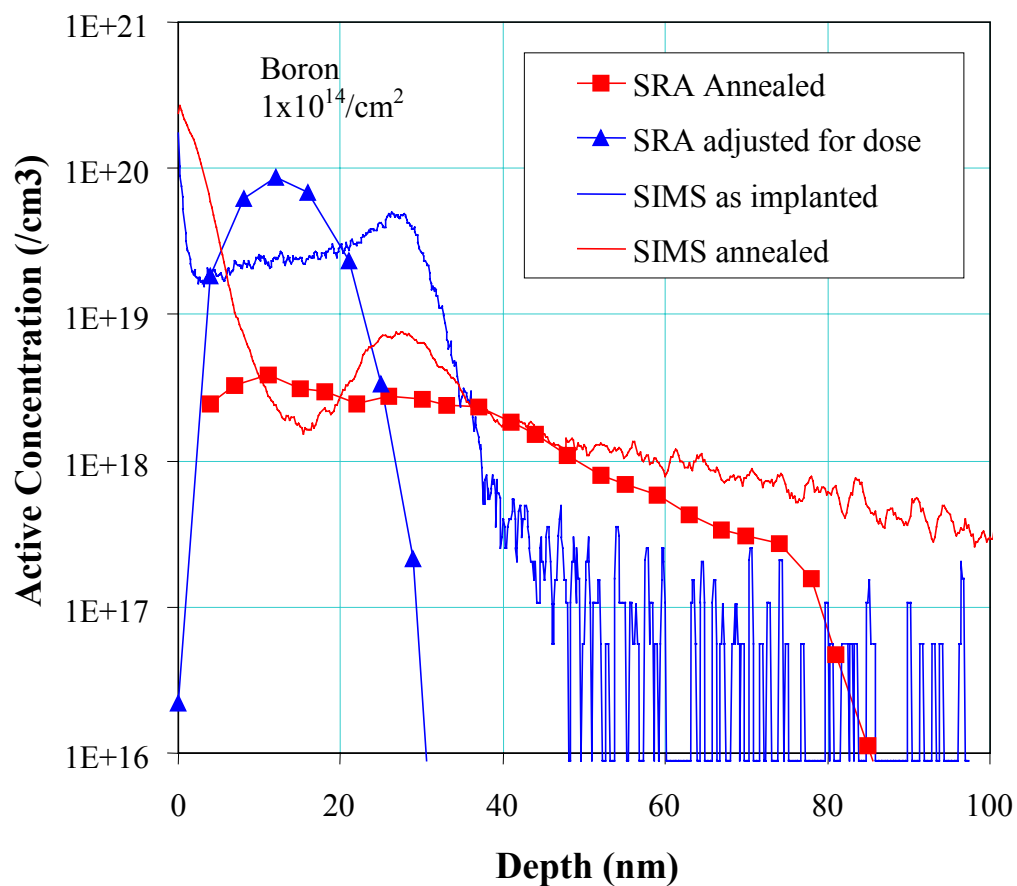


Figure 4-15 SRP of 800 mJ/cm² with no anneal and 750 2h. Included are SIMS profiles of the same material. These results confirm previous suggestions that the 30 nm deep peaks resolved in SIMS are in fact due to boron-interstitial clustering and that a total active dose of $1.3 \times 10^{13}/\text{cm}^2$ is observed. (Implant conditions: 15 keV Si⁺ $1 \times 10^{15}/\text{cm}^2$, 1 keV B⁺ $1 \times 10^{14}/\text{cm}^2$)

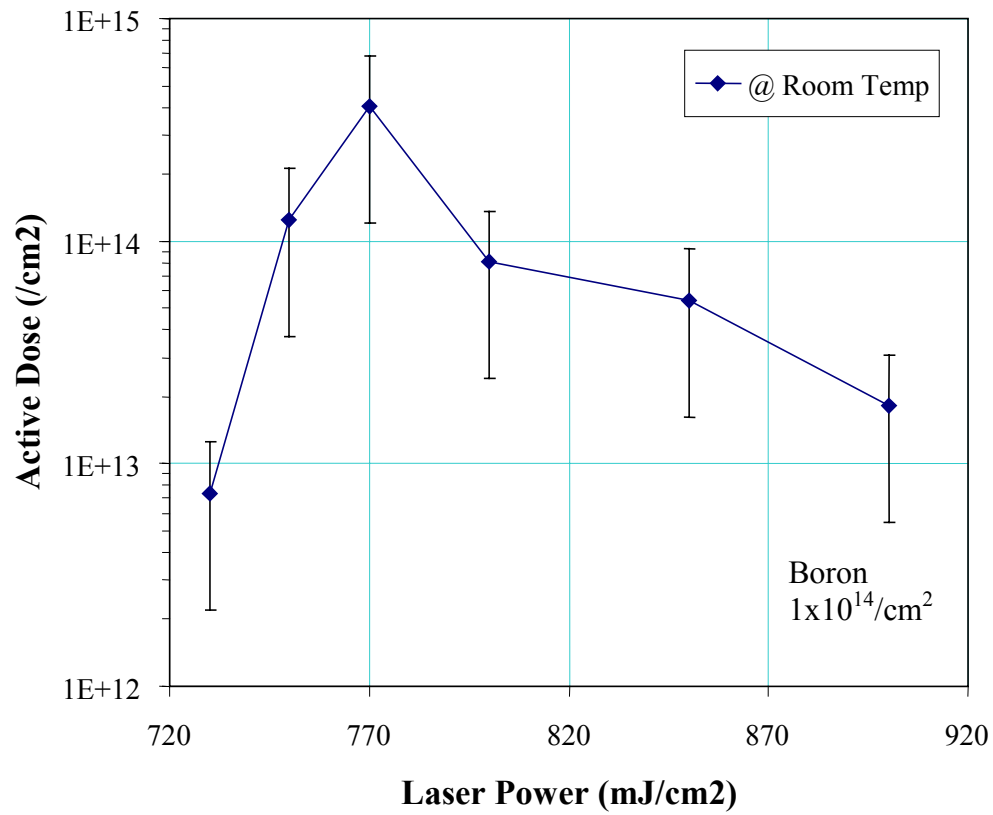


Figure 4-16 Hall effect of as-LTP material at room temperature. It was found that making good ohmic contact to the material was difficult. (Implant conditions: 15 keV Si⁺ 1x10¹⁵/cm², 1 keV B⁺ 1x10¹⁴/cm²)

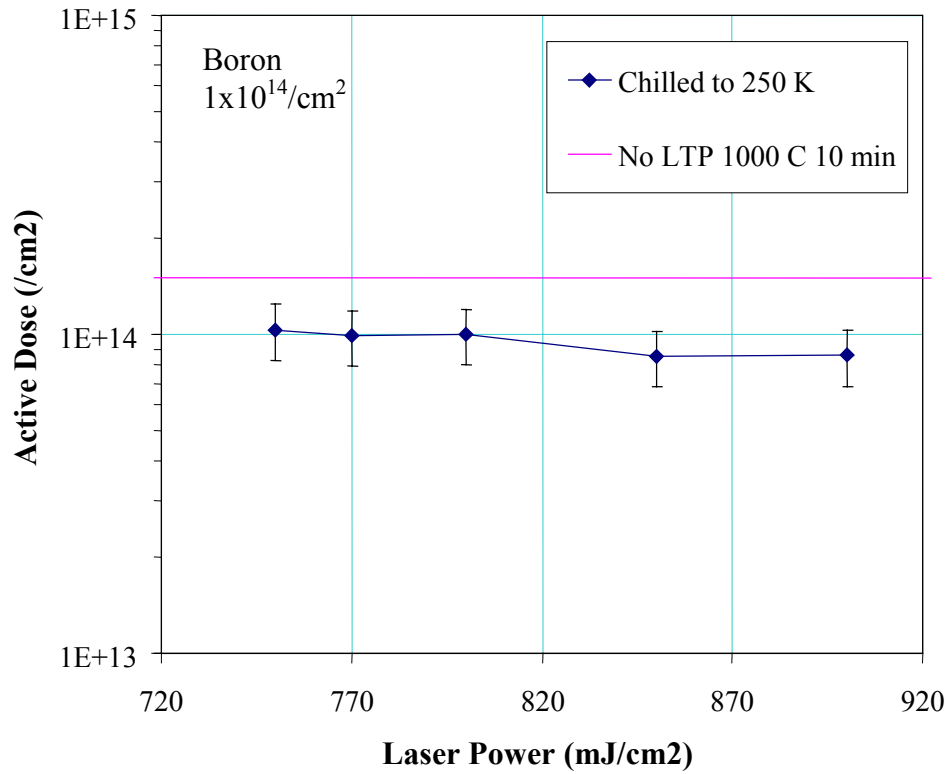


Figure 4-17 Hall effect measurement of active boron dose as a function of laser energy density, at temperatures below 250 K. Also included is the value determined for non-LTP material annealed at 1000 °C for 10 minutes. It is believed that this anneal should fully activate the boron dose and be useable as a reference standard. (Implant conditions: 15 keV Si⁺ 1x10¹⁵/cm², 1 keV B⁺ 1x10¹⁴/cm²)

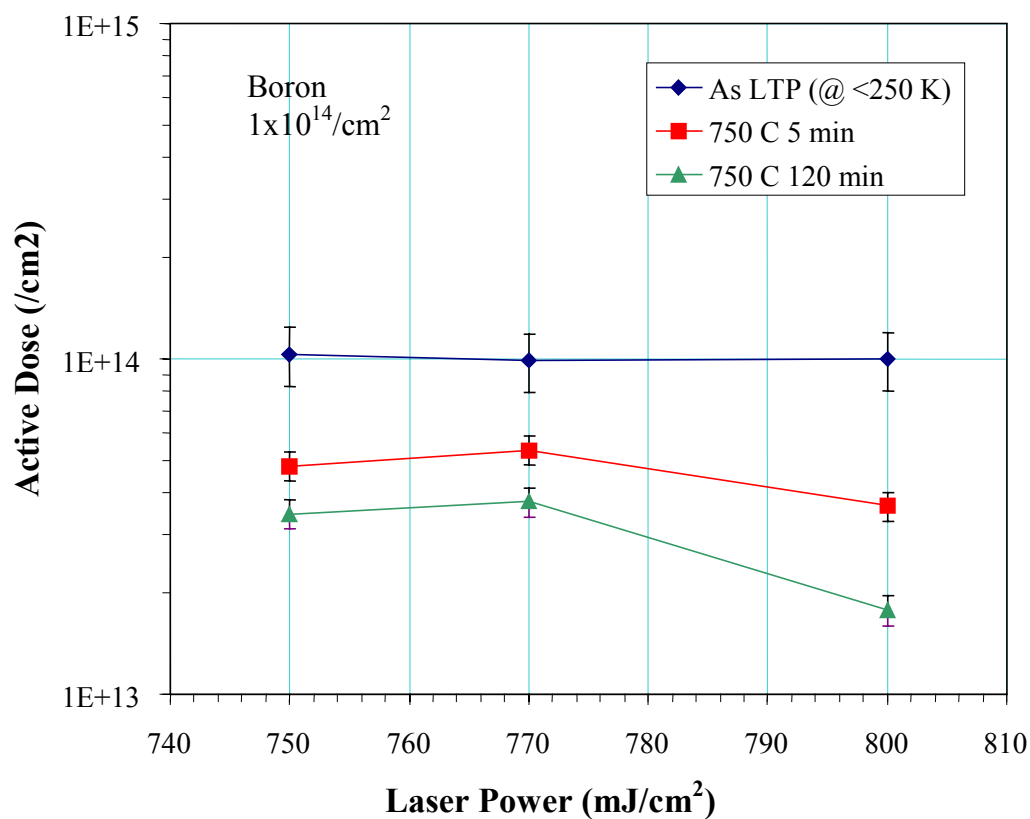


Figure 4-18 Hall effect measurement of active boron dose as a function of laser energy density used during laser annealing. Some material was then thermally annealed at 750 °C for 5 m and 2 hours. It is observed that the active dose for the 800 mJ/cm² materials matches well with the integrated dose measured via SRP. (Implant conditions: 15 keV Si⁺ $1 \times 10^{15} / \text{cm}^2$, 1 keV B⁺ $1 \times 10^{14} / \text{cm}^2$)

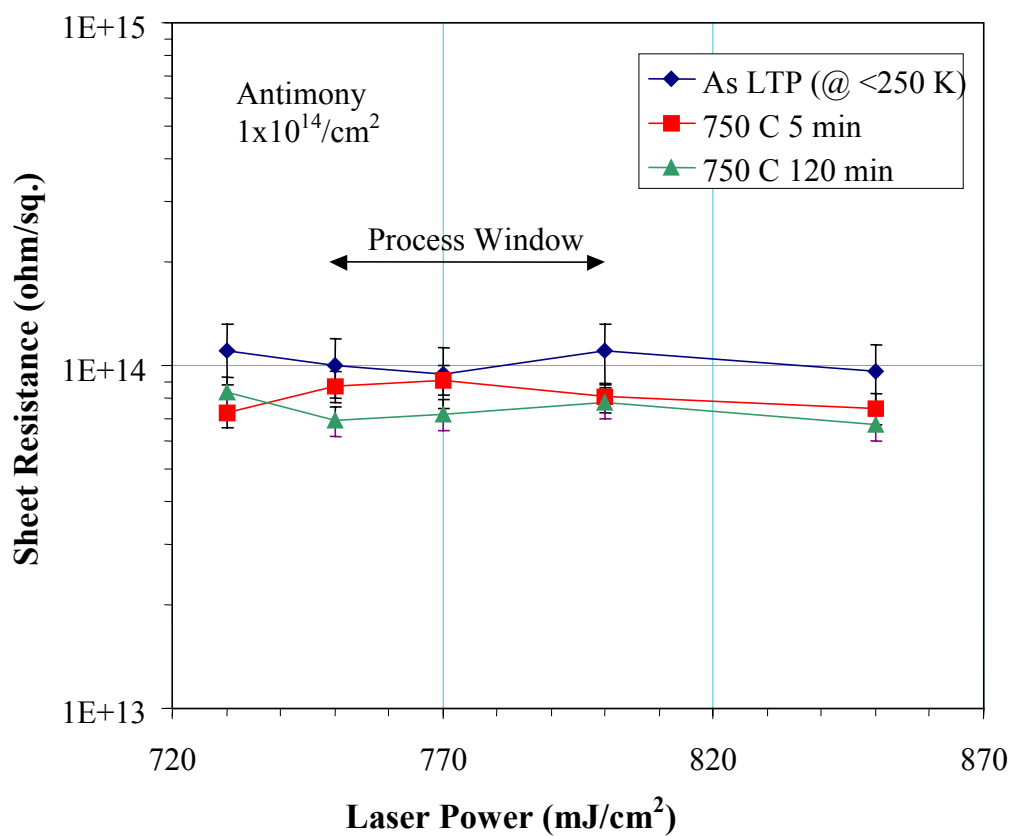


Figure 4-19 Hall effect measurement of active antimony dose as a function of energy density used during laser annealing. Little to no effect is observed during annealing at 750 °C for 5 m and 2 hours indicating no deactivation via precipitation of antimony. (Implant conditions: 15 keV Si⁺ $1 \times 10^{15} / \text{cm}^2$, 5 keV Sb⁺ $1 \times 10^{14} / \text{cm}^2$)

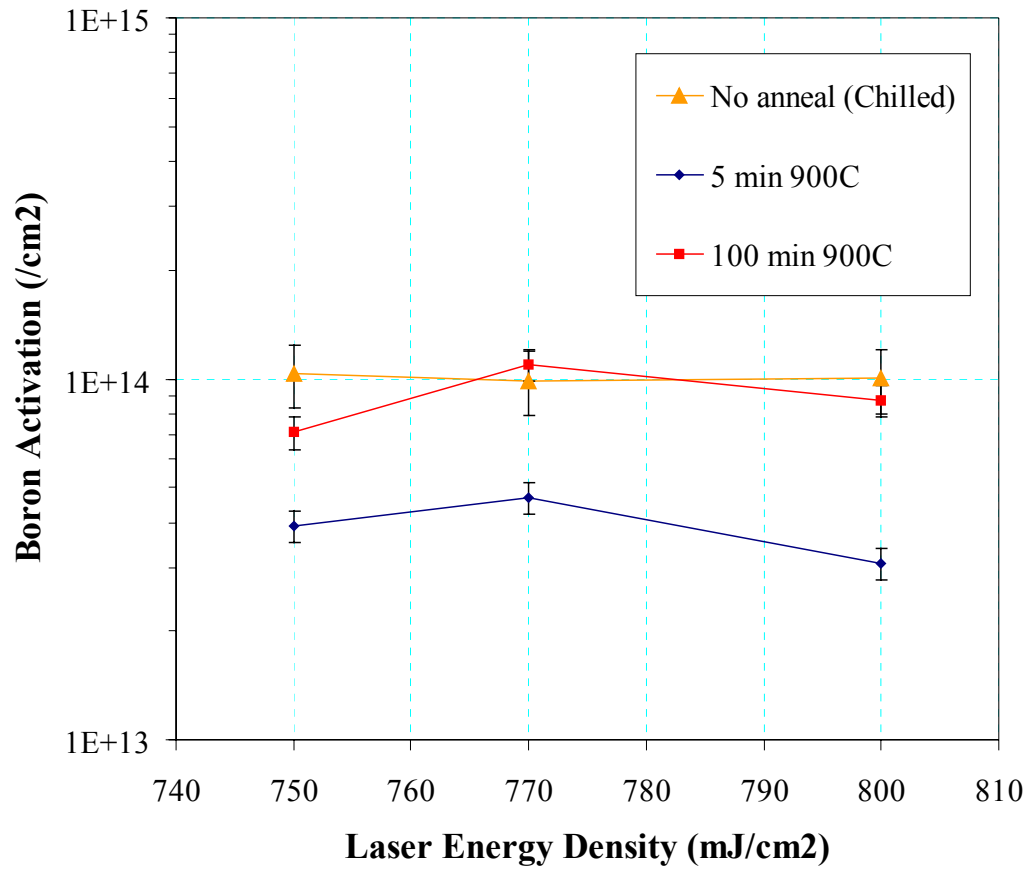


Figure 4-20 Hall active boron dose measurement as a function of energy density used during laser annealing. The material was then thermally annealed at 900 °C for 0, 5, and 100 minutes. (Implant conditions: 15 keV Si^+ $1 \times 10^{15}/\text{cm}^2$, 1 keV B^+ $1 \times 10^{14}/\text{cm}^2$)

CHAPTER 5 DISCUSSIONS AND CONCLUSIONS

This chapter will attempt to bring together the findings of the previous two chapters to create a global picture of the status of point defect populations and the possible factors that affect their behavior in laser processed silicon, namely the epitaxial defects that result from the rapid liquid phase epitaxy. To support these theories some of the experiments from the prior two chapters are repeated, but this time with the use of very low temperature annealing prior to laser annealing so that epitaxial defect densities can be varied without altering the laser anneal energy density. In addition, the chapter will explore other observed phenomena such as enhanced diffusion of boron for laser “overmelt” conditions and the possibilities of quenching in point defects during the rapid liquid phase epitaxy.

Initial Theories and Discussion of Results

In the previous two chapters it was observed that a number of interstitial mitigated phenomena, specifically transient enhanced diffusion of boron, boron-interstitial clustering and end of range dislocation loop evolution, were affected by the laser energy density used during laser thermal processing. However, given TEM findings in Chapter 3, it was suggested that the trapped interstitial density in loops was impacted by the presence of epitaxial defects that are formed as a result of the rapid liquid phase epitaxy during laser thermal processing, rather than the laser energy density itself. For the other two phenomena, it was also found that the magnitude of each of these was increased as the density of epitaxial defect decreased for a 750 °C, 2 hour anneal. In addition, for

diffusion of boron, it was observed that the time to TED saturation was similar to the time necessary for the dislocation loops to trap the highest density of interstitials. Figure 5-1 shows that both the junction motion and the maximum trapped interstitial concentrations occur during the same time periods for both the 770 and 800 mJ/cm² materials, at 2 and 4 hours, respectively. Given that there is evidence to suggest that the interstitial density trapped in dislocation loops is governed by the epitaxial defect density, we can also then suggest that the same process affects the enhanced diffusion. Why the dislocation loops in the 770 mJ/cm² material do not begin to dissolve after 4 hours, has yet to be determined.

It was also observed that for process window material with little to no epitaxial defects the magnitude of enhanced diffusion and point defect clustering were very similar to conventional material. This suggests that the source of interstitials is the same, namely the interstitials generated at the end-of-range via the implant amorphization step. However, these same materials showed only as much as 10% of the trapped interstitial concentration. This suggests that a different mechanism, or combination of mechanisms, is affecting the formation of end-of-range dislocation loop evolution.

Theories for Reduced Interstitial Population in Loops

Several mechanisms for this phenomenon are suggested to explain the reduced interstitial population trapped in dislocation loops. Given that dislocation loop evolution, boron-interstitial clustering, and transient enhanced diffusion are all interstitial based, these discussions will also pertain to those phenomena as well. These mechanisms will first be presented without regard for findings in previous chapters and then will be discussed in relation to those findings. Finally, a theory will be put forth to explain the phenomena and tested in the following section. These possibilities can be put into two

categories, processes that alter the number of interstitials available to form dislocation loops and processes that alter the nucleation mechanism.

Reduction of available interstitials

By reducing the number of interstitials available in the solution to form dislocation loops, the loops that do form will have a lower total number of trapped interstitials and thus be smaller in size. There are two ways that the interstitial concentration for loop formation can be reduced.

The first method is that they are annihilated. This would occur if, during the laser melt, enough energy was supplied to the system to allow interstitials sitting in the solid, just below the liquid-solid interface, to diffuse into the melt. The duration of the laser pulse is only between 15 and 30 nanoseconds, however the quench rates are on the order of 10^9 K/s with thermal gradients of 10^7 K/cm [Poa82]. Thus, for material just below the amorphous-crystalline interface that is just near the melting point of silicon, 1410 °C, the time spent at a temperature in excess of 1000 °C is on the order of 0.4 microseconds. For a silicon self-interstitial with a diffusion activation energy of 4.84 eV and pre-exponential of 914 cm²/s [Gös96], we find that even a 1350 °C anneal for 0.4 μ s results in only 0.6 nm of diffusion, or roughly one lattice parameter. Using TRIM to calculate the dose of interstitials immediately below the amorphous-crystalline interface reveals that less than 10% of the ion dose (implanted dose not including knock-ons) is located within 1 nm of the a-c interface. Thus, it is not expected that the energy provided by the laser anneal would be enough to eliminate more than 10% of the dose. Annihilation of interstitials could also occur if there existed a fast diffusion path for interstitials to diffuse towards the surface. It is known that for most species, diffusion along grain boundaries is significantly higher than through a bulk crystal, due to lower energy diffusion paths.

Prior to meeting the minimum energy requirements of the process window it is known that polycrystalline grains form due to incomplete melting of the amorphous layer and the lack of a crystalline template for epitaxy. Thus this phenomenon could be expected for sub-process window material, but would not be expected for process window material unless diffusion occurred dislocations. Given that the dislocation is itself composed of silicon this would be equivalent to the steady-state dissolution of the dislocation.

The second method is that the interstitials are restricted and not allowed to participate in the loop evolution process. This could occur if there were other defects that gettered the interstitials to them and captured them. These could either be submicroscopic defects such as dopant clusters, submicroscopic loops, or larger defects such as the epitaxial defects created during the recrystallization process. It has been shown that small impurities such as boron can be gettered to a dislocation line, but it is still unclear if a similar phenomenon occurs with self-interstitials.

Altered nucleation process

The second mechanism for reduced interstitial populations is that the laser melt changes the dislocation loop nucleation process, thus altering the evolution. In terms of heterogeneous nucleation, this could occur by altering the morphology of the nucleation interface, so as to change the number of possible nucleation sites. For laser processed material there does not exist an amorphous layer during the early stages of loop evolution like in conventional material. Therefore if the nucleation process were dependent on the state of the amorphous-crystalline interface, the laser process would dramatically affect it.

For homogeneous nucleation, the laser melt process could provide enough energy to the system to form sub-microscopic proto-loops that are composed of interstitials that

were able to perform one or two-hop diffusion. It has been shown by Camillo-Castillo that there is an optimum anneal temperature of 550 °C for the formation of proto-loops and that anneal temperatures above this result in a lower loops densities and trapped interstitial concentrations [Cam02]. It has already been determined that interstitials could move as far as one lattice parameter (0.543 nm), during the dissipation of the thermal energy provided by the laser, thus it remains feasible that proto-loops could form during this period.

Proposed Theory

Analyzing the above mechanisms with regards to results from Chapters 3 and 4, it can be stated with confidence that no single mechanism perfectly explains the annealing behavior of laser processed silicon. Analysis of material processed at the end of the process window shows that for both diffusion and activation, there is little variation from conventionally processed material. However, reducing the laser energy density results in boron diffusion profiles that are far shallower, even after up to 8 hours of annealing. This could be explained by the slow release of interstitials from the epitaxial defects, thus while the total interstitial population is unchanged the enhancement factor is smaller over a longer length of time.

Thus the only factor that cannot be explained by a trapping of interstitials by epitaxial defects is the formation of dislocation loops. For two energy densities studied, 770 and 800 mJ/cm², a similar maximum interstitial concentration in loops was observed, but this maximum was one-tenth that observed for conventional material. Given that loss of interstitials is unlikely, due to calculations above, and supported by results observed via diffusion and deactivation, it was then suggested that only an alteration of the nucleation process could explain the significant drop in the number of trapped interstitials

trapped in dislocation loops. Unfortunately there is little one can do to cleanly test differences in nucleation processes for laser thermal processing. However, it is possible to alter the epitaxial defect density created during LTP by varying the a-c interfacial roughness as shown by Banisaukas [Ban00]. In that work, three methods were used to vary the a-c interfacial roughness including implant temperature during amorphization, dose rate during amorphization, and finally very low temperature anneals (VLTA) prior to laser annealing. It was this last method that was used in this work to study the effects of the epitaxial defects on interstitial based behavior.

Very Low Temperature Annealing

So that the theories presented in the previous section could be tested, low temperature annealing of pre-amorphized silicon was performed prior to laser annealing in order to smooth the amorphous crystalline interface. It was found that a 450 °C 30 minute anneal efficiently decreased the amorphous-crystalline interfacial roughness without leading to any measurable amorphous layer regrowth, Figure 5-2. The material was then laser annealed at the lowest possible energy density in the process window, 750 mJ/cm², and analyzed in PTEM to determine the decrease in epitaxial defect density. Figure 5-3 compares both 750 mJ/cm² material with the VLTA and without. The 800 mJ/cm² material is also included for epitaxial defect density comparison. It is observed that the silicon receiving the VLTA prior to laser annealing has a subsequently lower epitaxial defect density when compared to samples that did not receive the VLTA. In fact, by using the VLTA on samples at the beginning of the process window, the epitaxial defect density can be reduced to levels observed for samples at the end of the process window. Given the low temperatures used for this VLTA, it is unlikely that there was any significant diffusion of the interstitials in the damage region. Thus it was believed

that the nature of the epitaxial defects can be discerned. It was possible that these anneals did affect any homogeneous or heterogeneous proto-loop nucleation processes however.

Loop Evolution

The material above was annealed at 750 °C for 2 hours and examined in TEM to determine the effects of the reduced epitaxial defect density on the dislocation loop evolution. It was observed that there was a dramatic increase in trapped interstitial concentration in loops for the samples receiving the VLTA when compared to samples not receiving the VLTA. Figure 5-4 shows a comparison of material laser annealed at 750 mJ/cm² with and without VLTA as well as a sample having received an 800 mJ/cm² laser anneal without VLTA. It is noted that the dislocation loop morphology of the VLTA sample is very similar to that of the sample at the end of the process window. This supports the theory that the epitaxial defects are inhibiting the formation of dislocation loops while they are present in the system. It does not however, explain the drastic difference between conventional and laser annealed loop morphologies.

Boron Diffusion

Boron doped material having received a VLTA prior to laser annealing was annealed at 750 °C for 2 hours to study the diffusion of boron with respect to non-VLTA material. Figure 5-5 shows the boron SIMS profiles before and after annealing. Two non-VLTA profiles, 750 and 800 mJ/cm², are included for comparison. Little to no difference is observed in the initial as-LTP profiles between material receiving the VLTA and those not receiving it. However, upon annealing, it is observed that for the material receiving a VLTA, and therefore a reduction of epitaxial defects, there is an increase in interstitial activity in this case enhanced diffusion of boron. In fact, the enhancement

observed is nearly identical to that of material laser annealed at the end of the process window and on the order of a 34X enhancement over base diffusion.

Deactivation

The effects of a VLTA on LTP material were studied using Hall measurements. The material was then thermally annealed at 750 °C for 5 minutes and 2 hours and the active dose was measured using Hall effect. It was observed that the active dose for the VLTA material very closely matched that of material with a similar initial epitaxial defect density rather than that of a similar laser processing energy density, Figure 5-6. This was observed for both the 5 minute and 2 hour anneals.

Thus by using VLTA and low process window energy densities, it was shown that all three interstitial related phenomena were increased to levels similar that of material laser processed at the end of the process window. This further supports the theory that it is the epitaxial defects that are responsible for controlling interstitial populations in laser processed silicon, rather than the laser energy density used during laser annealing. Figure 5-7 shows the normalized results of all three interstitial based phenomena as a function of initial epitaxial defect density.

Beyond the Process Window

Thus far, most work has focused on the behavior of material laser annealed within the process window during subsequent thermal annealing. The primary reason for this is that within the process window, the junction depth is defined by the pre-amorphization implant rather than by the laser energy density. Once the process window is exceeded and the melt begins to penetrate into the interstitial rich end-of-range region, it would be expected that any and all interstitial mitigated phenomenon would drop off as a function of consumed interstitial profile (Figure 5-8). However this is not uniformly observed.

For interstitials trapped in dislocation loops, it was shown in Chapter 3 that laser energy densities of 825 mJ/cm^2 resulted in as much as a 90% drop in trapped interstitials when compared to material laser annealed at 800 mJ/cm^2 for a $750 \text{ }^\circ\text{C}$ 2 hour anneal. For deactivation in an hyper process window condition, it is observed in Figure 5-9 that the recovery of active boron also occurs at a more rapid rate than the loss of interstitials in the EOR would predict for an 850 mJ/cm^2 laser anneal given its melt depth. The most unexpected result, however, comes during the analysis of diffusion in post-process window material, Figure 5-10. After a $750 \text{ }^\circ\text{C}$ 2 hour anneal, it is observed that the boron junction depth is independent of laser energy density and was maintained at a depth of about 100 nm. Conversion of these initial and final depth profiles shows that while the diffusion enhancement is decreasing, due to a deeper starting depth, it does not drop off anywhere near the rate at which interstitials are being consumed.

These results led to a theory that perhaps the LTP process itself generated excess interstitials during solidification. This could be explained by a quenching process that trapped interstitials in solution at concentrations equivalent to equilibrium values just below the melt temperature. Using the activation energies for the intrinsic formation of interstitials and vacancies determined by Tan and Gosele [Tan 85], it can be determined that at temperatures just below the melting temperature of silicon the equilibrium concentration of interstitials is roughly $3.5 \times 10^{17} / \text{cm}^3$, which is nearly seven orders of magnitude greater than the equilibrium concentration at $750 \text{ }^\circ\text{C}$. Thus while the concentration of interstitials is still far below that produced by an implant, roughly another three orders of magnitude, it is still possible that some enhanced diffusion could

be expected. In order to test if this is truly the case, several experiments were performed and are discussed in the following section.

Crystal Melt Conditions

This section will discuss the effects of performing laser thermal processing using laser energy densities beyond the process window as well as laser annealing of crystalline materials. The purpose of this is to attempt to understand the nature of point defects in the recrystallized materials independent of epitaxial defects.

A silicon wafer was implanted with a 1keV $1 \times 10^{14}/\text{cm}^2$ boron implant. It was then cleaved into equal halves. One half was left as-implanted. The other half was thermally annealed in a nitrogen ambient furnace at 800 °C for 60 minutes to anneal out the implant damage. Each half was then laser annealed with an energy density of 850 mJ/cm² with a 308 XeCl excimer laser.

As-implanted

The as-implanted material was thermally annealed at 750 °C in a nitrogen ambient furnace for 2 hours and then analyzed with SIMS to monitor any diffusion. Figure 5-11 shows the SIMS profile of the as-implanted material prior to laser annealing, after laser annealing, and after laser annealing with thermal anneal. It was observed that the melt depth of the laser was approximately 48 nm, as determined by the end of the flat concentration profile. This depth should have been deep enough to melt past any damage produced by the boron implant. However, upon annealing a junction motion of nearly 20 nm was observed, or an enhancement of roughly 12x, given a standard diffusion of length of 1.63 nm for a 750 °C 2 hour anneal. While the SIMS profile for the as-laser annealed profile shows that all the implant damage should have been consumed by the melt, it is

important to compare these results with those below where the implant damage is removed.

Annealed

The material thermally annealed prior to laser annealing was then subsequently annealed again in a nitrogen ambient furnace at 750 °C for 2 and 4 hours. SIMS was used to monitor any diffusion as well as determine initial profiles. The laser-annealed profile shows a melt depth of approximately 60 nm, nearly 12 nm deeper than in the previous experiment. When compared to the annealed-implant profile it can be determined that the melt was not deep enough to consume the entire boron profile which extends to nearly 87 nm. However, given that the profile had already been annealed, it was not expected that there would be any remaining implant related damage. It was observed that after the first 2 hours of annealing, a total junction motion of 11 nm was observed, or a 7x enhancement over inert diffusion. Continued annealing for up to 4 hours resulted in a total junction motion of 17 nm, or a total diffusion enhancement of 5x.

Thus in two different experiments it was shown that there existed an enhanced diffusion resulting from laser annealing of crystalline silicon, and in each case it was determined that little to no interstitial supersaturation should exist from other sources. This strongly suggests that there is a trapping of interstitials that occurs during the rapid solid phase epitaxy of upon the laser melting of silicon.

Previous work by Rousseau and Takamura did not suggest the presence of either an interstitial or a vacancy supersaturation due to the rapid resolidification of the melt [Rou94a, Tak01]. In both these works all point defect supersaturations were attributed to the deactivation of dopant via Frenkel pair formation and subsequent dopant point defect clustering. Both authors found that an interstitial supersaturation was created by the

deactivation of arsenic or phosphorus. Takamura suggested that the boron and antimony deactivation method was via a precipitation method that did not greatly perturb the point defect populations.

Summary

This chapter reflected upon findings in the preceding two chapters, discussed those findings, and then presented a theory to explain those findings. It was proposed that laser annealing within the process window does not directly affect the point defect population created by the amorphization implant step. However, the laser energy density selected does affect the density of epitaxial defects and it is these defects that inhibit the participation of silicon interstitials in interstitial based phenomena such as dislocation loops formation and evolution, enhanced diffusion of boron, and boron-interstitial clustering. Moreover, the dissolution of these defects controls the release of these interstitials such that the time constant for each of these reactions is delayed with greater number densities of defects. To test this theory, experiments were performed to vary the epitaxial defect density without varying the laser energy density used during laser annealing. It was found that there was indeed a relationship between the density of epitaxial defects and the magnitude of interstitial based phenomena. It was also proposed that differences in dislocation loop evolution between conventional and laser processed material were the result of differences in nucleation methods but this theory was not tested.

The effect of exceeding the laser energy process window was also studied. It was expected that as the laser energy density was increased and the laser induced melt encroached upon the end-of-range damage, a proportional decrease in interstitial based phenomena would be observed. While this was the case for dislocation loop evolution

and boron-interstitial clustering, enhanced diffusion of boron was observed to remain rather high. Thus it was proposed that there might be a quenching of interstitials during the rapid solidification of silicon at levels predicted by thermodynamics. This theory was tested by laser melting boron doped single crystal silicon and monitoring any enhanced diffusion during subsequent thermal annealing. It was observed in two experiments that there was indeed an enhanced diffusion of boron and that the interstitials causing this enhancement could only have come from the laser melting process.

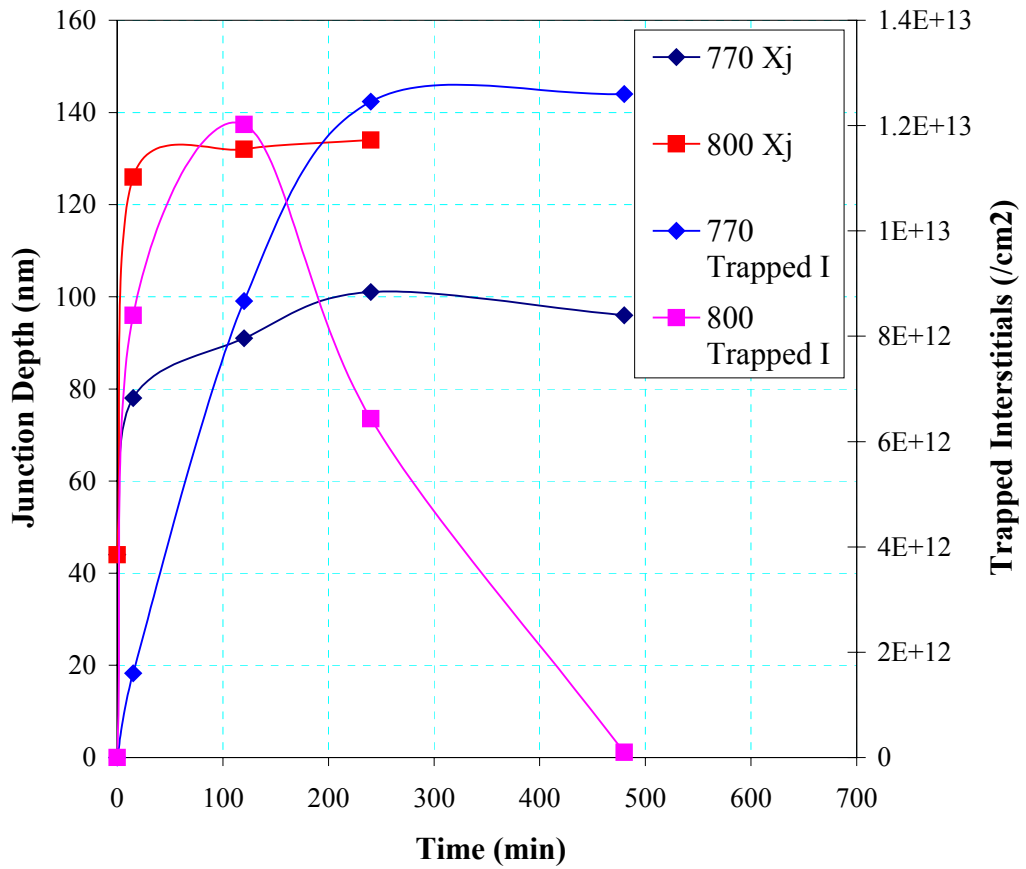


Figure 5-1 Boron junction depth and trapped interstitial concentration as a function of anneal time at 750 °C. It is observed that for both materials (770 and 800 mJ/cm^2) the time necessary to achieve the deepest junction depth is also the time necessary to trap the maximum interstitial population in loops. (Implant conditions: 15 keV Si^+ $1 \times 10^{15}/\text{cm}^2$, 1 keV B^+ $1 \times 10^{14}/\text{cm}^2$)

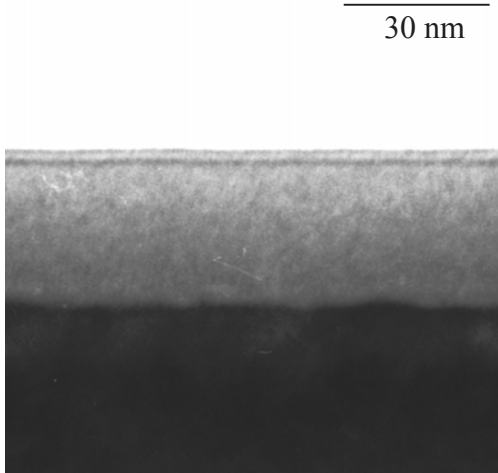


Figure 5-2 XTEM showing the amorphous layer depth after a 450 °C 30 min VLTA. No amorphous layer regrowth was observed. (Implant conditions: 15 keV Si⁺ 1x10¹⁵/cm², 1 keV B⁺ 1x10¹⁴/cm²)

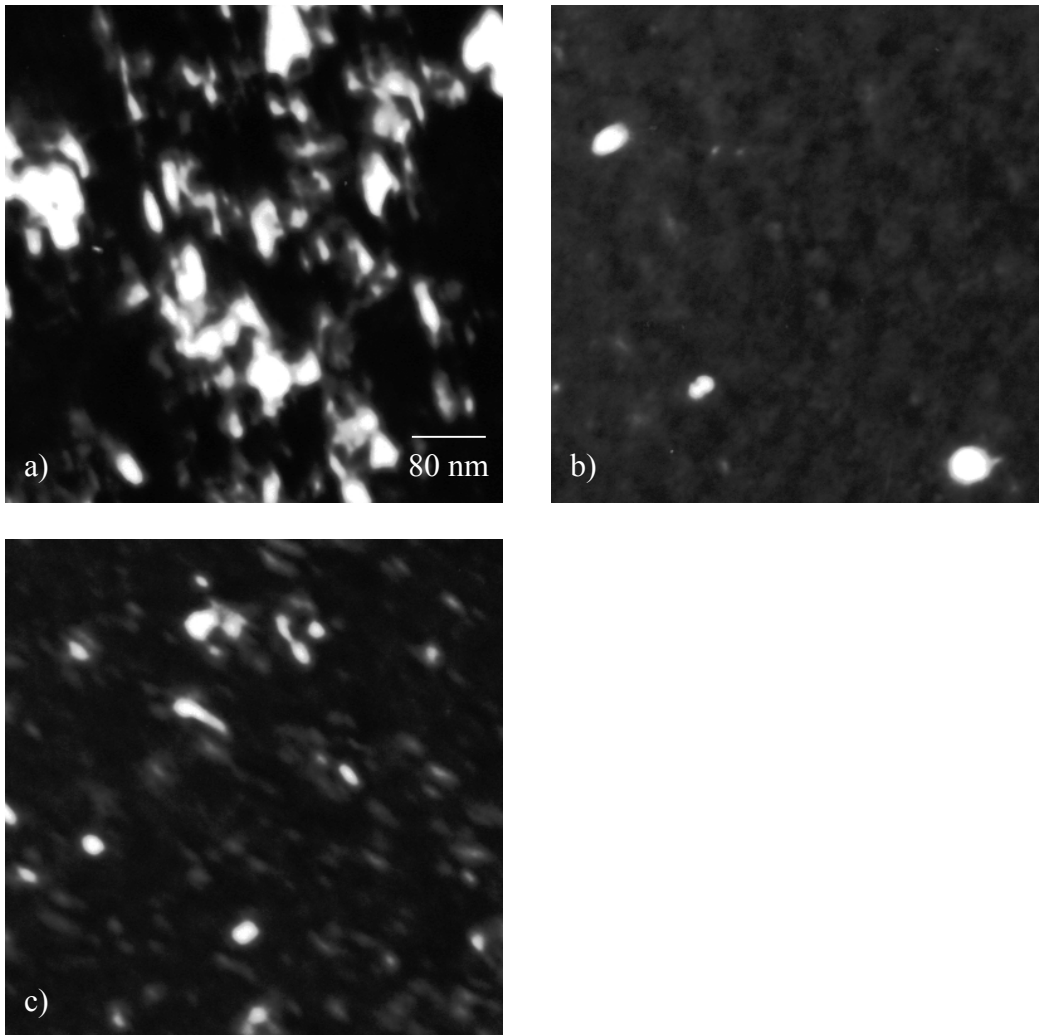


Figure 5-3 PTEM showing as-LTP defect densities for material having first received a) no anneal followed by 750 mJ/cm^2 , b) no anneal followed by 800 mJ/cm^2 , and c) a 450°C 30 minute anneal followed by 750 mJ/cm^2 . It is observed that the material that was pre-annealed more closely resembles the material having received the higher laser energy density anneal. (Implant conditions: $15 \text{ keV Si}^+ 1 \times 10^{15}/\text{cm}^2$, $1 \text{ keV B}^+ 1 \times 10^{14}/\text{cm}^2$)

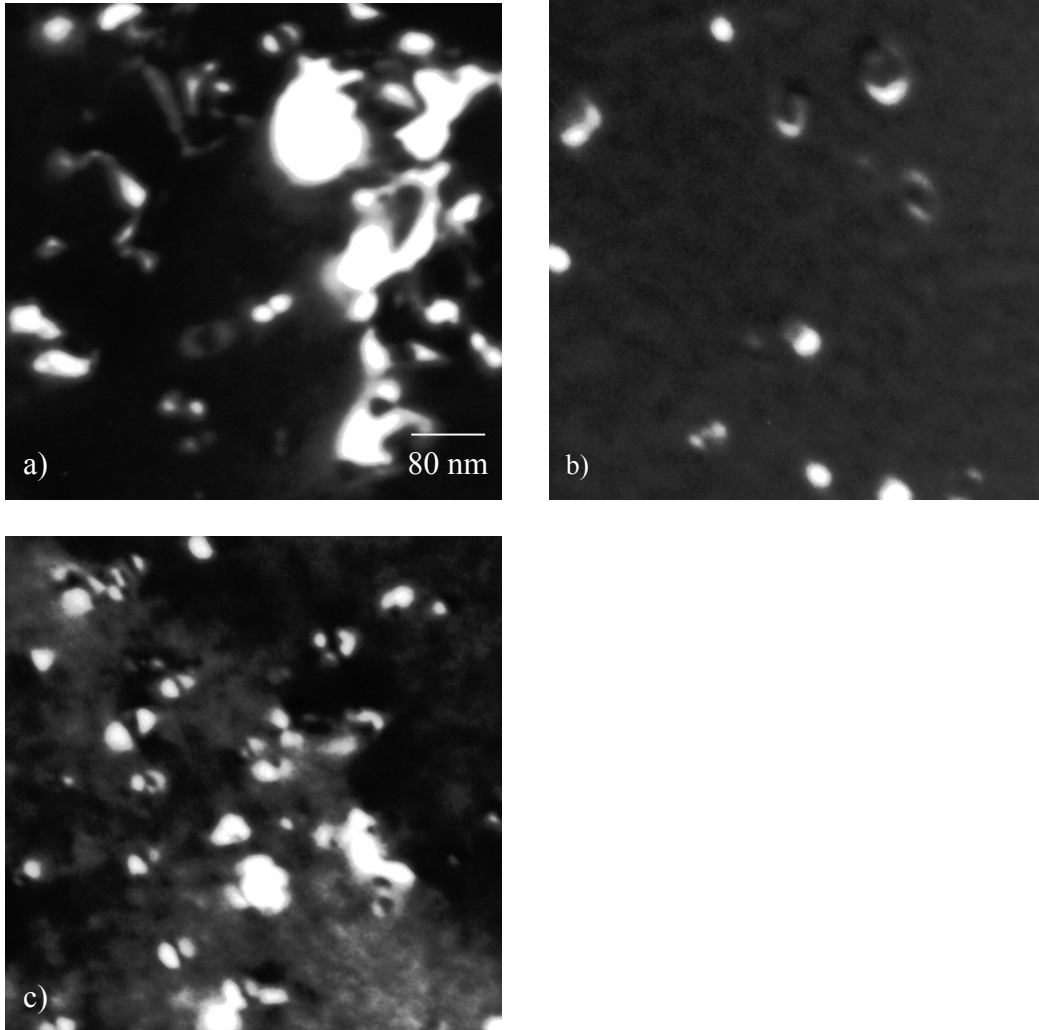


Figure 5-4 PTEM showing LTP material having first received a) no anneal followed by 750 mJ/cm^2 , b) no anneal followed by 800 mJ/cm^2 , and c) a $450 \text{ }^\circ\text{C}$ 30 minute anneal followed by 750 mJ/cm^2 . All material was then annealed at $750 \text{ }^\circ\text{C}$ for 2 hours to study the dislocation loop evolution. (Implant conditions: $15 \text{ keV Si}^+ 1 \times 10^{15}/\text{cm}^2$, $1 \text{ keV B}^+ 1 \times 10^{14}/\text{cm}^2$)

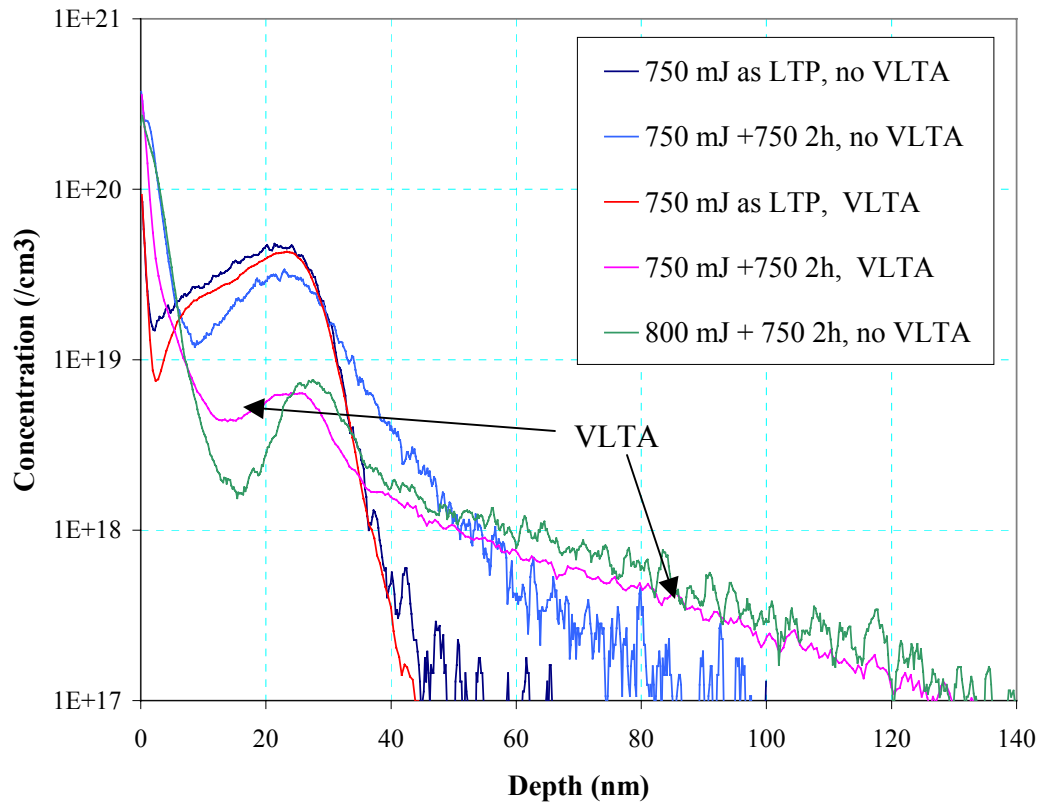


Figure 5-5 SIMS boron profiles analyzing the effect of a VLTA (450 °C 30 minutes) prior to laser annealing. It is observed that the material having received the VLTA more closely matches those materials laser annealed near the end of the process window (800 mJ/cm²) than those with the same laser anneal (750 mJ/cm²). (Implant conditions: 15 keV Si⁺ 1x10¹⁵/cm², 1 keV B⁺ 1x10¹⁴/cm²)

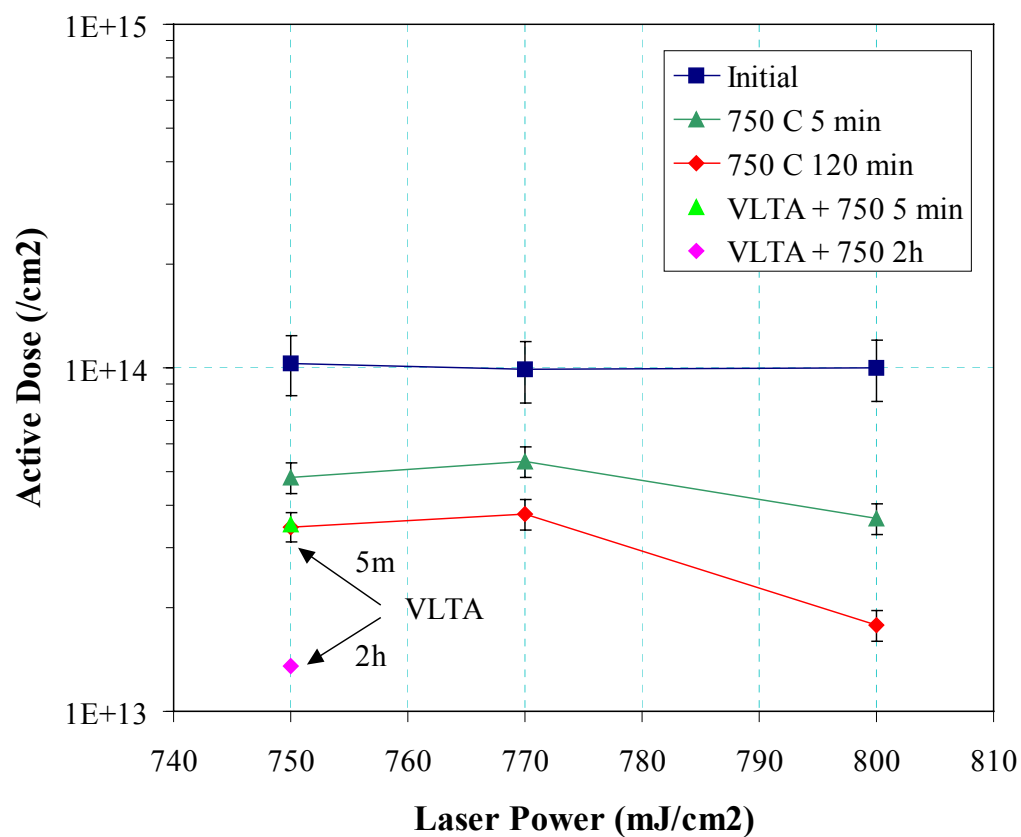


Figure 5-6 Hall effect active boron dose measurements showing the effect of VLTA on deactivation at 750 °C for 5 minutes and 2 hours. It is observed that the values for the pre-annealed material more closely match those laser-annealed near the end of the process window (800 mJ/cm²). (Implant conditions: 15 keV Si⁺ 1x10¹⁵/cm², 1 keV B⁺ 1x10¹⁴/cm²)

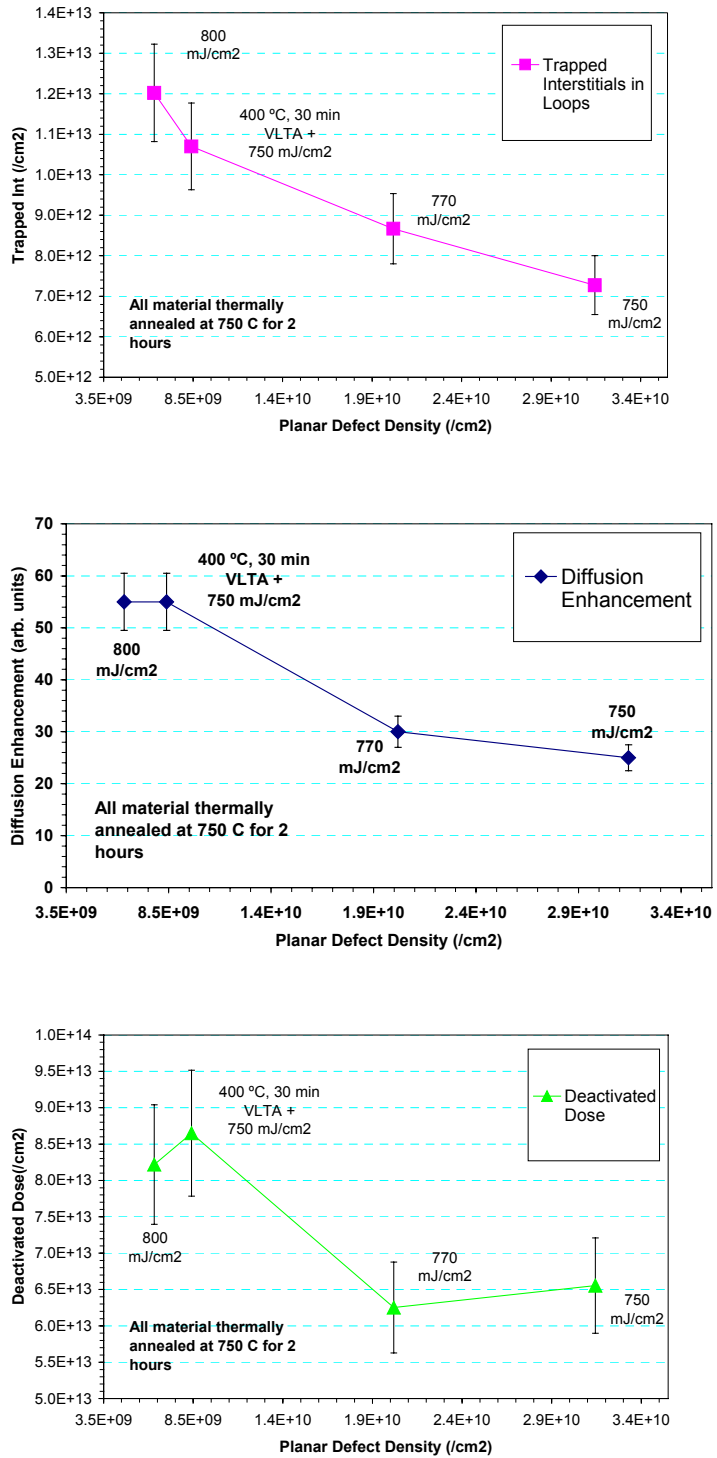


Figure 5-7 Plots showing all three interstitial based phenomenon as a function of the epitaxial defect density. For all three there is a trend observed that as the epitaxial defect density decreases, there is an increase in interstitial activity. (Implant conditions: 15 keV Si⁺ 1x10¹⁵/cm², 1 keV B⁺ 1x10¹⁴/cm²)

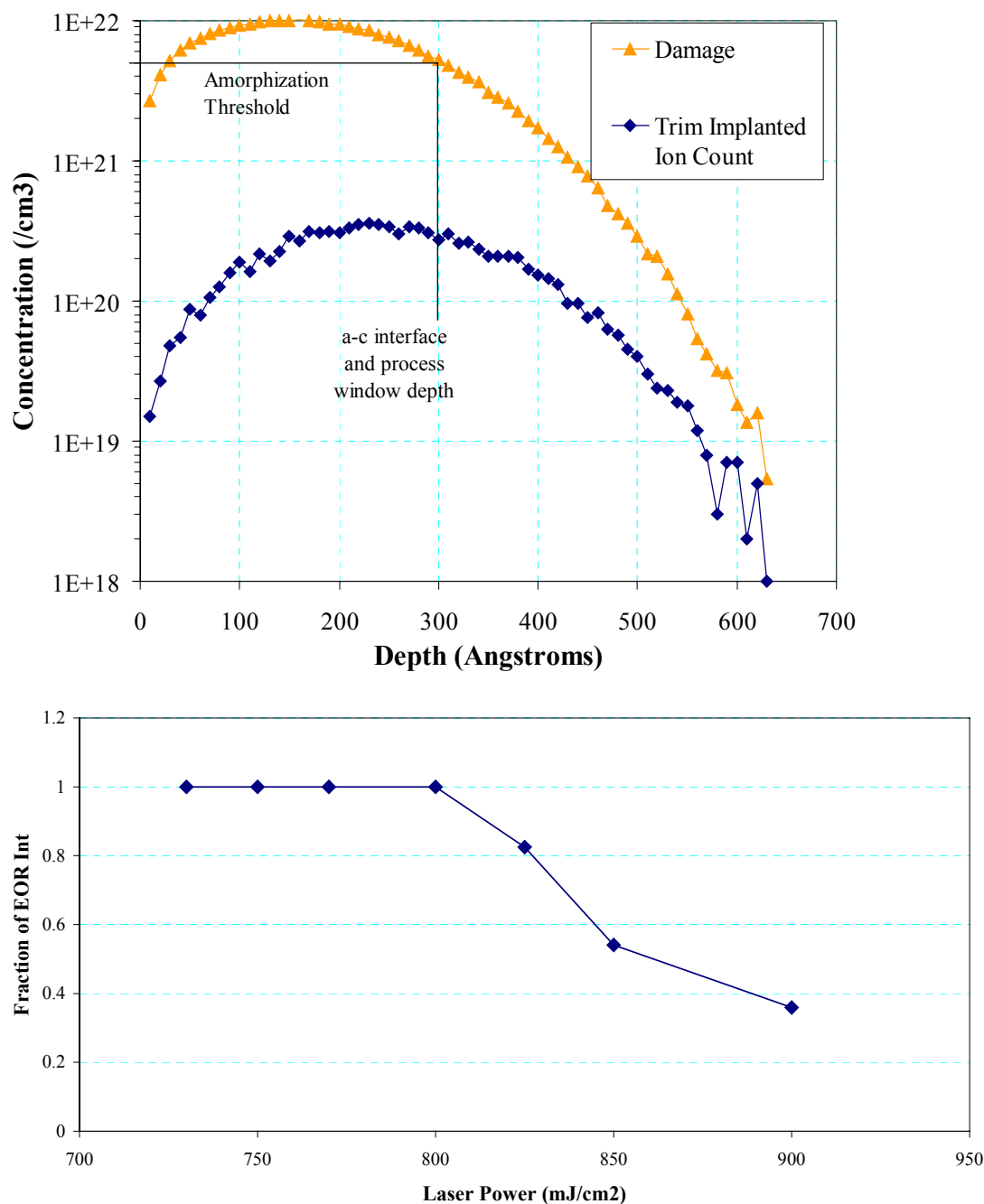


Figure 5-8 SRIM simulation of 15 keV Si⁺ 1x10¹⁵/cm² implant. The left axis plots the damage concentration profile, while the right axis plots the remaining fraction of the total interstitial dose. The depth to which the laser melts (determined via SIMS) is shown on the plot. Below, the fraction of initial interstitials, 3.2x10¹⁴/cm², is plotted as a function of laser energy density. (Implant conditions: 15 keV Si⁺ 1x10¹⁵/cm², 1 keV B⁺ 1x10¹⁴/cm²)

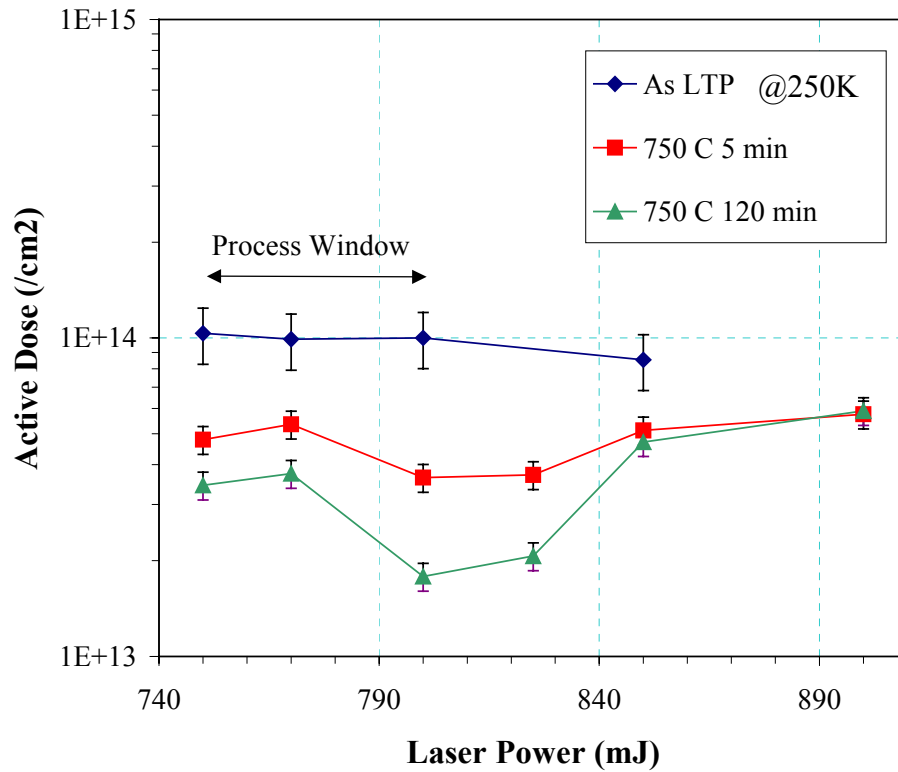


Figure 5-9 Hall effect active boron dose measurements showing data for material beyond the process window. Some material was thermally annealed at 750 °C for 5 minutes and 2 hours. It is expectedly observed that as the melt penetrates into the depth and consumes interstitials, the active dose increases due to decreased boron-interstitial clustering. (Implant conditions: 15 keV Si⁺ 1x10¹⁵/cm², 1 keV B⁺ 1x10¹⁴/cm²)

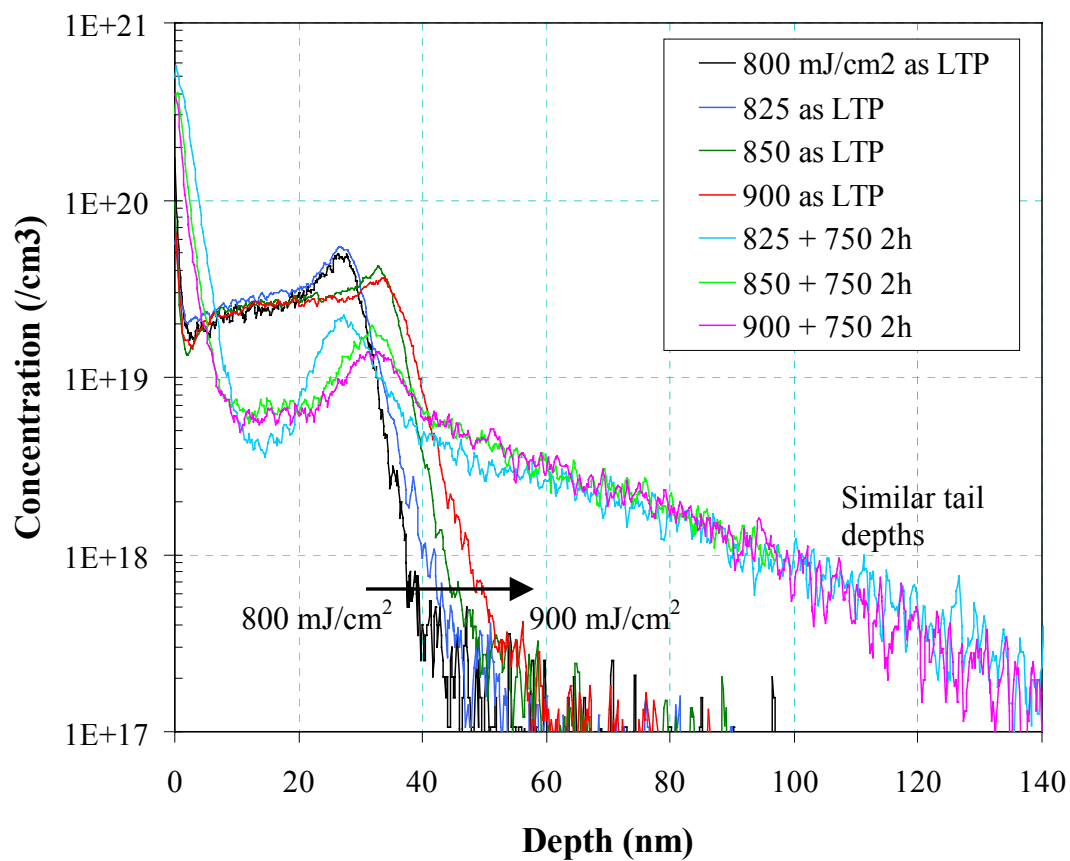


Figure 5-10 SIMS boron profiles for material laser annealed beyond the process window. While each started with a successively deeper junction depth, after a 750 °C 2 hour thermal anneal, all diffused to a junction depth of approximately 140 nm. (Implant conditions: 15 keV Si⁺ 1x10¹⁵/cm², 1 keV B⁺ 1x10¹⁴/cm²)

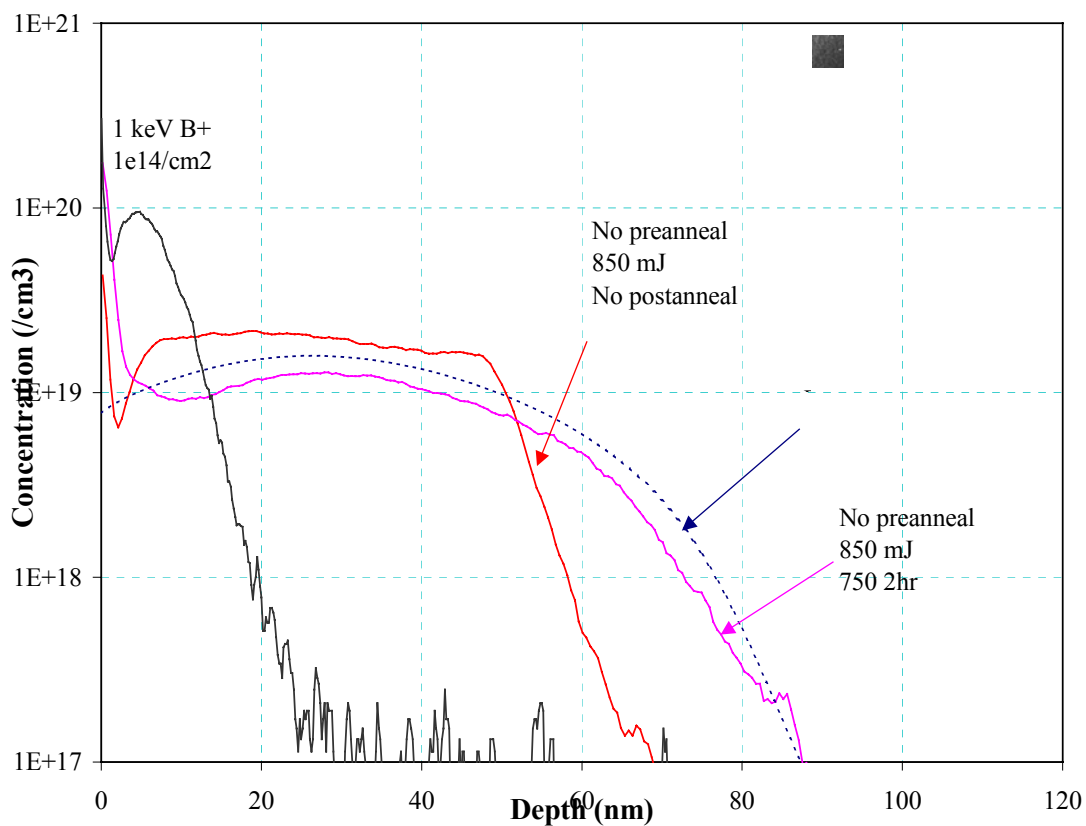


Figure 5-11 SIMS profile showing transient enhanced diffusion of boron in laser melted material following thermal annealing at 750 °C for 2 hours. Given the depth of the melt, interstitials created by the boron implant would not be expected. This suggests an interstitial population created during the rapid liquid phase epitaxy following laser melting. (Implant conditions 1 keV B⁺ 1x10¹⁴/cm²)

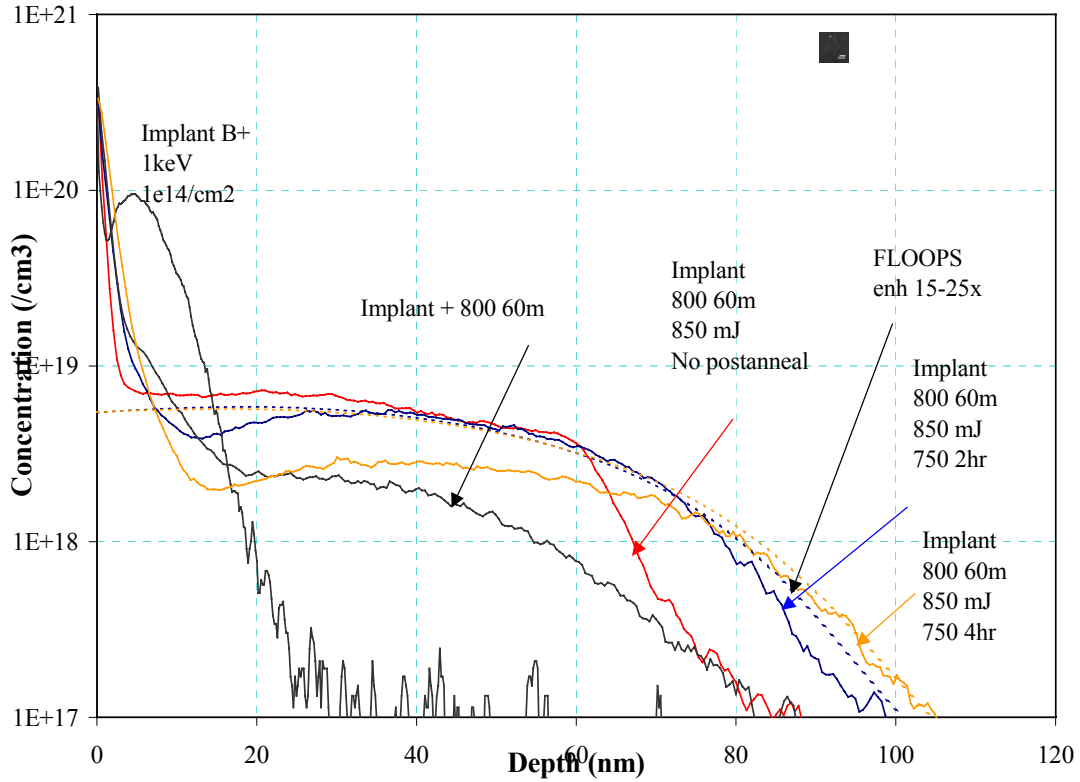


Figure 5-12 SIMS profile showing transient enhanced diffusion of boron in laser melted material following thermal annealing at 750 °C for 2 hours. Unlike in the previous figure, this material received an 800 °C anneal for 60 minutes prior to laser melting to ensure that no residual damage from the implant existed. Again, an enhanced diffusion is observed. This suggests an interstitial population created during the rapid liquid phase epitaxy following laser melting. (Implant conditions 1 keV B⁺ 1x10¹⁴/cm²)

CHAPTER 6 SUMMARY AND FUTURE RECOMMENDATIONS

Laser thermal processing is an emerging solution to conventional implant and annealing for the formation of ultra-shallow junctions in silicon IC front-end technology. Before it can be fully implemented, it is important to understand the nature of the material after laser annealing and how variations in process parameters can affect the behavior of the material during any subsequent thermal processing. This thesis has attempted to understand these variables via several characterization methods, each designed to observe a different phenomenon. With understanding of each of these events, a general theory to explain them was presented along with further experimentation to verify the theory. In this final chapter, the contributions of this thesis will be reviewed and areas for further study will be suggested.

Synopsis of Results

Due to the relatively low rate of heating and cooling provided by conventional RTA processing and the non-conservative nature of ion implantation, conventional processing suffers from interstitial based phenomena such as extended defect formation, enhanced dopant diffusion, and incomplete dopant activation due to the formation of inactive dopant-interstitial clusters. While LTP may still suffer from the deleterious effects of ion implantation, the use of lasers to anneal the material allows for little to no extended defect formation, no diffusion, and complete activation due to its rapid heating and solidification rates. However, a thorough understanding of the effects of post-LTP thermal cycling is necessary in order to allow integration of LTP into front-end silicon

processing. In addition it is critical to understand how variations in process parameters, primarily the laser energy density, can affect the material during these post-LTP thermal cycles. A number of experiments were presented; each designed to analyze the critical issues observed in conventional processing, namely extended defect formation, enhanced diffusion, and dopant clustering. The ramifications of these findings and the contributions to science are as follows:

1. Characterized the extended defect evolution in both the end of range and in the epitaxially grown silicon layer of LTP material during post-LTP thermal annealing.
2. Characterized the dopant behavior with regards to enhanced diffusion and deactivation via dopant-interstitial clustering in LTP material during post-LTP thermal annealing.
3. Correlated epitaxy induced defects and the suppression of interstitial based phenomena.
4. Demonstrated that while the metallurgical and electrical properties of LTP material laser annealed within the process window are the same, their behavior during post-LTP thermal annealing is dramatically different due to differences in the densities of epitaxial defects.
5. Suggested that by controlling the amorphous-crystalline interface prior to laser annealing, epitaxial defect densities formed throughout the process window could be made to be more uniform, thus providing for more uniform material behavior during subsequent thermal cycling.

6. Presented evidence of quenching interstitials into the epitaxially grown silicon during the laser induced melt recrystallization.

It was found that while the laser energy density itself had little to no effect on the populations of interstitials created by the amorphization process, the epitaxial defects that resulted from the rapid solidification from the laser induced melt did impact the behavior of interstitials. While these defects can be dissolved using thermal annealing, it was found that while present, these epitaxial defects captured interstitials preventing them from participating in dislocation loops evolution, enhanced diffusion of boron, and boron-interstitial clustering.

Conclusion

This thesis provides a significant scientific contribution to the understanding of the nature and behavior of crystallographic defects in laser thermal processed silicon and how they might impact the future integration of this process into current silicon front-end processing technologies.

Areas of Further Study

Future studies within this field could be extended towards the optimization of process conditions prior to laser annealing so that uniform densities of epitaxial defects could be produced. This could be combined with current studies that seek to use thermal transfer layers designed to increase the range of the laser energy density process window. Together these studies could reduce the barriers to the future implementation of LTP into silicon IC front-end processing. It is also necessary to understand how variations in processing conditions affect the leakage currents in LTP formed devices.

Further investigation into the possibility of quenched in interstitials during liquid phase epitaxy is also needed. While the findings here suggest that this phenomenon is

real, they are by no means conclusive. These investigations could also be extended toward the rapid recrystallization of amorphous layers during flash lamp annealing.

APPENDIX A EFFECT OF PARAMETER VARIATIONS

The purpose of this appendix is to analyze how unintentional variations in the laser energy affect the material. Throughout the text laser energy densities are cited by the parameter that was input into the laser control program, rather than the fluence actually measured by the photometer. The energy measured often varied by as much as ± 15 mJ/cm^2 from sample to sample. It was unknown whether this variation was actually variations in the laser power output or actually error in the recording equipment. In order to determine this, four samples were selected. Two were from the materials that were laser annealed at $770 \text{ mJ}/\text{cm}^2$ and two were annealed at $800 \text{ mJ}/\text{cm}^2$. Within the first set, the recorded energy densities were 768 and $789 \text{ mJ}/\text{cm}^2$. In the second set the recorded energy densities were 793 and $811 \text{ mJ}/\text{cm}^2$. Plan view TEM was performed on these samples and their defect structures examined in Figure A-1. It is observed that despite only a $4 \text{ mJ}/\text{cm}^2$ difference between the two extreme samples, 789 and $793 \text{ mJ}/\text{cm}^2$, these two samples appear to have defect densities more similar to the other in their respective sets. However, there was still a difference in epitaxial defect density observed between 768 and $789 \text{ mJ}/\text{cm}^2$ materials. Thus it was determined that only materials within 1 standard deviation of the mean energy density would be used. The standard deviations for the 770 and $800 \text{ mJ}/\text{cm}^2$ materials were 9 and $7 \text{ mJ}/\text{cm}^2$, respectively.

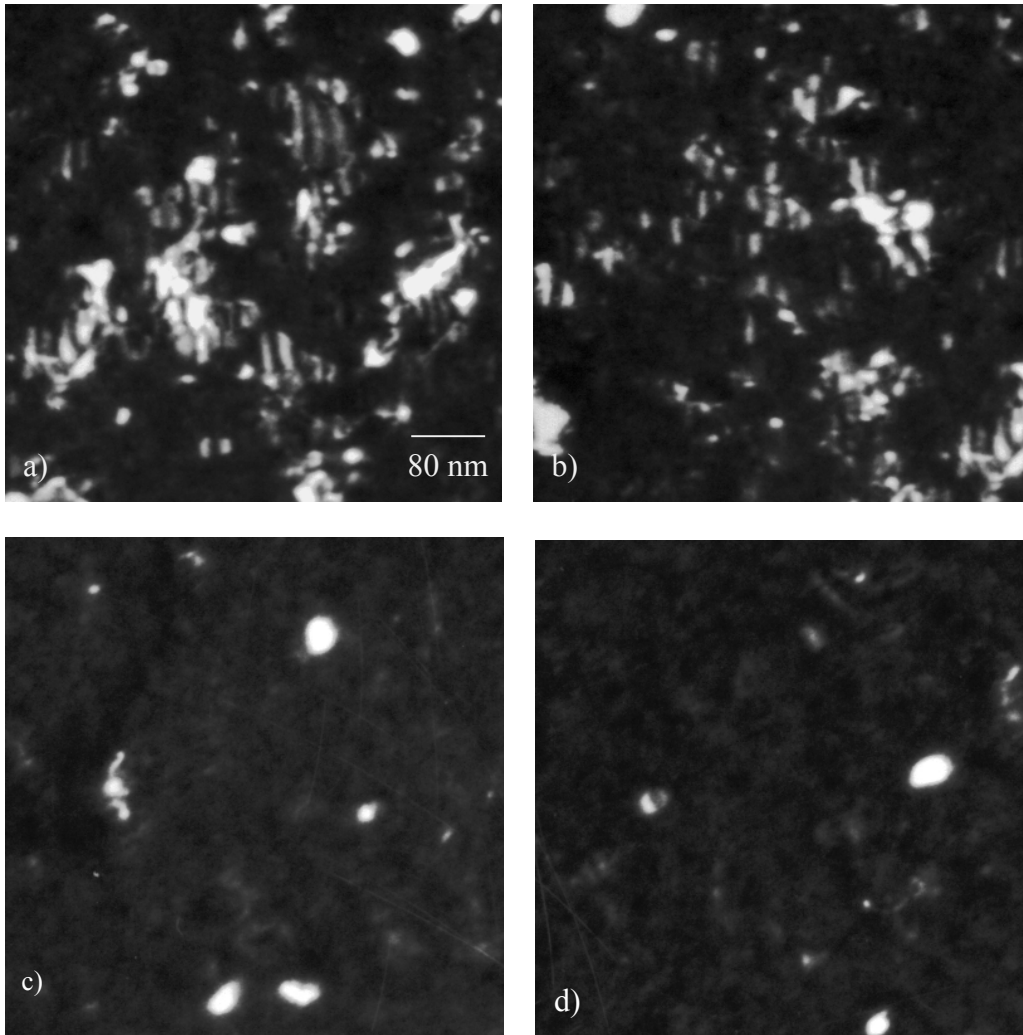


Figure A-1 PTEM images showing how variations in measured laser energy density affect the epitaxial defect density. Images are of a) 768, b) 789, c) 793, and d) 811 mJ/cm^2 .

APPENDIX B STEREOLOGY OF DEFECTS

Because of the nature in which TEM is performed and the large depth of field of the electron beam, defects located at two different z-positions can appear to occupy the same space in the final projected image. Thus it becomes necessary to develop a stereological method of defect quantification that will allow distinction between the various defect types. In the case of material that has been laser processed and subsequently thermal annealed, the defects in question are dislocation loops, which form near the original amorphous-crystalline interface, and the epitaxy induced crystal defects, which exist in recrystallized region. Under $g/3g$ 220 weak-beam darkfield conditions, dislocation loops appeared as small ellipses and circles. Under the same conditions, dislocations appear as high contrast strings that often overlapped with other dislocations. Often these defects can be very small in size and appear circular. Thus it can be difficult to distinguish dislocations that terminate within the bulk and those that do not.

To determine the epitaxial defect density and the trapped interstitial density in dislocation loops of a material, the image was first enlarged 150,000X (50kX via TEM and 3x via optical enlargement). Then five 4 cm by 4 cm boxes on a transparency were randomly placed on the image. Circular defects within the boxes that had dark interior regions were carefully circled and labeled as dislocation loops. Defects that were circular but did not contain a dark interior were circled on a separate transparency and labeled as uncertain. Finally, the number of separate epitaxial defects within each box was counted. To determine the epitaxial defect density, the number of certain epitaxial defects was

added to the number of uncertain defects, and the total was multiplied by the squared magnification (150kX) divided by the area of the region measured (16 cm²). The five results were then averaged to give an epitaxial defect density. For interstitials bound in dislocation loops, the transparency was analyzed using a freeware program called Scion Image. This program scans the transparency and calculate the total area inside the traced loops. This area is then compared to the total area of the analyzed area (16 cm²) and a fractional area bound by loops is determined. Given that these loops all reside on the {111} plane, multiplication of this fraction with the {111} atomic packing density, $7.8 \times 10^{14}/\text{cm}^2$, gives the trapped interstitial density. This process is repeated for the uncertain transparency. It was found that the uncertain defect density more closely followed the epitaxial defect density. Thus it was determined that only defects that had definite dark interior regions would be counted as loops.

LIST OF REFERENCES

- Aga99 Agarwal, A., Fiory, A.T., Gossmann, & H.-J., Semiconductor International, **22**, 71 (1999).
- Ase98 Aselage, T.L., Journal of Materials Research, **13**, 1786 (1998).
- Aus78 Auston, D.H., Surko, C.M., Venkatesan, T.N.C., Slusher, R.E., & Golovchenko, J.A., Appl. Phys. Lett., **33**, 437 (1978).
- Avc01 Avci, I., Law, M.E., Jasper, C., Rueda, H.A., & Thoma, R., Mat. Res. Soc. Symp. Proc., **669**, J441 (2001).
- Azi87 Aziz, M.J., Tsao, J.Y., Thompson, M.O., Peercy, P.S., & White, C.W., Mat. Res. Soc. Symp. Proc., **57**, 487 (1987).
- Bae80 Baeri, P., Poate, J.M., Campisano, S.U., Foti, G., Rimini, E., & Cullis, A.G., Appl. Phys. Lett., **37**, 912 (1980).
- Bae81 Baeri, P., Foti, G., J.M Poate., Campisano, S.U., & Cullis, A.G., Appl. Phys. Lett., **38**, 800 (1981).
- Bag78 Bagley, B.G., & Chen, H.S., AIP Conf. Proc., **50**, 97 (1978).
- Ban00a Banisaukas, H., Jones, K.S., Falk, S., & Downey, D.F., Mat. Res. Soc. Symp. Proc., **610**, B10.3.1 (2000).
- Ban00b Banisaukas, H., PhD Dissertation, University of Florida, 2000.
- Ban01 Banisaukas, H., Jones, K.S., Talwar, S., Downey, D.F., & Falk, S., Materials Science in Semiconductor Processing, **4**, 339 (2001).
- Bea79 Bean, J.C., Leamy, H.J., Poate, J.M., Rozgonyi, G.A, van der Ziel, J.P., & Williams, J.S., J. Appl. Phys., **50**, 881 (1979).
- Bel03 Bellis, M., Inventors, About Inc. (accessed June 2003) {<http://inventors.about.com/library/blcoindex.htm>}.
- Bor02 Borland, J.O., Mat. Res. Soc. Symp. Proc., **717**, 3 (2002).
- Bra95 Bracht, H., Stolwijk, N.A., & Mehrer, H., Phys. Rev. B, **52**, 542 (1995).

- Cal97 Callister, W.D., in Materials Science and Engineering (John Wiley & Sons, New York, 1997).
- Cam80 Campisano, S.U., Foti, G., & Servidori, M., Appl. Phys. Lett., **36**, 279 (1980).
- Cam02 Camillo-Castillo, R. A., Jones, K. S., Law, M. E., & Rubin, L. M., Mat. Res. Soc. Symp. Proc., **717**, 21 (2002).
- Col00 Collart, E.J.H., Murrell, A.J., Foad, M.A., van den Berg, J.A., Zhang, S., Armour, D., Goldberg, R.D., Wang, T.-S., Cullis, A.G., Clarysse, T., & Vandervorst, W., J. of Vac. Sci. and Tech. B, **18**, 435 (2000).
- Cow86 Cowern, N. E. B., Yallup, K. J., Godfrey, D. J., Hasko, D. G., McMahon, R. A., Ahmed, H., Stobbs, W. M., & McPhail, D. S., Mat. Res. Soc. Symp. Proc., **52**, 65 (1986).
- Cul81 Cullis, A.G., Hurle, D.T.J., Webber, H.C., Chew, N.G., Poate, J.M., Baeri, P., & Foti, G., Appl. Phys. Lett., **38**, 642 (1981).
- Cur04 Curie, M., in Radio-Active Substances (Chemical News Office, London, 1904).
- Dok96 Dokumaci, O., Law, M.E., Krishnamoorthy, V., Jones, K.S., Mat. Res. Soc. Symp. Proc., **396**, 167 (1996).
- Don85 Donovan, E.P., Spaepen, F., Turnbull, D., Poate, J.M., & Jacobson, D.C., J. Appl. Phys., **57**, 1795 (1985).
- Eag96 Eaglesham, D.J., Agarwal, A., Haynes, T.E., Gossmann, H.-J., Jacobson, D.C., & Poate, J.M., Nuclear Inst. & Methods in Phys. Res. Section B, **120**, 1 (1996).
- Fai80 Fair, R.B., J. Appl. Phys., **51**, 5828 (1980).
- Gab02 Gable, K.A., Jones, K.S., Law, M.E., Robertson, L.S., & Talwar, S., Mat. Res. Soc. Symp. Proc., **717**, C1.10 (2002).
- Gal82 Galvin, G.J., Thompson, M.O., Mayer, J.W., Hammond, R.B., Paulter, N., & Peercy, P.S., Phys. Rev. Lett., **48**, 33 (1982).
- Gös96 Gösele, U., Plössl, A., & Tan, Y.T., in Process Physics and Modeling in Semiconductor Technology (Electrochemical Society, New Jersey, 1996).
- Her97 Herner, B., Krishnamoorthy, V., Jones, K.S., Mogi, T.K., & Gossmann, H.-J., Mat. Res. Soc. Symp. Proc., **442**, 157 (1997).

- Hob00 Hobler, G., Pelaz, L., & Rafferty, C.S., J. Electrochem. Soc., **147**, 3494 (2000).
- Hu97 Hu, S.M., Mat. Sci. and Engineering, **R13**, 105 (1997).
- Jon86 Jones, K.S., & Prussin, S., Mat. Res. Soc. Symp. Proc., **71**, 173 (1986).
- Jon89 Jones, K.S., in The Encyclopedia of Advanced Materials (Pergamon, New York, 1989).
- Jon00 Jones, K.S., Kuryliw, E., Murto, R., Rendon, M., & Talwar, S., Ion Implant Tech. Conf., 111 (2000).
- Key01 Keys, P., PhD Dissertation, University of Florida, 2001.
- Kim02 Kim, S.-D., Park, C.-M., & Woo, J.C.S., IEEE Trans. Elec. Dev., **49**, 1748 (2002).
- Kur02 Kuryliw, E., Jones, K.S., Sing, D., Rendon, M.J., & Talwar, S., Mat. Res. Soc. Symp. Proc., **717**, 39 (2002).
- Lar78 Larson, B.C., White, C.W., & Appleton, B.R., Appl. Phys. Lett., **32**, 801 (1978).
- Law02 Law, M.E., FLOOPS User's Manual (University of Florida, Gainesville, 2002).
- Li98 Li, J.-H., Law, M.E., Jasper, C., & Jones, K.S., Materials Science in Semiconductor Processing, **1**, 99 (1998).
- Lil00 Lilak, A.D., Krishnamoorthy, V., Vieira, D., Law, M., & Jones, K., Mat. Res. Soc. Symp. Proc., **610**, B5.4.1 (2000).
- Lin03 Lindfors, C., PhD Dissertation, University of Florida, 2003.
- May70 Mayer, J.W., Eriksson, L., & Davies, J.A., in Ion Implantation in Semiconductors (Academic Press, New York, 1970).
- May90 Mayer, J.W., & Lau, S.S., in Electronic Materials Science: For Integrated Circuits in Si and GaAs (Macmillan, New York, 1990).
- Moo75 Moore, G.E., Tech. Dig. Int. Electron Devices Meet., **75**, 11 (1975).
- Mur00 Murto, R., Jones, K., Rendon, M., & Talwar, S., Ion Implantation Technology, 155 (2000).

- Nar81 Narayan, J., J. Appl. Phys., **52**, 1289 (1981).
- NIS03 National Institute of Standards and Technology, Nanostructures and CMOS (accessed June 2003) {<http://www.eeel.nist.gov/812/nano.html>}.
- Nob89 Nobili, D., Angelucci, R., Armigliato, A., Landi, E., & Solmi, S., J. Electrochem. Soc., **136**, 1142 (1989).
- Ole84 Olesinski, R.W., & Abbaschian, G.J., Bull. Alloy Phase Diagrams, **5**, 478 (1984).
- Ols88 Olson, G. L., & Roth, J. A., Materials Science Reports, **3**, 77 (1988).
- Pan96 Pan, S., & Mitchell, I.V., Materials Chemistry and Physics, **46**, 252 (1996).
- Par01 Park, C., Kim, S.-D., Wang, Y., Talwar, S., & Woo, J.C.S., VLSI Technology Digest of Technical Papers, 69 (2001).
- Pee85 Peercy, P.S., & Thompson, M.O., Mat. Res. Soc. Symp. Proc., **35**, 53 (1985).
- Pen84 Pennycook, S. J., Narayan, J., & Holland, O.W., Electrochem. Soc. Extended Abstracts, **84-2**, 672 (1984).
- Pen85 Pennycook, S. J., Marayan, J., & Culbertson, R. J., Mat. Res. Soc. Symp. Proc., **36**, 151 (1985).
- Pen86 Pennycook, S. J., & Culbertson, R. J., Mat. Res. Soc. Symp. Proc., **52**, 37 (1986).
- Phi72 Phillips, V.A., Acta Metallurgica, **20**, 1143 (1972).
- Poa82 Poate, J.M., & Mayer, J.W., in Laser Annealing of Semiconductors (Academic Press, New York, 1982).
- Pru74 Prussin, S., J. Appl. Phys., **45**, 1635 (1974).
- Pru86 Prussin, S., & Jones, K.S., Nuclear Inst. & Methods in Phys. Res. Section B, **B21**, 496 (1986).
- Rou94a Rousseau, P.M., Griffin, P.B., & Plummer, J.D., Appl. Phys. Lett., **65**, 578 (1994).
- Rou94b Rousseau, P.M., Griffin, P.B., Kuehne, S.C., & Plummer, J.D., IEEE International Electron Devices Meeting, 35.1.1 (1994).

- Rou96 Rousseau, P.M., Griffin, P.B., Kuehne, S.C., & Plummer, J.D., IEEE Trans. Elec. Devices, **43**, 547 (1996).
- Rou97 Rousseau, P.M, Crowder, S.W., Griffin, P.B., & Plummer, J.D., IEEE Electron Device Lett., **18**, 42 (1997).
- Rut06 Rutherford, E., in Radioactive Transformations (C. Scribner's Sons, New York, 1906).
- Sei97 Seibt, M., Huang, Y.-L., & Plikat, B., Diffusion and Defect Data Pt.B: Solid State Phenomena, **57-58**, 377 (1997).
- Ser89 Servidori, M., Cembali, F., Fabbri, R., Gabilli, E., Negrini, P., Solmi, S., Zaumseil, P., Winter, U., Anderle, M., & Canteri, R., Nuclear Inst. & Methods in Phys. Res. Section B, **B39**, 347 (1989).
- Sho54 Shockley, W., Forming Semiconductor Devices by Ionic Bombardment, US Patent 2787564, Bell Laboratories, 1954.
- SIA00 Silicon Industry Association, International Technology Roadmap for Semiconductors 2000 Update, Semiconductor Industry Association, San Jose, California (accessed October 2000) {<http://www.public.itrs.net/>}.
- SIA02 Silicon Industry Association, International Technology Roadmap for Semiconductors 2002 Update, Semiconductor Industry Association, San Jose, California (accessed November 2002) {<http://www.public.itrs.net/>}.
- Sol89 Solmi, S., Cembali, F., Fabbri, R., Lotti, R., Servidori, M., Anderle, M., & Canteri, R., Nuclear Inst. & Methods in Phys. Res. Section B, **B37- 38**, 394 (1989).
- Sol96 Solmi, S., & Valmorri, S., Mat. Res. Soc. Symp. Proc., **438**, 95 (1996).
- Spa79 Spaepen, F., & Turnbull, D., AIP Conf. Proc., **50**, 73 (1979).
- Spe94 Specht, E.D., Walko, D.A., & Zinkle, S.J., Mat. Res. Soc. Symp. Proc., **316**, 241 (1994).
- Sto86 Stolwijk, N.A., Holzl, J., Frank, W., Weber, E.R., & Mehrer, H., Appl. Phys. A, **39**, 37 (1986).
- Sto95 Stolk, P.A., Gossmann, H.-J., Eaglesham, D.J., Jacobson, D.C., & Luftman, H.S., Mat. Res. Soc. Symp. Proc., **354**, 307 (1995).

- Sto97 Stolk, P.A., Gossmann, H.-J., Eaglesham, D.J., Jacobson, D.C., Rafferty, C.S., Gilmer, G.H., Jaraiz, M., Poate, J.M., Luftman, H.S., & Haynes, T.E., J. Appl. Phys., **81**, 6031 (1997).
- Tak01 Takamura, Y., Jain, S., Griffin, P.B., & Plummer, J., Mat. Res. Soc. Symp. Proc., **669**, J731 (2001).
- Tal98 Talwar, S, Verma, G., & Weiner, K.H.; Ion Implantation Technology Proc., **2**, 1171 (1998).
- Tal00 Talwar, S., Felch, S., Downey, D., & Wang, Y., Ion Implantation Technology, 175 (2000).
- Tan85 Tan, T.Y., & Gösele, U., Appl. Phys., **A37**, 1 (1985).
- Tas89 Tasch, A.F., Park, C., Alvis, J., & Novak, S., J. Electrochem. Soc., **136**, 810 (1989).
- Til53 Tiller, W.A., Jackson, K.A., Rutter, J.W., & Chalmers, B., Acta Metallurgica, **1**, 428 (1953).
- Van58 L. J. van der Pauw, "A Method of Measuring Specific Resistivity and Hall Effect of Discs of Arbitrary Shapes," Philips Res. Repts. 13, 1 (1958).
- Ver95 Verma, G., Slaoui, A., Talwar, S., & Sigmon, T.W., IEEE Elec. Device Lett., **16**, 14 (1995).
- Ver96 Verma, G., Talwar, S., & Sigmon, T.W., Appl. Phys. Lett., **69**, 319 (1996).
- Whi80 White, C.W., Wilson, S.R., Appleton, B.R., & Young, F.W., J. Appl. Phys., **51**, 738 (1980).
- Yam02 Yamamoto, T., Goto, K., Tada, Y., Kikuchi, Y., Kubo, T., Wang, Y., Talwar, S., Kase, M., & Sugii, T., VLSI Technology Digest of Technical Papers, 138 (2002).
- Yu99 Yu, B., Wang, Y., Wang, H., Xiang, Q., Riccobene, C., Talwar, S., & Lin, M.-R., Electron Devices Meeting, 509 (1999).
- Zai01 Zaitsev, A.I., & Kodentsov, A.A., Journal of Phase Equilibria, **22**, 126 (2001).
- Zie02 Ziegler, J.F., The Stopping and Range of Ions in Solids (IIT Press, New York, 2002).

BIOGRAPHICAL SKETCH

Erik Kuryliw was born in Dearborn, Michigan on May 23, 1974. He received his B.S. and M.S. degrees in materials science and engineering from University of Florida in 1996 and 2000, respectively. He began his work towards his Ph.D. at the University of Florida in 2000. During his time in graduate school he interned at Eaton Corporation's Semiconductor Equipment Operations division, now Axcelis, where he worked on phase transformation of titanium silicides. He has also twice interned at Intel Corporation, once in the TCAD department and once in the Quality and Reliability department. His primary research interests are in materials characterization.